2013-07-10

Thermodynamic, Kinetic and Mechanistic Investigations of Binding and Activation of Molecular Oxygen and Mesityl Nitrile Oxide

Xiaochen Cai
aspirincai@gmail.com

UNIVERSITY OF MIAMI

THERMODYNAMIC, KINETIC AND MECHANISTIC INVESTIGATIONS IN
BINDING AND ACTIVATION OF MOLECULAR OXYGEN AND MESITYL
NITRILE OXIDE

By

Xiaochen Cai

A DISSERTATION

Submitted to the Faculty
of the University of Miami
in partial fulfillment of the requirements for
the degree of Doctor of Philosophy

Coral Gables, Florida

August 2013

UNIVERSITY OF MIAMI

A dissertation submitted in partial fulfillment of
the requirements for the degree of
Doctor of Philosophy

THERMODYNAMIC, KINETIC AND MECHANISTIC INVESTIGATIONS IN
BINDING AND ACTIVATION OF MOLECULAR OXYGEN AND MESITYL
NITRILE OXIDE

Xiaochen Cai

Approved:

_____   _____
Carl D. Hoff, Ph.D.   M. Brian Blake, Ph.D.
Professor of Chemistry   Dean of the Graduate School

_____   _____
Angel Kaifer, Ph.D.   Burjor Captain, Ph.D.
Professor of Chemistry   Professor of Chemistry

_____
Manuel Temprado Morena, Ph.D.
Professor of Chemistry
Universidad de Alcalá

CAI, XIAOCHEN   (Ph.D., Chemistry)

Thermodynamic, Kinetic and Mechanistic Investigations   (August 2013)
in Binding and Activation of Molecular Oxygen and
Mesityl Nitrile Oxide

Abstract of a dissertation at the University of Miami.

Dissertation supervised by Professor Carl D. Hoff.
No. of pages in text. (158)

Oxygen activation and binding to two transition-metal systems: late transition-metal system $Pd(L_1)(L_2)$ (L_1 = NHC, L_2 = NHC or PR_3, NHC = N-heterocyclic Carbene) and early transition-metal system $V(N(^tBu)Ar)_3$ (Ar = $3,5-Me_2C_6H_3$) was explored in order to gain information about the thermodynamics, kinetics and mechanism of O_2 binding to metal complexes. In this work, a novel oxygen binding mode was discovered and the resulting complex $Pd(IPr)_2(\eta^1-O_2)_2$ was reported as the first η^1 oxygenation palladium complex. This reaction was further studied and a plausible mechanism of O_2 binding to $Pd(L_1)(L_2)$ system was proposed, in which the effect of ligands bulkiness and an equilibrium between η^1-O_2Pd and η^2-O_2Pd were highlighted. In addition, an early transition-metal peroxo complex $V(N(^tBu)Ar)_3(\eta^2-O_2)$ has been prepared directly by reaction with O_2. Its equilibrium with $V(N(^tBu)Ar)_3(\eta^1-O_2)$ and its reactivity were investigated. In the end the binding and activation of a potent oxygen atom transfer reagent MesCNO were studied.

TABLE OF CONTENTS

vi

LIST OF FIGURES

CHAPTER 5

APPENDIX

LIST OF SCHEMES

CHAPTER 5

LIST OF TABLES

"It was the best of times, it was the worst of times, it was the age of wisdom, it was the age of foolishness, it was the epoch of belief, it was the epoch of incredulity, it was the season of Light, it was the season of Darkness, it was the spring of hope, it was the winter of despair."

Charles Dickens, A Tale of Two Cities

Chapter 1: Introduction

1.1   Overview

The quotation above from Dickens seems characteristic of scientific research in general, and particularly true for those working in catalytic chemistry—research is made of ups and downs and that pattern was followed in development of this thesis.

An alternative title for this dissertation might be "A Tale of Two Complexes"—both of which bind O_2 but in ways that are both different and the same. The two "cities" in this work are: the late transition-metal complex $Pd(IPr)_2$ (IPr = 1,3-bis(diisopropyl)phenylimidazol-2-ylidene) and the early transition-metal complex $V(N(^tBu)(Ar))_3$ (Ar = 3,5-Me$_2$C$_6$H$_3$). The study of these two complexes and how they bind O_2 evolved out of solution calorimetric studies of which led beyond the initial research goal. Dickens' motif of doubles is also reflected in the two different ways (end-on and side-on) in O_2 binding to $Pd(IPr)_2$ and $V(N(^tBu)(Ar))_3$, two intermediates involved in reaction of O_2 with $Pd(IPr)_2$, and the distinctive reactivities the two demonstrate. All of these studies will be discussed in the following chapters.

The first project the author worked on was binding of a series of nitriles to the Kubas complex $Mo(CO)_3(P^iPr_3)_2$ to form a series of brightly colored adducts shown in Figure 1.1. This work was extended to a collaborative project with Professor Kit Cummins (MIT) and Elena Rybak Akimova (Tufts) on binding of the same set of nitriles to the paramagnetic complex $V(N(^tBu)Ar)_3$ in work that remains in progress.

Figure 1.1 Colors of the $Mo(P^iPr_3)_2(CO)_3(RCN)$ complexes studied. From left to right: R = Ad; $4\text{-}NMe_2C_6H_4$; $2,4,6\text{-}Me_3C_6H_2$; C_6H_5; $2,6\text{-}F_2C_6H_3$; $4\text{-}CF_3C_6H_4$; F_5C_6.

Calorimetric measurements in the $V(N(^tBu)Ar)_3$ system were difficult since the paramagnetic compound was found to bind most ligands weakly. This leads to the question of what would be the strongest possible ligand binder to $V(N(^tBu)Ar)_3$ which has two unpaired electrons. It was decided that O_2 (which also has two unpaired electrons) should be the ideal partner. At first this idea was dismissed due to the steric crowding present in the V(III) system. In spite of that dismissal, the reaction was attempted and a green diamagnetic product was formed. The investigation of the structure and mechanism of formation of that complex is presented in chapter 4 of this thesis.

The other major "city" in this work is quite different. Although it has a different beginning and in many cases differing results, it shares some surprising features in common with its "sister city". This project began as a simple study of the enthalpy of binding of O_2 to a series of $Pd(L_1)(L_2)$ complexes in which L_1 and L_2 can be a phosphine ligand (PR_3) or an *N*-heterocyclic carbene (NHC) ligand. A range of steric and electronic factors can be varied in these ligand systems and the goal was to see how that has influenced the energetics of binding of O_2 to form *cis*- $Pd(L_1)(L_2)(\eta^2\text{-}O_2)$. As described in chapter 2, ligand variation was proven to affect not just the energetics of binding, but the outcome as well. In contrast to all other systems of this type studied to date, a new type of

binding was observed for very bulky NHC ligands and the paramagnetic complexes *trans*-Pd(L)$_2$(η^1-O$_2$)$_2$ were formed instead (L = IPr, SIPr, IPr = 1,3-bis(diisopropyl)phenylimidazol-2-ylidene, SIPr = 1,3-bis(diisopropyl)phenylimidazolin-2-ylidene).

These discoveries—the unexpected formation of a stable V(V) peroxo complex and a Pd(II) bis-superoxo complex led to more detailed investigations of the nature of binding of O$_2$ in these systems. These studies led to questions outside the expertise of the Hoff group, and collaborative work was initiated--structural studies with Professor Captain (Miami), computational studies with Professor Prabhakar (Miami) and Temprado (Spain), stopped flow kinetic studies with Professor Rybak-Akimova (Tufts), magnetic studies with Professor Wieghardt (Mülheim), and ^{51}V NMR and other studies with Professor Cummins (MIT) and Professor Nolan (St. Andrews). The author wishes now to acknowledge the many contributions of these groups. Learning to collaborate and "multitask" has been an added benefit to this work and is the way of modern science. Unless stated otherwise, all synthetic, crystal growth, solution calorimetric, FTIR kinetic, NMR kinetic, and other studies have been performed by the author. The collaborative work has enhanced the quality of this project, and the fact that these investigators from other laboratories were interested to work on this project attests to the significance of the questions being addressed in this thesis.

The first chapter of this thesis provides an introduction to the vast literature of catalyzed oxidations. Of necessity, this is selected to highlight principles and applications of direct relevance to our research. Since work with O$_2$ is new to the Hoff group, the background literature can only be summarized briefly. The second chapter describes our

initial research efforts in O_2 binding. Due to a basic interest in oxygen activation at metal centers and organometallic thermochemistry, kinetic and thermodynamic studies of O_2 binding to $Pd(L_1)(L_2)$ (L_1,L_2 = NHC and/or PR_3 ligands) systems were probed. This led ultimately to discovery of a novel end-on O_2 binding mode to the palladium center forming $Pd(IPr)_2(\eta^1\text{-}O_2)_2$. Characterization of this complex, its reactions, and properties occupy the majority of Chapter 2. While the room temperature product of oxygenation is $Pd(IPr)_2(\eta^1\text{-}O_2)_2$, at low temperatures we obtained evidence that a more conventional, but less stable and more reactive adduct was formed, namely $Pd(IPr)_2(\eta^2\text{-}O_2)$. Characterization and reactivity of this complex are described in Chapter 3 where it is compared to the related complex $Pd(IMes)_2(\eta^2\text{-}O_2)$ (IMes = N,N'-bis(2,4,6-trimethyl)phenylimidazol-2-ylidene) discovered by Stahl and coworkers. The majority of oxidation catalysts fall into two categories—low valent late transition metal complexes and high valent early transition metal complexes. In Chapter 4 investigation of binding of O_2 to a high valent Vanadium complex is reported--here as well a two-step binding of O_2 was discovered, and the nature of this addition is compared to that of the Pd complexes discussed in the earlier chapters. While O_2 has a desirable use as an oxidant in "green" catalytic chemistry it has the disadvantage of delivering two oxygen atoms at once. A number of additional oxidants, most notably pyridine oxide have been used in catalytic studies to deliver a single oxygen atom. Chapter 5 reports studies of a more reactive OAT (oxygen atom transfer) reagent, mesityl nitrile oxide (MesCNO) to a series of phosphines and a terminal metal phosphido complex as well as to selected metal complexes. A summary of what has been learned and a prognosis for future studies in this area is included in the end of Chapter 5.

1.2   Selective Oxidation

The oxidation of organic compounds by molecular oxygen has a long history. As early as in the 18th century, French chemist Lavoisier explored the secret of combustion, which is generally viewed as the start of the modern chemistry. Nowadays chemists are more interested in selective oxidation of organic chemicals instead of the total destruction that occurs in uncontrolled oxidation. This is especially vital today since petroleum hydrocarbon feedstocks are the primary source (>90%) of the world's industrial organic chemicals.[1]

Selective oxidation can be either the preferred attack on one of the components by oxidants or abscission of specific hydrogen atoms in a material. Many traditional selective oxidants, such as chlorine and metal oxides, have serious problems of dumping waste, polluting the environment. In addition, they also function at an economic loss compared to molecular oxygen, which constitutes 20.8% of the volume of air and has the advantages of being cheap, readily available and environmentally benign. Whereas molecular oxygen is viewed as the ideal oxidant it is generally highly exothermic and non-selective in its reactivity. As a result uncontrolled aerobic oxidation reactions usually lead to unselected products or even complete combustion of the starting materials instead of producing useful and expected products. A relevant recent discovery is "direct" production of H_2O_2 from a H_2 and O_2. Once started, explosive production of H_2O rather than controlled production of H_2O_2 is the ever present hazard in this chemistry. Recently Meier and Braun[2] have reported selective production of H_2O_2 at a Rh(I) catalyst utilizing formate as the ultimate source of H_2.

The challenges remained in the research of selective oxidation are, as described in a paper of Oyama,[3] "*1) Substitution of raw materials. 2) Formulation of alternative catalysts. 3) Reduction in the number of process steps. 4) Elimination of waste by-products. 5) Development of new processes.*"
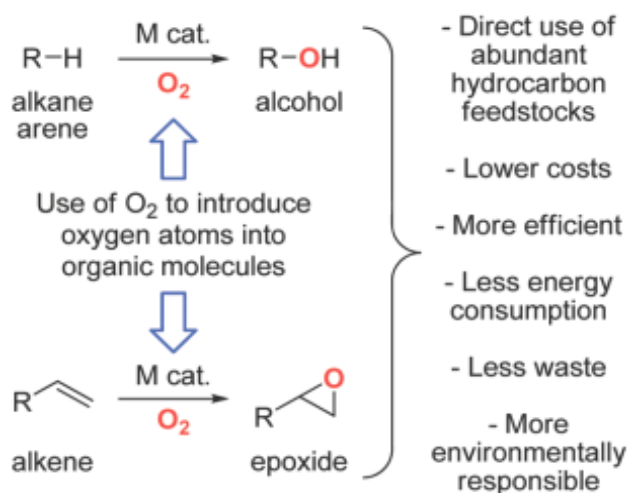
Scheme 1.1 Desired catalytic transformations and their advantages over traditional routes.[4] (Drawing taken from reference 4)

A number of catalytic systems employed in aerobic oxidation reactions have been reported up to date.[5,6] Industrial applications generally prefer use of heterogeneous catalysts such as nanoparticles, metallic carbon nanotubes, SiO_2 supported metallic complexes and metal clusters. Mechanistic information of use in catalyst design is generally easier to obtain for their soluble homogeneous counterparts.

One of the most successful oxidation catalysts to date is the Wacker process for production of acetaldehyde as shown in Eqn. (1.1). The basic individual steps for this process were actually known in the literature but were only put into practice in 1959 by a group of German scientists.[6a]

$$CH_2=CH_2 \;+\; 1/2\; O_2 \;\xrightarrow{\text{Pd/Cu Cat.}}\; CH_3CHO$$

(1.1)
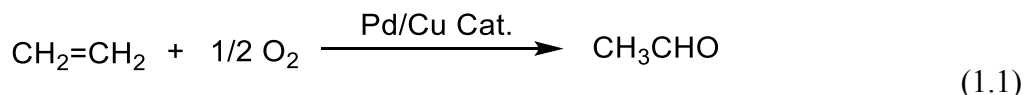
Eqn. (1.2) is the primary alcohol oxidation catalyzed by $Pd(OAc)_2/O_2/DMSO$ system reported by Peterson and Larock in 1997.[6c] Eqn. (1.3) describes the osmium(VI) oxide catalyzed dihydroxylation of olefins by using O_2 or air as the terminal oxidant.[7]

$$(1.2)$$

$$(1.3)$$
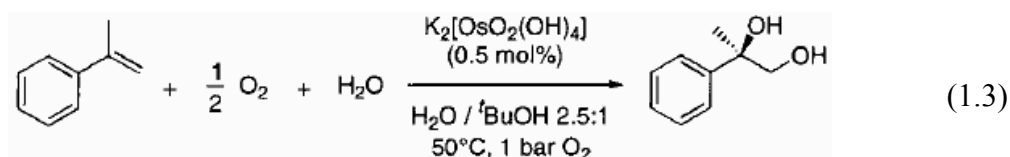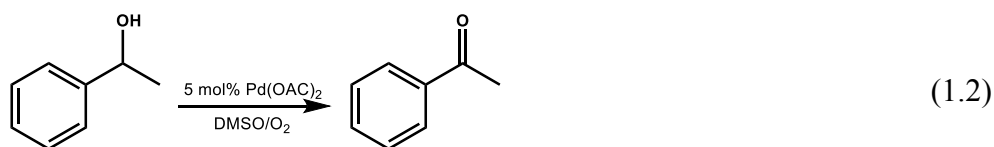
1.3 Oxidase and Oxygenase

In nature there are many metalloenzymes that catalyze selective aerobic oxidation reactions, serving as the framework and blueprint for chemists to design, modify and optimize new catalysts. These enzymes can be categorized into two classes: oxygenases and oxidases.
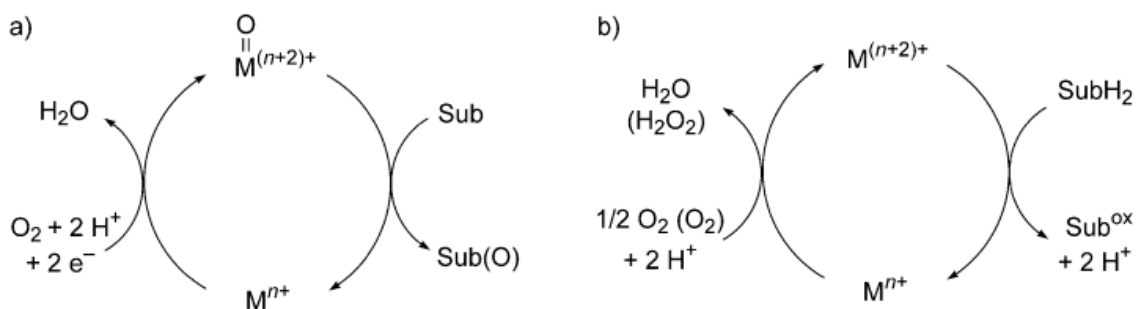
Scheme 1.2 In a selective aerobic oxidation reaction, a) The oxygenase pathway. b) The oxidase pathway.[8] (Drawing taken from reference 8)

The catalytic cycle for oxygenase and oxidase pathways in selective aerobic oxidation reactions is illustrated in Scheme 1.2 respectively. They differ with the respect to whether oxygen atoms of molecular oxygen are incorporated into the final product. In

oxygenase catalysis (Scheme 1.2a) molecular oxygen is first bound and activated by catalysts forming highly reactive metal oxides which then transfer oxygen atom to substrates. In oxidase catalysis (Scheme 1.2b) molecular oxygen only serves as an electron/proton acceptor. The hydrogen atoms extracted from substrates end up combining with oxygen forming water or hydrogen peroxide. Binding and activation of O_2 is a fundamental step in both oxygenase and oxidase catalysis.

$$C_2H_4 + Pd(II)Cl_2 + H_2O \rightarrow CH_3CHO + Pd(0) + 2\ HCl$$

$$Pd(0) + 2\ Cu(II)Cl_2 \rightarrow Pd(II)Cl_2 + 2\ Cu(I)Cl$$

$$2\ Cu(I)Cl + 2\ HCl + 1/2\ O_2 \rightarrow 2\ Cu(II)Cl_2 + H_2O$$

$$\text{Net: } C_2H_4 + 1/2\ O_2 \rightarrow CH_3CHO$$
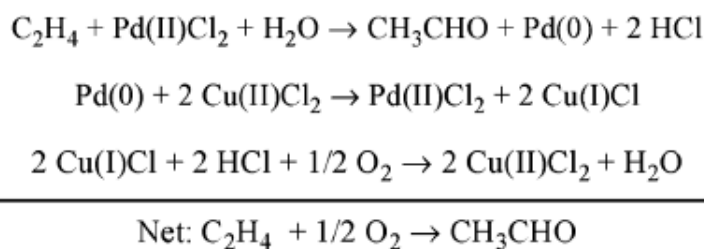
Scheme 1.3 The Wacker process reaction equations.[9]
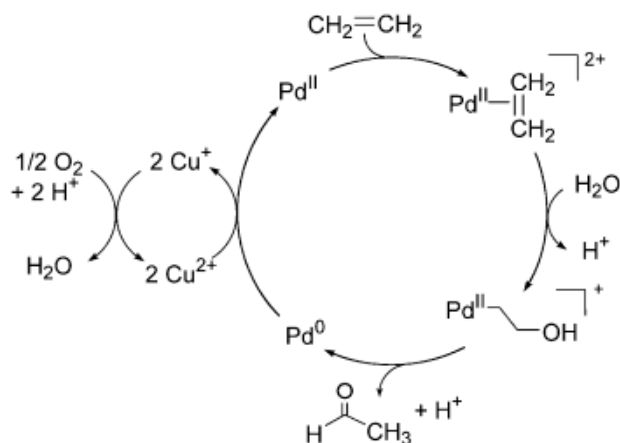
Scheme 1.4 The simplified catalytic cycle of Wacker process. (Drawing taken from reference 8)

The catalytic cycle of Wacker Process is a best example of illustrating the oxidase pathway in aerobic selective oxidation reactions. Simply judging from the net reaction equation (Eqn. (1.1)) may lead to a false conclusion that the oxygen in product is from O_2 and this reaction follows the oxygenase pathway. However, a closer investigation to the

mechanism of this process (Scheme 1.3, 1.4) shows that O_2 actually only serves as proton acceptor and oxidant of regenerating catalysts Pd^{2+} and Cu^{2+}.

Compared to catalysis by the oxidase there are far fewer reported studies in catalysis of the oxygenase pathway.[7,10,11] In the oxygenase pathway molecular oxygen first binds to metallic catalysts and becomes activated by forming metal oxides, such as ruthenium porphyrin oxide, osmium(VI) oxide and ruthenium substituted polyoxometalate, which then transfer oxygen atom to substrates. An example illustrating this oxygenase pathway is shown in Scheme 1.5.
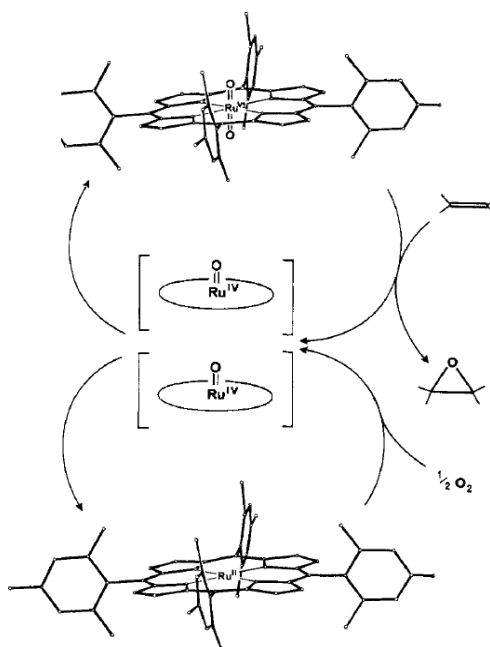
Scheme 1.5 Catalytic cycle of ruthenium porphyrin catalyst catalyzed aerobic epoxidation of olefins.[10] (Drawing taken from reference 10)

The design of an effective oxidase or oxygenase catalyst system is clearly a complex procedure. It provides motivation for the work described here but detailed investigation of a full catalytic cycle is beyond the scope of the current work which focuses on the first step in oxidation—simply binding and activation of O_2 itself. The next section describes some of the complexities involved in this first step.

1.4   Binding Modes of Molecular Oxygen to Transition-metals

The fundamental step in both oxygenase and oxidase pathways is: the binding and activation of molecular oxygen. Understanding of the mechanism of this crucial step enables chemists to design, modify and optimize the properties of transition-metal catalysts in aerobic selective oxidation reactions. Any discussion of ligand binding starts with description of the ligand itself. Coordination chemists typically view binding of a ligand to a metal as donation of a pair of electrons on the ligand to a vacant orbital on the metal.

The process of O_2 binding is more complex since O_2 is a rather unique ligand. First of all it is a diradical with two unpaired electrons in the $2p\pi^*_x$ and $2p\pi^*_y$ orbitals. In bonding, the net effect is often reduction of O_2 to O_2^{-2} in which two electrons from the metal are donated to the $2p\pi^*$ orbitals of O_2. Inorganic chemists often think of ligand binding in terms of an initial donation of a lone pair of electrons on the Lewis base ligand to a vacant orbital on the Lewis acid metal complex. However, the situation is more complex regarding binding of O_2 since the net transfer of electrons is not from the ligand to the metal, but from the metal to the ligand. The first step may involve donation of a lone pair of electrons on O_2 to the metal, as in conventional ligand binding, but the net process involves subsequent transfer of electron density from the metal to O_2. Along the way, in many cases a change in spin state occurs--as shown for binding to Vaska's[12] complex in eqn. (1.4)

$$Ir(CO(Cl)(PPh_3)_2 + O_2 \rightarrow Ir(CO(Cl)(PPh_3)_2(\eta^2\text{-}O_2) \qquad (1.4)$$
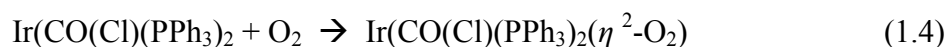
$S =$ **0**   **1**   **0**

The reactants of reaction (1.4) have $\Sigma S = 1$, whereas the products have $\Sigma S = 0$. In principle this reaction is spin forbidden and should not occur. In many organic reactions, such reactions in fact do not occur and this is why, in spite of its great thermodynamic reactivity that $^3O_2$ is inert and present in the atmosphere. While the reaction between triplet oxygen and singlet organic substrates is spin-forbidden, "*the limitation is lifted in reaction between triplet oxygen and paramagnetic species such as organic radicals or transition metal ions or complexes.*"[13] The spin paired form of oxygen $^1O_2$ is much more reactive since it does not violate the conservation of angular momentum which is the basis of the spin conservation rules. For transition metals, however, spin-orbit coupling often allows such formally spin forbidden reactions to take place.

In analysis of these reactions, the potential energy surface is often drawn for reaction of both higher energy $^1O_2$ and lower energy $^3O_2$ with the metal complex. The reaction of $^1O_2$ is not spin forbidden. The minimum energy point of the crossing curve where the two potential energy surfaces cross (reaction of the metal with both spins states of O_2) is called the MECP (Minimum Energy Crossing Point). Exactly where this happens as a function of the metal, its oxidation state, and ligand set is a topic of current interest in inorganic chemistry, and the full details of what controls this spin crossover are still in the process of being worked out. A leader in this field has been Harvey[14] and it can be expected that future work will allow better understanding of the entire process.

The important conclusion at this point, to the author, is that metal complexes often eliminate the spin forbidden nature of O_2 reactivity. A way to test whether the spin crossover retards the reaction rate is to compare rates of ligand binding which do not involve spin crossover to rates that do for the same complex. It will be discussed later for

the systems we have studied but no general conclusions can be reached at this time and each complex must be studied on a case by case basis.

The oxygen coordination modes in metal-oxygen complexes are various and can be categorized into: one-electron reduction superoxides, two-electron reduction peroxides (η^2) and high-valent metal-oxo complexes. For dioxygen it can coordinate end-on (η^1) or side-on (η^2) to one metal center; if there are more than one metal centers present, it may form bridging coordination geometries (μ-). Typical oxygen binding modes to one or more metal centers are shown in Figure 1.2.

Superoxo complexes

η^1 η^2 μ-(O^{2-}), $\eta^1(O_2^-)$ μ-η^1:$\eta^1(O_2^-)$

Peroxo and hydroperoxo complexes

$\eta^2(O_2^{2-})$ $\eta^1(OOH^-)$ cis-μ-η^1:$\eta^1(O^{2-})$ trans-μ-η^1:$\eta^1(O^{2-})$

μ-η^2:$\eta^2(O^{2-})$ μ-η^1:$\eta^2(O^{2-})$ μ$_4(O^{2-})$ μ-(O^{2-})-$\eta^1(OOH^-)$

High-valent metal-oxo Intermediates

bis-μ-oxo;
diamond core
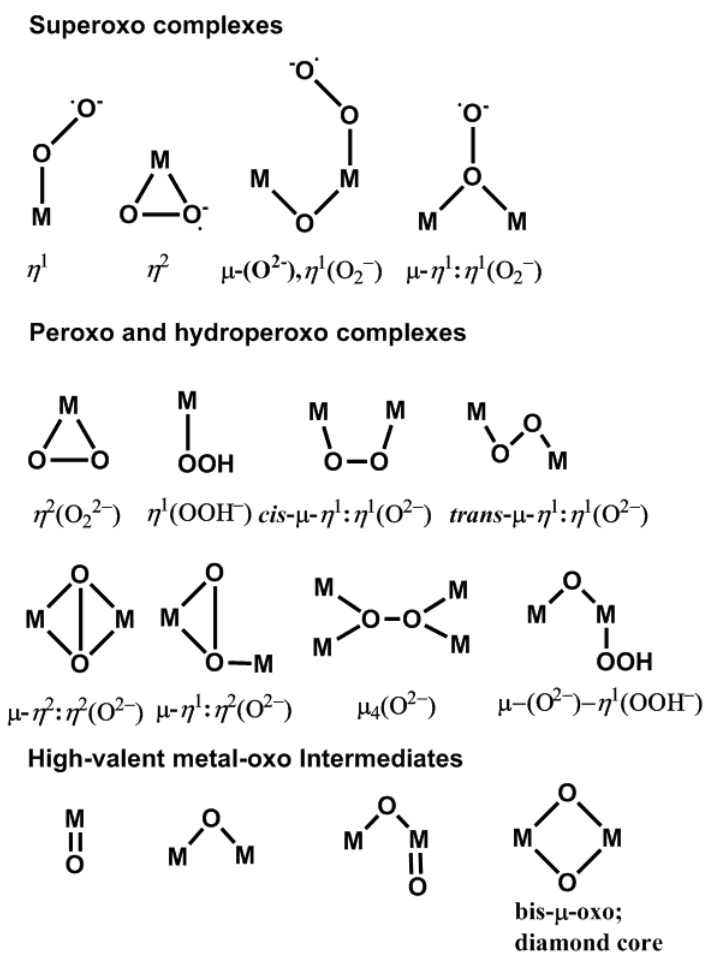
Figure 1.2 Typical oxygen coordination modes in metal-oxygen complexes.[13] (Drawing taken from reference 13)

It is generally held that the η^1 binding motif is more reactive than the η^2 motif.[15] The formation of side-bound O_2 complexes can proceed by initial end-on binding followed by isomerization or possibly by concerted binding of O_2 to form the side-bound product.[16]
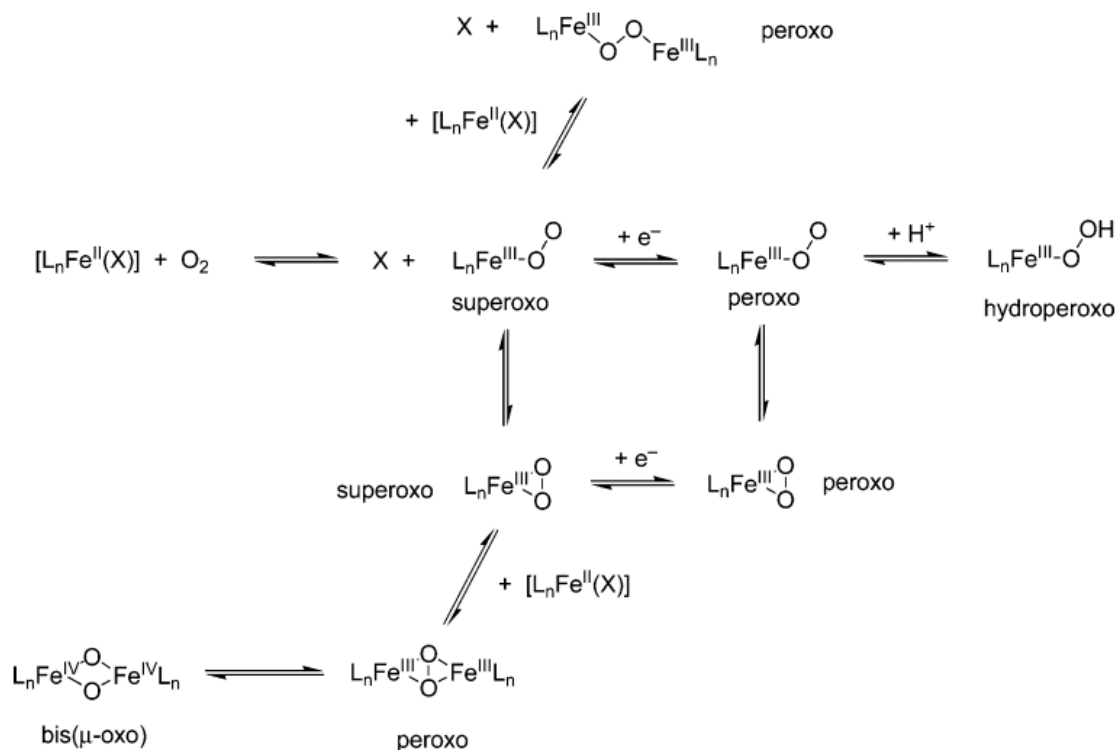
Scheme 1.6 Possible reaction pathways in oxygenation of mononuclear non-heme iron (II) complexes.[17] (Drawing taken from reference 17)

In the cases of biological systems and biological mimics, oxygenation of active metal complexes yields various products and the mechanism is complex, which normally involves several binding modes of oxygen to one or more metal centers. Scheme 1.6 illustrates the possible reaction pathways in oxygenation of mononuclear non-heme iron (II) complexes.[17] The initial product is an end-on iron (III) superoxide, which then 1) oxidizes another iron (II) forming a dinuclear iron (III) peroxo complex; or 2) gains an electron forming an end-on iron peroxo complex; or 3) does a ring-closure step and

converts to a side-on superoxo species. There is not always crystallographic or structural evidence for the presumed intermediate binding forms, often only the end product can be fully characterized and the intermediate binding stages are subject to calculations.

Numerous structures have been reported for O_2 binding. One of the first is that of the Vaska's[12] complex (see Eqn. (1.4) above). While the Vaska's complex may be most famous for its reversible binding of H_2 it also reversibly binds O_2 and the structure of the octahedreal Ir(III) (18 electron complex) is shown in Figure 1.3 a).[13] Though discovered nearly 45 years ago complexes of this type continue to be or interest and the more recent structure of Pr(IMes)$_2$(O$_2$) reported by Stahl[18] is also shown in Figure 1.3 b) for comparison.

a)   b)
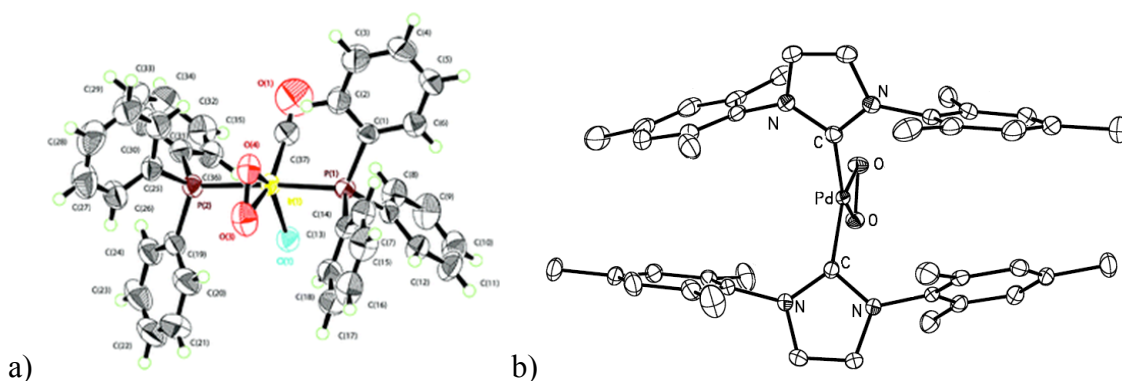
Figure 1.3 a). ORTEP diagram of Ir(CO(Cl)(PPh$_3$)$_2$(O$_2$) —a coordinatively saturated 18 electron complex of Ir(III) discovered by Vaska.[12] b). ORTEP diagram of Pd(IMes)$_2$(O$_2$) reported by Stahl.[18]

The O-O distances for the two complexes are 1.475 and 1.443 Å for the Ir and Pd complexes respectively and are in keeping with a peroxo formulation. The Vaska's complex can be viewed as a distorted octahedral, and the Stahl complex as a distorted square planer. The bidentate O_2^{-2} ligand must occupy *cis* position, but leaves a relatively large unoccupied area for the remaining ligand set as can be seen looking at the planer arrangement in the Vaska's complex of the O_2^{-2}, Cl, and CO ligands, or in the Stahl

complex the relatively large area occupied by the two IMes ligands. Following

publication of the Vaska's structure, a large amount of side-on (η^2) dioxygen complexes

have been discovered with O_2 coordinated to various transition-metal centers, particularly

for late transition metal complexes of Ir, Pt, Pd, Co.[19] There are relatively fewer

structures of end-on (η^1) dioxygen complexes, a recent Cu(I) structure[20] is shown in

Figure 1.4 below. Of particular note is the O-O bond length in the end-on binding form

which is 1.280 Å is much shorter, indicating less reduction in the O=O bonding and

formulation as an O_2^{-1} is indicated.
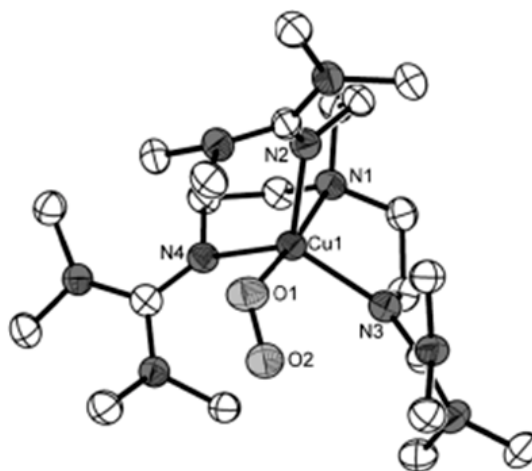
Figure 1.4 ORTEP diagram of $[TMG_3trenCu(O_2)]^+$. (tren = tris(2-aminoethyl)amine, TMG = tris(tetramethylguanidino))

In many cases the final structure is an η^2 complex but it may go through an initial

η^1 bonding form which then converts. This is a matter of some controversy in recent

literature. Roth[21] has published detailed kinetic isotope binding studies of $^{18}O_2$ and

concluded that "*the absence of spectrophotometrically detectable intermediates further

argues against the two-step mechanism for forming η^2 peroxide complexes*". In contrast,

Stahl[22] has performed calculations in contradiction to that in which both η^1 and η^2

binding are stable minima and the conversion of η^1 to η^2 occurs as a separate step in O_2 binding.

This is of clear importance to the reactivity of bound O_2. It is generally held that the η^1 form is more kinetically reactive form of O_2 binding. That was found to be the case in the binding of nitrile ligands to the complex $Mo(N^tBu(Ar))_3$[23] as shown in Scheme 1.7.
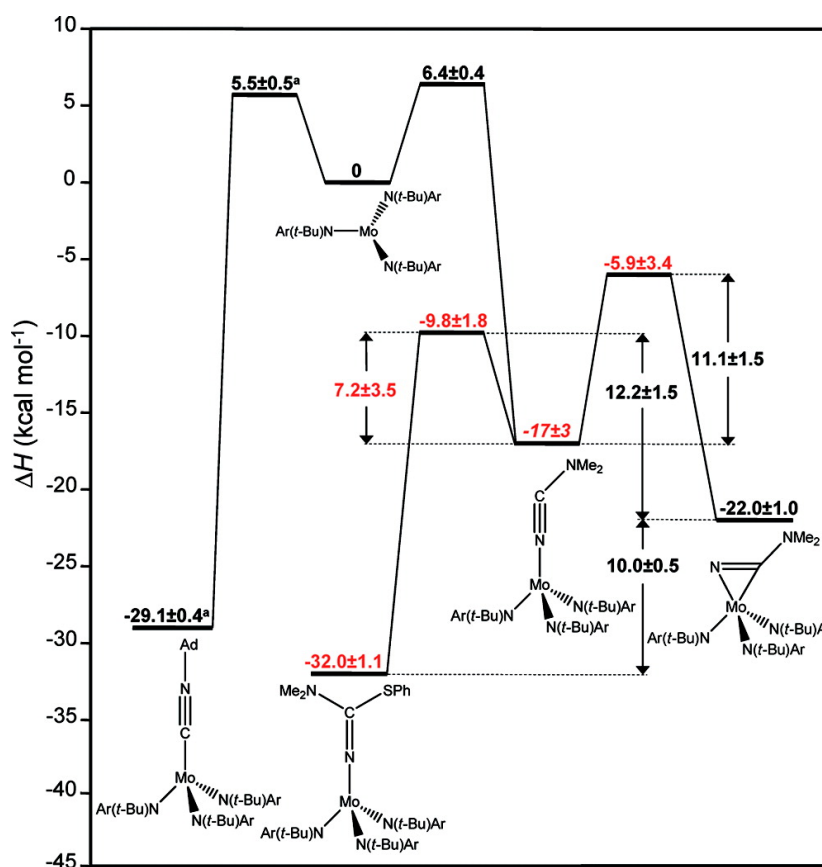
Scheme 1.7 Potential energy diagram for trapping of an η^1 nitrile product. (It has a relative energy of -17 ± 3 (calculated) which is closer to the transition state (-9.8 ± 1.8) than the η^2 form (22 ± 1 kcal/mol). (Drawing taken from ref 23)

For this complex with dimethyl cyanamide, the ultimate form of binding of the nitrile ligand is as an η^2 ligand as determined by its crystal structure. Stopped flow kinetic studies in this system were able to detect a two-step binding kinetic pattern with initial formation of an η^1 nitrile radical complex which subsequently converted (even at -78 °C)

to an η^2 form. The η^2 was known to react slowly with PhSSPh to cleave the S-S bond of the disulfide and form a ketinimide complex. At room temperature the half life for this reaction under typical conditions was on the order of one half hour for the η^2-preformed complex. However, it was discovered that if the PhSSPh was added (also at -78 ^{o}C) and present in ten fold excess, that the intermediate η^1 complex could be intercepted before it had the opportunity to form the η^2 complex which is totally inert at that temperature. This is summarized in the potential energy diagram shown in Scheme 1.7. It provides hope in catalyst design that a fleeting intermediate η^1 complex that is more reactive than its η^2 counterpart can be trapped under appropriate conditions.

The same type of effect could exist in O_2 chemistry. A question arises if the η^1 form of ligand binding will always be more reactive than the η^2 form. No definite answer can be given to that for all reactions, but in most cases the η^2 form is more stable and hence less reactive. In addition, the reaction products usually involve cleavage of one or both of the bonds to the metal, and so an η^1 bound form would be closer to the transition state for most reactions. This discussion is meant to highlight the importance of understanding the rate and mechanism for interconversion of η^2 and η^1 binding modes.

1.5 Palladium Catalysts bearing *N*-heterocyclic Carbene (NHC) Ligand(s) in Selective Oxidation

Different metal catalysts have been used in aerobic selective oxidation reactions, such as Ru,[24] Co,[25] and Cu[26]. Interest in using palladium compounds as catalysts in selective oxidation reactions started in the middle 1950s. After about 60 years of development, today palladium has become one of the most important catalysts in this area mainly because it is able to coordinate a large number of different organic substrates and

is highly effective in almost all fundamental organometallic reactions, including oxidative addition, reductive elimination, nucleophilic addition, insertion reactions, and β-elimination.[27] Its balance and stability of different oxidation states may be key to the apparent unique position of palladium in selective oxidation catalysis.

The ancillary ligands bound to Pd in oxidation catalysis play a major role, even though that role is often not fully understood. As is the case of the Wilkinson's complex[28] $Rh(PPh_3)_3Cl$, the starting complex is best viewed as a pre-catalyst and some loss of ligand to form a vacant site at the metal occurs to form $Rh(PPh_3)_2Cl$ which is best viewed as the true catalysts in the Wilkinson's system.

The same is likely true in oxidation chemistry, but it does not remove the interest in searching for new ligands and new pre-catalysts. One of the major moves in this area has been away from the use of popular phosphine ligands. For one thing, under oxidative conditions the formation of phosphine oxides is thermodynamically very favorable and high turnover numbers are generally not found if phosphine modified catalysts are used. One of the most popular ligands today is NHCs. These were first prepared by Wanzlick who synthesized the first salt-carbene complex in 1968.[29] However the area of NHCs did not become active until Arduengo isolated the first stable carbene in 1991 and low-valent carbene complexes of Ni and Pt in 1994.[30] Since then NHCs have been employed as useful ligands to coordinate a large range of transition-metals and tune the properties of catalysts in various reactions.[31]

As two electron donors NHCs resemble phosphines, but in many cases they form more thermally stable complexes with higher catalytic reactivity. NHCs are principally σ-donors and were historically thought to be poor π-acceptors.[32] This view has changed

over the past few years with the emergence of some computational studies.[33] The interactions between NHCs and transition metals can be modulated by tuning the steric and electronic components of NHCs. The steric factor can be varied by modifying the N-substitutes on NHCs, for example using bulky ligands, which can dramatically change the reactivity of NHC-ligated metal complexes. The electronic factor of NHCs can be modified by incorporation of heteroatoms into the backbone, variation of the ring size, and/or addition of electron-donating or electron-withdrawing groups.[34]
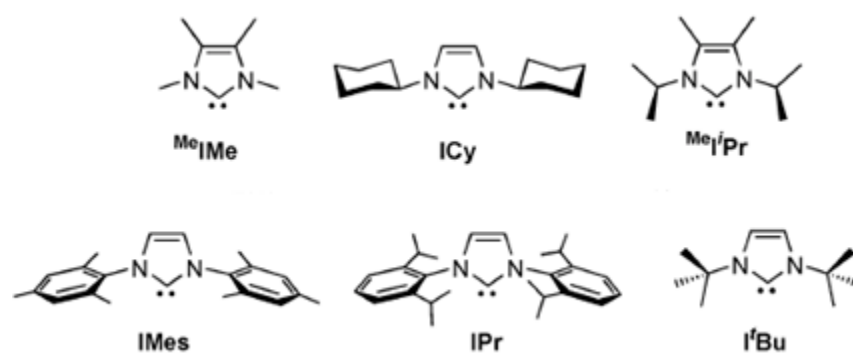
Figure 1.5 Some *N*-heterocyclic carbenes (NHC).[35] (Drawing taken from ref 35)

     Selective oxidation utilizing 14-electron Pd(0) complexes bearing NHC and/or PR_3 ligands is an area of growing interest.[36] These NHC-ligated palladium compounds are newly-risen catalysts to compete with traditional palladium catalysts, which are mainly simple palladium salts, such as palladium acetate and palladium chloride. However, little quantitative data on the kinetics and thermodynamics of oxygen binding to $Pd(L_1)(L_2)$ (L_1, L_2 = NHC and/or PR_3 ligands) systems have been reported, and the mechanistic study on these systems is not complete either.

1.6   Statement of Purpose

      The following chapters will discuss the thermodynamic, kinetic and mechanistic investigations in binding and activation of two oxidants (O_2 and MesCNO) with an emphasis on the comparison in the role of the binding mode in activation of oxidants. These investigations will add to the current reservoir of knowledge in activation of small molecules and organic oxidants in terms of exploring reaction mechanisms, finding environmental-friendly reaction conditions and discovering new efficient transition-metal catalysts. The ultimate goal of this work is to shed light on designing, modifying and optimizing transition-metal catalysts in selective oxidation reactions.

Chapter 2: Oxygen Binding to Pd(L$_1$)(L$_2$) (L$_1$ = NHC, L$_2$ = NHC or PR$_3$, NHC = *N*-Heterocyclic Carbene). Synthesis and Structure of a Paramagnetic *trans*-Pd(NHC)$_2$(η^1-O$_2$)$_2$ Complex

2.1 Background

Homogeneous catalytic oxidation is of fundamental importance, especially in its incarnation where molecular oxygen is used as oxidant.[37] In this context, catalytic oxidation utilizing 14-electron Pd(0) complexes bearing N-heterocyclic carbene (NHC) and/or PR$_3$ ligands is a fast growing area and under extensive studies over the past few years.[36]

In 1977 Otsuka and Yoshita[38] studied dioxygen binding to a series of palladium and platinum complexes with phosphine ligands. They found Pd(PPh(t-Bu)$_2$)$_2$, Pd(P(c-C$_6$H$_{11}$)$_3$)$_2$ and their platinum analogues are sensitive to air even in the solid state and dioxygen binds to these metal centers in a side-on (η^2) fashion. One of the complexes they discovered, Pd(PPh(t-Bu)$_2$)$_2$O$_2$, is known to be the only Pd^{II}-peroxo complex to undergo simple dissociation of O$_2$. In 2004 Stahl and co-workers[18] have reported that binding of O$_2$ to Pd(IMes)$_2$, yielding *cis*-Pd(IMes)$_2$(η^2-O$_2$), is rapid, even at -78 ^{o}C.

It is known that Pd(II) complexes serve as in situ precursors for active catalyst functioning by an oxidase pathway.[8, 39] This is shown in Scheme 2.1 for Pd(IMes)$_2$(η^2-O$_2$) in spite of the fact that to the author's knowledge Stahl and coworkers have not reported catalytic studies for this complex. As discussed later in Chapter 3, they have studied reactions of this complex with acetic acid to produce the first hydroperoxy Pd(II) complex[18] which would be an intermediate in the catalytic cycle in Scheme 2.1. Since then, a number of additional dioxygen-bound palladium (II) and platinum (II) complexes have been reported and all of them to date have been found in a side-on fashion.[40]
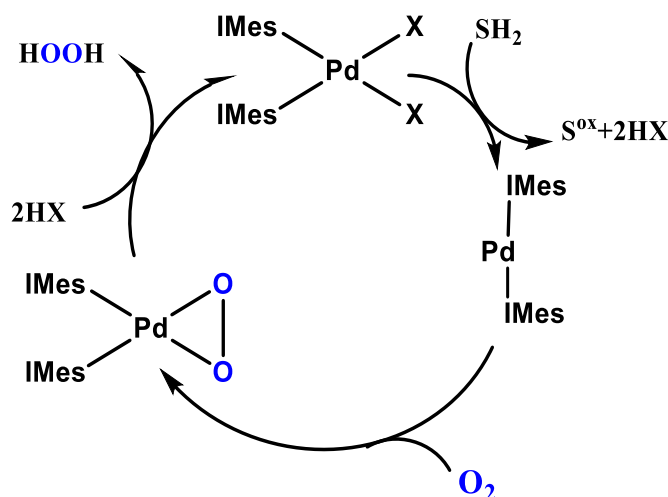
Scheme 2.1 Potential catalytic cycle of selective oxidation reaction catalyzed by Pd(IMes)$_2$(η^2-O$_2$) in oxidase pathway.

Dioxygen is known to be able to bind to single metal center in two ways: end-on (η^1) and side-on (η^2). However, the end-on (η^1) way of dioxygen is only well-known to bind to the Fe (III) center in hemoglobin, myoglobin and related proteins, and a recently discovered Cu(I) complex.[20] This raises the question: Is O$_2$ able to bind to Pd(L$_1$)(L$_2$) (L$_1$,L$_2$ = NHC and/or PR$_3$ ligands) systems in an end-on fashion and if so how will this change in binding mode affect its reactivity? The answer to that question is "yes", and this chapter reports the discovery of a novel dioxygen binding mode to Pd(L$_1$)(L$_2$) (L$_1$= NHC, L$_2$= NHC or PR$_3$, NHC = *N*-Heterocyclic Carbene), synthesis and structure of a paramagnetic *trans*-Pd(NHC)$_2$(η^1-O$_2$)$_2$ complex.

2.2   Results and Discussion

Discovery of the novel complexes *trans*-Pd(NHC)$_2$(η^1-O$_2$)$_2$ (NHC = IPr, SIPr) was fortuitous. This work began as a systematic study of the enthalpies of binding of O$_2$ to a series of Pd(PR$_3$)$_2$, Pd(PR$_3$)(NHC), Pd(NHC)$_2$ to see how sequential introduction of the NHC influenced the energetics of O$_2$ binding for a range of PR$_3$ and NHC compounds.

Initial studies of Pd(IPr)(PPh$_3$) were changed to Pd(IPr)(P-p-tolyl$_3$) due to the enhanced solubility of the later complex in toluene, and are described in the section below.

O$_2$ binding to Pd(IPr)(P-p-tolyl$_3$). The structures of both Pd(IPr)(P-p-tolyl$_3$) and its O$_2$ adduct Pd(IPr)(P-p-tolyl$_3$)(η^2-O$_2$) have been reported.[40d] Adding O$_2$ to solution of Pd(IPr)(P-p-tolyl$_3$) in toluene causes immediate bleach of the yellow solution as indicated in Figure 2.1. Even in solid state, Pd(IPr)(P-p-tolyl$_3$) loses its golden yellow color very quickly when exposed to O$_2$ and forms η^2-O$_2$ adduct as described in Eqn. (2.1). The oxygen adduct is best viewed as a distorted square planar Pd(II) complex of the peroxide ligand, which is typical of all O$_2$ binding modes to Pd(L$_1$)(L$_2$) systems reported to date.[40]

$$\text{Pd(IPr)(P-}p\text{-tolyl}_3) + O_2 \longrightarrow \text{Pd(IPr)(P-}p\text{-tolyl}_3)(\eta^2\text{-O}_2) \qquad (2.1)$$
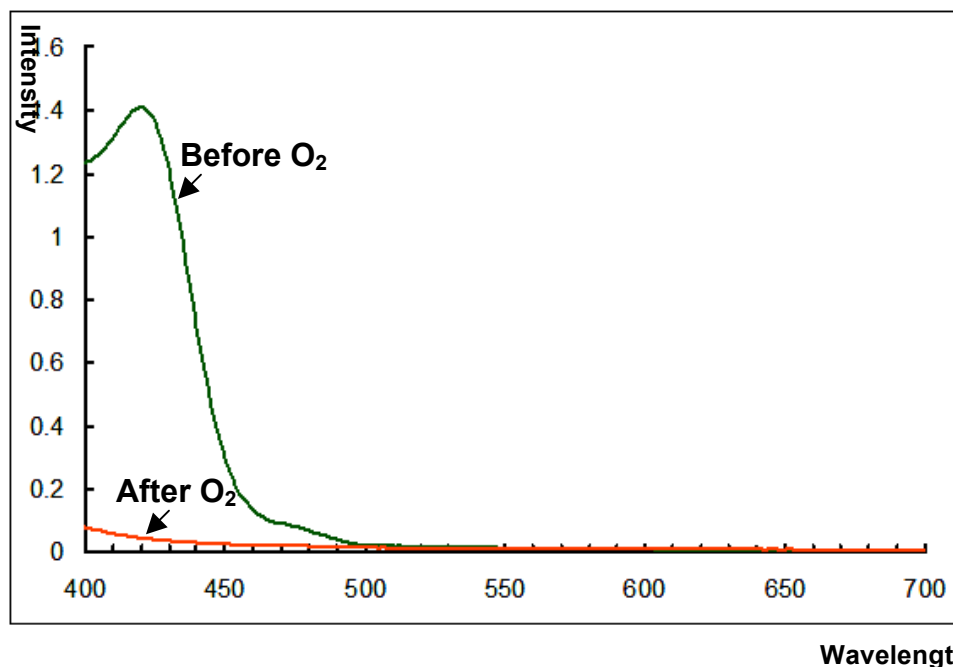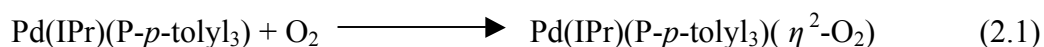
Figure 2.1 UV-Vis spectra in toluene of Pd(IPr)(P-p-tolyl$_3$) before (green spectrum) and after (orange spectrum) addition of O$_2$.

Stopped-flow kinetic studies, performed in collaboration with Professor Elena Rybak-Akimova at Tufts, confirmed that O_2 binding to Pd(IPr)(P-*p*-tolyl$_3$) was first-order in metal complex and in oxygen and that it was rapid in THF, even at -90 °C. As spectroscopically observed (see Chapter 2.4 Experimental Section), rapid bleaching occurs, and no intermediate complexes are detected on the way to forming the η^2-O_2 adduct. Activation parameters for O_2 binding, $\Delta H^{\ddagger} = 2.2$ kcal/mol and $\Delta S^{\ddagger} = -28$ cal/mol•K, are in keeping with a very small enthalpic barrier to O_2 addition. Solution calorimetric measurements performed in Miami yield a net enthalpy of O_2 addition to this complex $\Delta H = -26.2 \pm 1.9$ kcal/mol. The exothermic nature of this binding is in keeping with the essentially irreversible addition of O_2. This value can be compared to that of Vaska[41] who utilized temperature variation of K_{eq} and a van't Hoff plot to derive $\Delta H^o = -17.1$ kcal/mol and $\Delta S^o = -37$ cal/mol•K. Assuming similar values for ΔS^o, the net ΔG^o for binding in the Pd system should be an approximately 10 kcal/mol more favorable. This explains the reversible nature of O_2 addition to the Ir(I) complex compared to the irreversible nature of O_2 addition to the Pd(0) complex.

The combination of kinetic and thermodynamic data allows construction of the complete reaction profile for O_2 binding in this system as shown in Scheme 2.2.

In view of the low enthalpy of activation and high negative entropy of activation, the transition state for O_2 binding in the mixed NHC/phosphine system is ascribed to simple formation of the initial L_2Pd-O_2 contact interaction. The nature of initial binding of O_2 to Pd(IPr)(P(*p*-tolyl)$_3$), namely whether it occurs through an initial end-on η^1-adduct or side-on η^2-adduct, probably cannot be determined on the basis of experimental

data. Even at -90 ºC, the rate is so rapid and the enthalpy of activation is so low that trapping or observation of an intermediate could not be achieved.
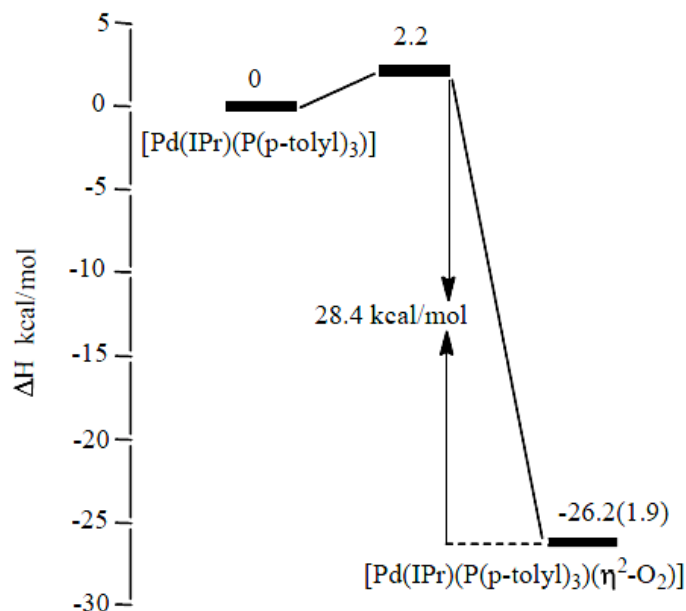
Scheme 2.2 Potential energy diagram (kcal/mol) derived for O_2 binding to Pd(IPr)(P-*p*-tolyl$_3$).

O_2 binding to Pd(IPr)$_2$. Extension of these physical studies from Pd(IPr)(PR$_3$) to Pd(IPr)$_2$ led to unexpected complexities. Qualitative visual studies showed that, at -78 ºC, binding of O_2 to Pd(IPr)$_2$ as described in Eqn. (2.2) was much slower than the rapid reaction of O_2 with Pd(IPr)(P(*p*-tolyl)$_3$) described above. In addition, at room temperature, binding of O_2 to Pd(IPr)$_2$ did not result in bleaching of its red-orange color but in development of a yellow-orange color instead (see Figure 2.2). The NMR spectrum of the bound adduct in Figure 2.3 was clearly in keeping with a paramagnetic and not a diamagnetic complex. Elemental analysis was in agreement with the Pd(IPr)$_2$(O$_2$)$_2$ formulation.

$$\text{Pd(IPr)}_2 + 2\ O_2 \longrightarrow \text{Pd(IPr)}_2(\eta^1\text{-O}_2)_2 \qquad\qquad (2.2)$$
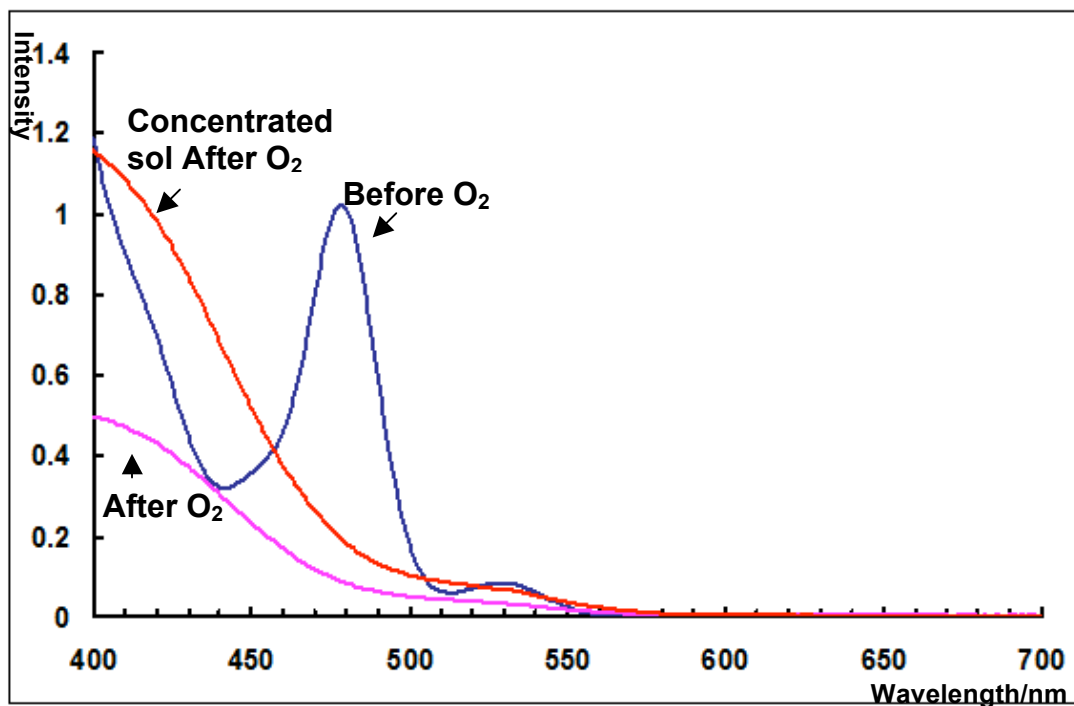
Figure 2.2 UV-Vis spectra in toluene of Pd(IPr)$_2$ before (blue spectrum) and after (pink spectrum) addition of O$_2$. The red spectrum is of a more concentrated toluene solution of Pd(IPr)$_2$O$_2$.
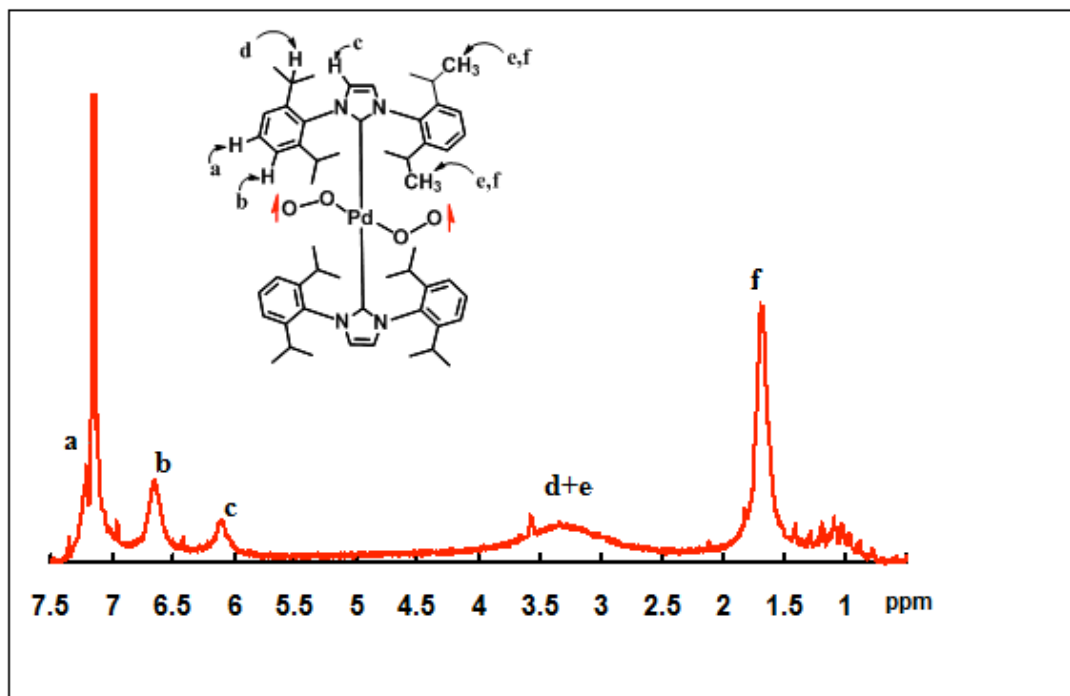
Figure 2.3 ^{1}H NMR spectrum of Pd(IPr)$_2$(η^1-O$_2$)$_2$ in C$_6$D$_6$.

The crystal structure[42, 43] of the complex (Figure 2.4) unambiguously shows oxygen binding consistent with a *trans*-Pd(IPr)$_2$(η^1-O$_2$)$_2$ composition with an average O-O bond length of 1.327(18) Å, in keeping with formulation of this complex as a bis-superoxo in which two paramagnetic O$_2$-ligands are bound to Pd(II). This result was surprising since binding of O$_2$ to Pd(L$_1$)(L$_2$) complexes studied to date had yielded exclusively *cis*-Pd(L$_1$)(L$_2$)(η^2-O$_2$) structures.
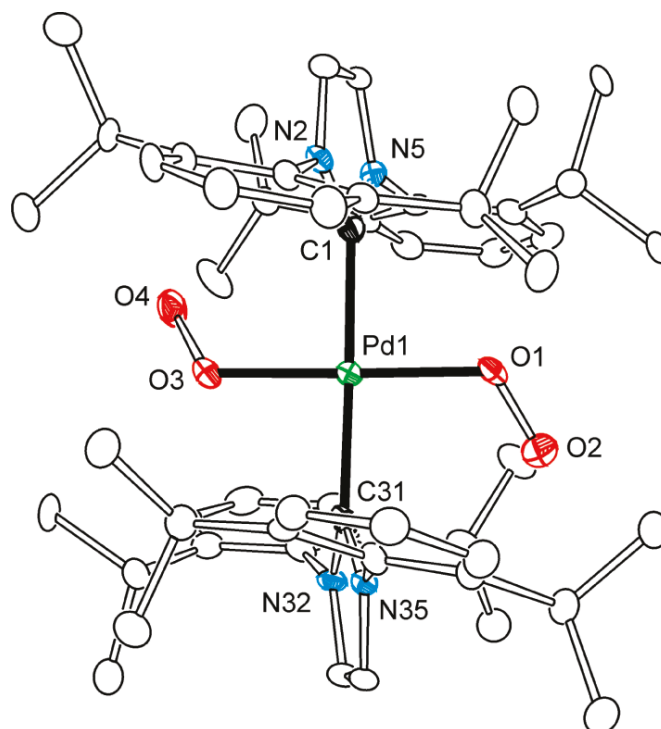
Figure 2.4 ORTEP diagram of *trans*-Pd(IPr)$_2$(η^1-O$_2$)$_2$, showing 30% thermal ellipsoid probability. Selected interatomic distances (Å) and angles (deg) are as follows: Pd-O1 = 2.010(8), Pd-O3 = 2.012(8), Pd-C1 = 2.059(11), Pd-C31 = 2.065(11), O1-O2 = 1.314(11), O3-O4 = 1.340(11), O3-Pd-O1 = 178.8(3), O3-Pd-C31 = 88.7(4), O1-Pd-C31 = 92.3(4), O3-Pd-C1 = 90.1(4), O1-Pd-C1 = 88.9(4), C31-Pd-C1 = 178.2(4).

There are only limited reports on η^1-O$_2$ complexes of Pd with some in situ spectroscopic characterization of Pd^{II} superoxides generated by KO$_2$[44] and a (^{F}PNP)PdO$_2$ complex[45] reported after our discovery[46]. Pd(IPr)$_2$(η^1-O$_2$)$_2$ is square planar, with *trans*-O$_2$ ligands formulated as superoxides on the basis of the average O-O distance of 1.327(18)

Å, which is closer to the O-O bond distance value of 1.280(3) Å reported in a Cu superoxide complex[20] and 1.293(2) Å reported in the (^{F}PNP)PdO$_2$ complex[45] than to the value of 1.443 Å reported for the Stahl complex.[18] The C31-Pd-C1 = 178.2(4) angle shows the nearly linear nature of binding of the *trans*-IPr ligands.

Study on Pd(IPr)$_2$(OOH)$_2$. As a second method of characterization of the complex a method to prepare a derivative of it was sought. The paramagnetic nature of a *trans*-Pd(IPr)$_2$(η^1-O$_2$)$_2$ and its formulation as a bis-superoxide complex with spin density on the terminal O$_2$ atoms suggested that it might readily undergo H atom transfer reactions, as shown in Eqn. (2.3). Since the H-Mo bond in HMo(Cp)(CO)$_3$(Cp = η^5-C$_5$H$_5$) (65 kcal/mol) is weaker than the ROO-H bond (85 kcal/mol for H$_2$O$_2$), hydrogen atom transfer from molybdenum to oxygen should be thermodynamically favorable.[47]
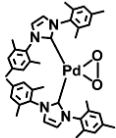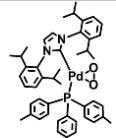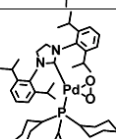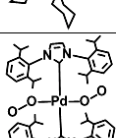
The reaction was performed and found to be rapid and quantitative at room temperature. Attempts to grow X-ray-quality crystals of *trans*-Pd(IPr)$_2$(OOH)$_2$ proved unsuccessful in spite of elemental analysis, NMR, and IR spectroscopic evidence for its formation. However, for the saturated NHC analogue SIPr, this proved possible, and the crystal structure of the obtained *trans*-Pd(SIPr)$_2$(OOH)$_2$ complex is shown in Figure 2.5.[42,38] Only a few structures of the L$_n$Pd(OOH) type have been reported,[49] and we are unaware of any Pd(L)$_n$(OOH)$_2$ of Pd(II).

(2.3)
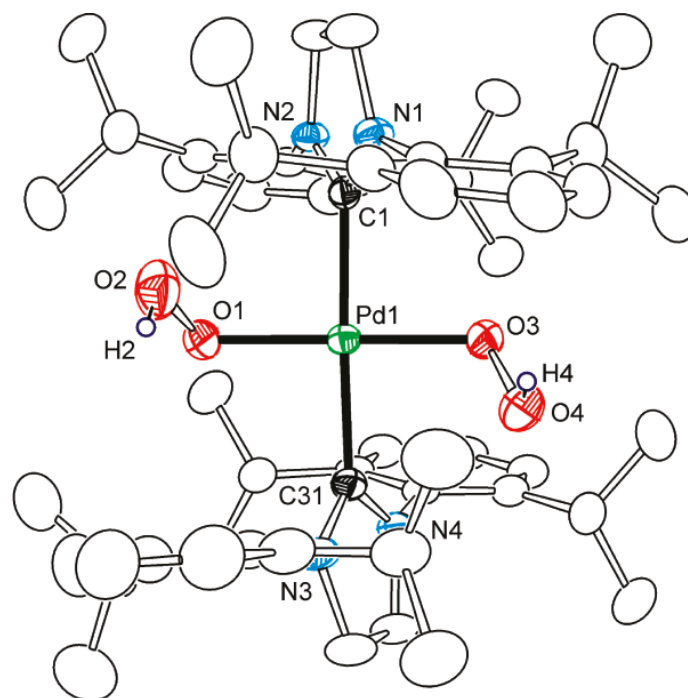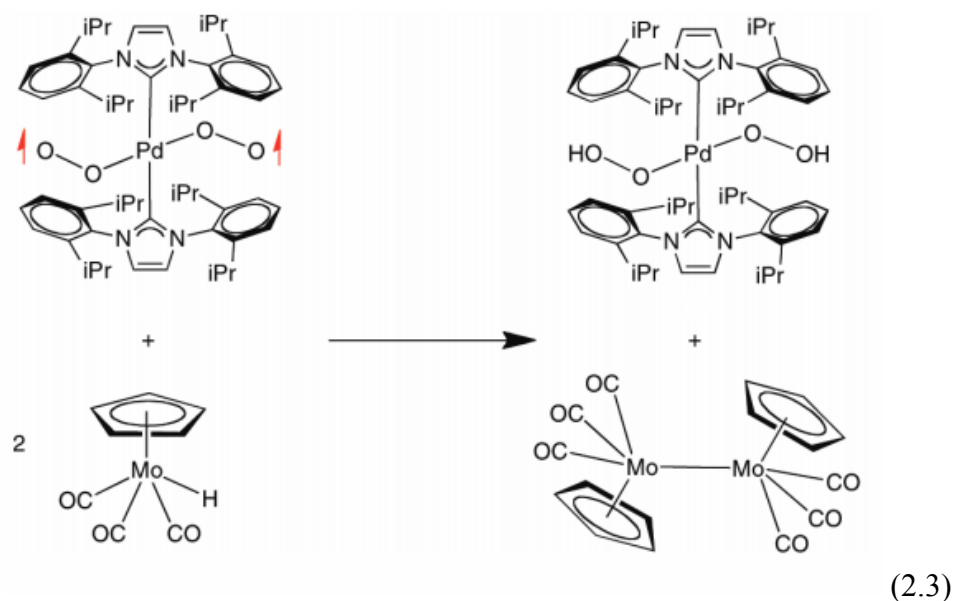
Figure 2.5 ORTEP diagram of *trans*-Pd(SIPr)$_2$(OOH)$_2$, showing 30% thermal ellipsoid probability. Selected interatomic distances (Å) and angles (deg) are as follows: Pd-O1 = 2.0172(16), Pd-O3 = 1.9925(16), Pd-C1 = 2.065(2), Pd-C31 = 2.064(2), O1-O2 = 1.392(3), O3-O4 = 1.452(2), O3-Pd-O1 = 177.38(7), O3-Pd-C31 = 87.98(8), O1-Pd-C31 = 91.67(8), O3-Pd-C1 = 89.72(7), O1-Pd-C1= 90.62(7), C31-Pd-C1 = 177.68(8).

Magnetic property of Pd(IPr)₂(O₂)₂. Magnetic susceptibility studies on the isolated

solid of Pd(IPr)$_2$(O$_2$)$_2$ showed it to have 1.8 unpaired electrons as measured using a Guoy

balance at FIU with permission of Professor Konstantinos Kavallieratos. A more detailed

study of the magnetic properties of this complex was performed by Professor Karl

Wieghardt of the Max Planck Institute for Bioinorganic Chemistry (Mülheim) and is

included in Appendix.

Table 2.1 Summary of enthalpy measurement of O$_2$ addition to a series of Pd(L$_1$)(L$_2$)
(L$_1$= NHC, L$_2$= NHC or PR$_3$).

	Reactant	Product	Value of Enthalpy (kcal/mol)
O$_2$	Pd(IMes)$_2$		-27.9±1.5[a]
	Pd(IPr)(*p*-tol$_3$)		-26.2±1.9[a]
	Pd(SIPr)(PCy$_3$)		-25.6±0.6[a]
	Pd(IPr)$_2$		-24.0±0.4[a]

[a.] Measurements were done in toluene solution.

Thermodynamic studies on O$_2$ binding to Pd(L$_1$)(L$_2$) system. The enthalpies of O$_2$

addition to several complexes were measured by solution calorimetry in toluene solution

and are summarized in Table 2.1. It is somewhat surprising that binding of two moles of

O$_2$ (which is irreversible at room temperature) has the lowest enthalpy of binding of all

the systems studied. It would be expected that the entropy of binding of two moles of

gaseous O$_2$ would be highly unfavorable--however based on the structure of the complex,

it might be expected that there would be less loss of entropy in the ligand system for the *trans*-Pd(NHC)$_2$ framework. As the geometry of the complex approaches that of a *cis*-complex, steric interlocking of the two NHC ligands might be expected to cause a large unfavorable entropic interaction.

Finally it should be mentioned that the enthalpy of binding of O$_2$ to Pd(P^{t}Bu$_3$)$_2$ was attempted. The thermogram is shown in Figure 2.6 below. The data in Figure 2.6 shows an initial enthalpy of reaction in the range of $\approx$ - 30 kcal/mol, followed by a large exothermic signal of $\approx$ - 120 kcal/mol. This is attributed to initial binding of O$_2$ in moderately exothermic reaction, followed by an induction period and then the more exothermic oxidation one of the phosphine ligands to a phosphine oxide. There is literature precedent for this type of reactivity.[38] For that reason this reaction was not studied further, but it is of note that while the bis-NHC, and mixed NHC, PR$_3$ complexes are highly stable to auto oxidation, bis-PR$_3$ complexes are not.
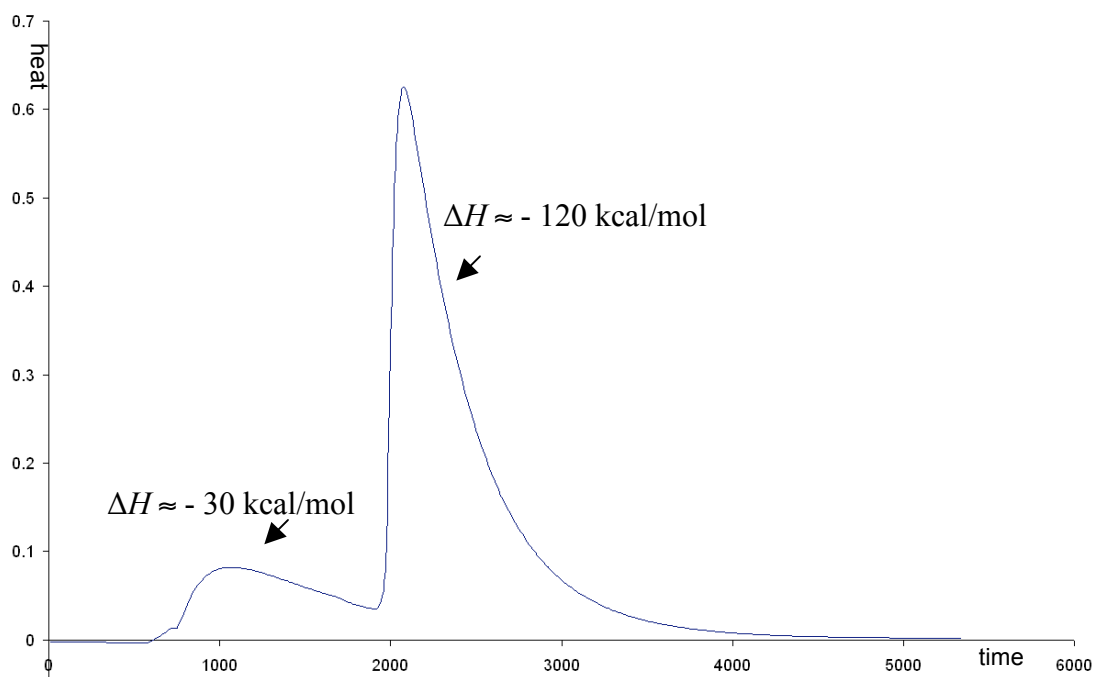
Figure 2.6 Thermogram from Calvet of Pd(P^{t}Bu$_3$)$_2$ with O$_2$.

Calculations on O₂ Binding to Pd(IPr)₂ and Pd(IMes)₂. In collaboration with Professor Rajeev Prabhakar, and with the help of Charles L'Hermitte, computational studies were performed for the full ligand systems Pd(IPr)₂ and Pd(IMes)₂. In this case the ligand set was not truncated--reduced in size to allow speedier computation. There would be no point in that, since it is exactly the large steric bulk that makes the difference in these reactions. Stahl, Landis, and coworkers have performed calculations of the "pruned off" ligand IMe in which the bulky arene groups of the NHC are replaced by methyl groups. However, the enthalpies and entropies computed do not present a consistent picture and it is felt that at this time while minimum energy configurations can be computed, the energetics of ligand binding requires more accuracy than current calculations allow.

Mechanism of O₂ binding to Pd(L₁)(L₂) system (L₁= NHC, L₂= NHC or PR₃). One significant challenge that remains in using Palladium complexes with NHC ligand(s) as catalysts in aerobic selective oxidation is that low valent Pd(0) complexes tend to decompose by losing their ligands and aggregating into inactive palladium black. This problem can be addressed by stabilizing these Pd(0) complexes with stronger ligands, for example pincer ligands,[21b] and by increasing the rate of oxygenation to the Pd(0) center, which makes it important to study the mechanism of O₂ binding to the palladium center.

The sensitivity of reaction product to the sterics of the NHC is highlighted, where the change from IMes to IPr results in quite different reactivities with respect to O₂ binding. Stahl, Landis, and co-workers[22] have performed calculations for O₂ binding to Pd(IMe)₂ using the truncated ligand "IMe" (IMe = 1,3-dimethylimidazol-2-ylidene) to allow faster computation. In view of the observed differing reactivities as a function of

ligand sterics, computational studies were begun on the minimum energy structures for presumed initial end-on binding of one O_2 molecule.

As determined previously for Pd(IMe)$_2$, the lowest energy structure proved to be a paramagnetic T-shaped intermediate with one O_2 bound end-on as superoxide. The optimized structures at the B3LYP/Lanl2dz level of theory are shown in Figure 2.7 for Pd(IPr)$_2$(η^1-O$_2$) (Ia), Pd(IMes)$_2$(η^1-O$_2$) (Ib), and Pd(IPr)(PPh$_3$)(η^1-O$_2$) (Ic). These structures have been oriented to show, for each complex, the maximum amount of free space available as "wiggle room" for O_2. It is clear from these views that the aperture available for O_2 binding and subsequent rearrangement increases on going from Ia to Ib to Ic.
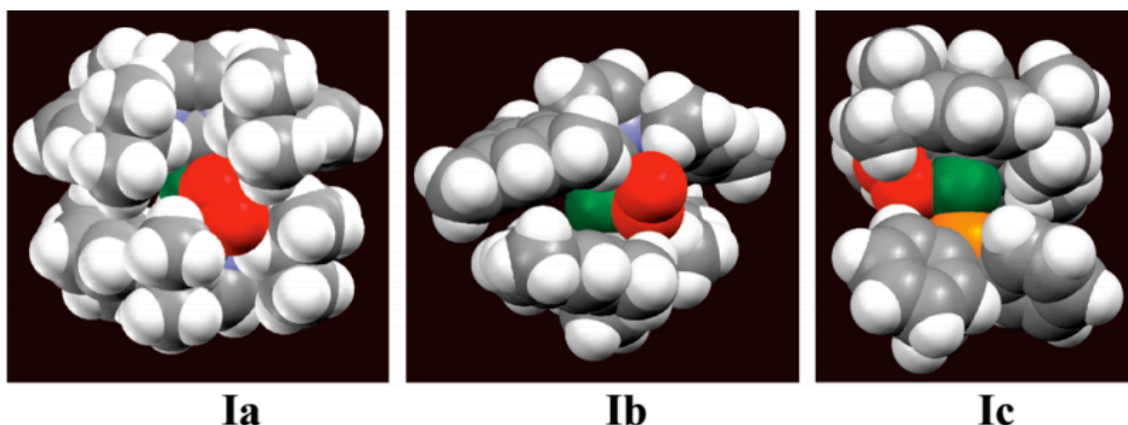
Figure 2.7 Computed geometries for η^1-O$_2$ (red) binding to Pd (green) to paramagnetic T-shaped complexes (η^1-O$_2$)Pd(IPr)$_2$ **Ia**, (η^1-O$_2$)Pd(IMes)$_2$ **Ib**, (η^1-O$_2$)Pd(IPr)(PPh$_3$) **Ic**. Showing increased mobility of O_2 to go to (η^2-O$_2$)Pd(L)$_2$. Atomic dimensions are the atomic van der Waals radii. Pd, green; O, red; N, blue; C, gray; H, white; P, orange.

A plausible general mechanism for stepwise binding of O_2 to Pd(NHC)$_2$ is shown in Scheme 2.3. This is proposed to involve, as originally delineated by Stahl,[16,22] initial formation of a reactive intermediate η^1-O$_2$ complex. Complex I is a branching point and can undergo O_2 loss to regenerate A, rearrange to form the expected diamagnetic η^2-O$_2$

complex B, or add a second O_2 to form paramagnetic C. Once formed, applying vacuum does not regenerate A from either B (NHC = IMes) or C (NHC = IPr), and these steps are effectively irreversible at room temperature and below.

The product distribution in Scheme 2.3 is determined by the relative magnitudes of k_2 and k_3, which may depend critically on the specific ligand system involved. Examination of Figure 2.7 presents a qualitative picture of how the rate of the intramolecular cyclization step k_2 may be retarded for $Pd(IPr)_2(\eta^1\text{-}O_2)$ (Ia), thus allowing trapping by additional O_2 in step k_3. Comparison between complex B and C shows that B is more thermodynamically (enthalpically) favorable and C is more dynamically (entropically) favorable.
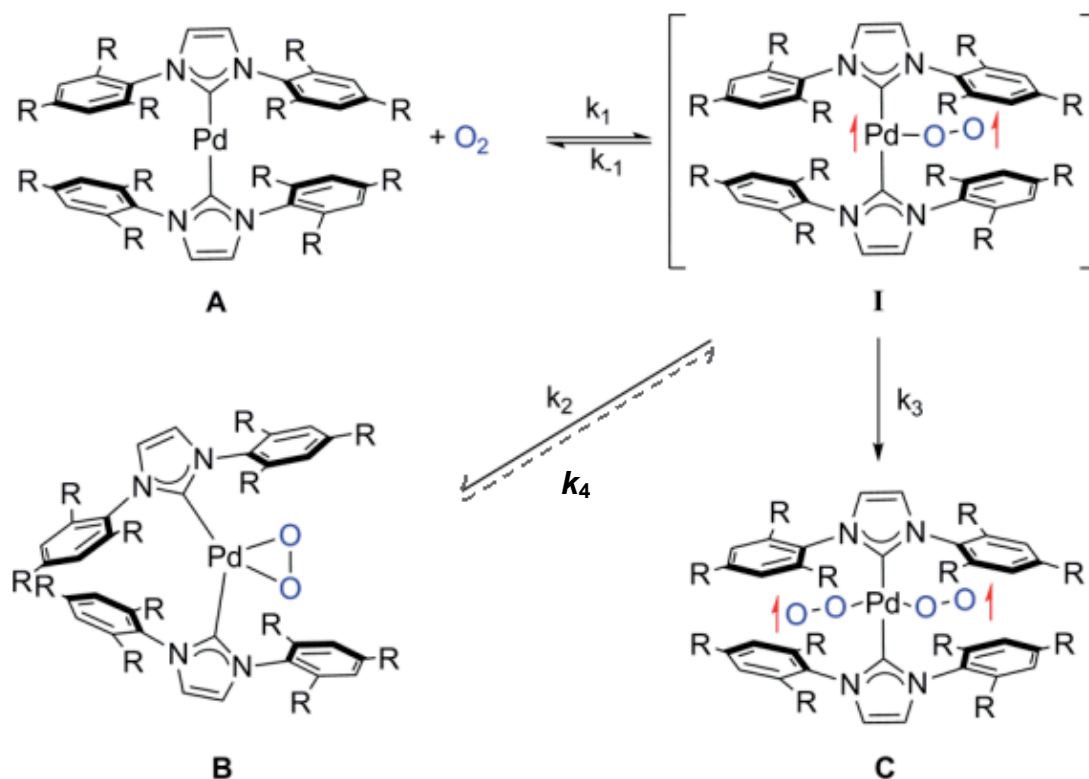
Scheme 2.3 Proposed mechanism for the reaction involving $Pd(NHC)_2$ and O_2.

For NHC = IPr, at low temperature (i.e. -90 to -70 $^{\circ}$C, detail in Chapter 3) entropy does not contribute significantly to ΔG. The rate of conversion from peroxide to superoxide step k_4 is effectively suppressed and B is formed exclusively as a thermodynamically-favored product. Whereas at higher temperature (i.e. above -70 $^{\circ}$C) the ratio of k_4 to k_2 increases as temperature elevates because entropy is playing a more important role in ΔG at high temperature than at low temperature. More palladium complex falls into the well of intermediate Pd(IPr)$_2$(η^1-O$_2$), which quickly adds a second mole of O$_2$ and forms Pd(IPr)$_2$(η^1-O$_2$)$_2$. Once this final product forms, applying vacuum will not convert it back to A or any other form. For NHC = IMes, the ration of k_2 to k_3 is big due to its intrinsic less steric property. Therefore even at -78 $^{\circ}$C, B forms without observing any two-stage process of O$_2$ binding.

2.3   Conclusions

The reactivity of a number of two-coordinate Pd(L$_1$)(L$_2$) (L$_1$ = *N*-heterocyclic carbene (NHC) and L$_2$ = NHC or PR$_3$) complexes with O$_2$ has been examined. Stopped-flow kinetic studies show that O$_2$ binding to Pd(IPr)(P(*p*-tolyl)$_3$) to form *cis*-Pd(IPr)(P(*p*-tolyl)$_3$)(η^2-O$_2$) occurs in a rapid, second-order process. The enthalpy of O$_2$ binding to the Pd(0) center has been determined by solution calorimetry to be - 26.2 ± 1.9 kcal/mol.

Extension of this work to the bis-NHC complex Pd(IPr)$_2$, however, did not lead to the formation of the expected diamagnetic complex *cis*-Pd(IPr)$_2$(η^2-O$_2$) but to paramagnetic *trans*-(Pd(IPr)$_2$(η^1-O$_2$)$_2$. This novel oxygen binding mode to low valent palladium(0) complexes was discovered as the first reported of its kind. This bis-(η^1-O$_2$)-bound complex Pd(IPr)$_2$(η^1-O$_2$)$_2$ was fully characterized spectroscopically and chemically by X-ray structure, NMR, elemental analysis and magnetic susceptibility. Pd(IPr)$_2$(η^1-

$O_2)_2$ is a bi-radical. A combination of theoretical and experimental approaches were used to generate a scheme for O_2 binding to $Pd(NHC)_2$ in which the sterics of ligands around palladium center plays a crucial role. The comparison between Stahl's $Pd(IMes)_2$ and $Pd(IPr)_2$ showed that these two complexes, in spite of being quite similar in structure, display greatly different properties when reacting with O_2. This confirms what is already known, that synthetic studies involving ligand variation can yield unexpected results on occasion.

2.4 Experimental

A. Synthetic and Thermochemical Experiments.

General Methods. Unless stated otherwise all reactions were carried out inside an MBraun or Vacuum Atmospheres glovebox or utilizing Schlenk tube techniques under inert atmosphere conditions. Solvents were purified by distillation under argon from an appropriate drying agent into flame dried glassware. NMR spectra were recorded on either a Burker 400 MHz or a Bruker 300 MHz NMR spectrometer. Calorimetric measurements were performed using a Setaram Calvet C-80 or modified Guild Solution Calorimeter as described previously.[50] Elemental analyses were performed at London Metropolitan University. Magnetic susceptibility measurements were made using a Johnson-Matthey MSB-Auto Magnetic Susceptibility Balance and diamagnetic corrections made according to the literature.[51] Pd-NHCcomplexes and their O_2 derivatives were prepared by methods strictly analogous to those reported previously.[40d] Representative procedures for preparation and reactions of new complexes are described below.

NMR Studies of Reaction of Pd(NHC)$_2$ (NHC = IPr, SIPr) and O$_2$ at Room Temperature. A sample of 5 mg Pd(IPr)$_2$ was weighed into an NMR tube in the glove box and dissolved in 0.5 mL C$_6$D$_6$ fitted with a screw cap and Teflon-lined silicone rubber septum. An NMR spectrum was taken and then 3ml of pure O$_2$ gas was added to the tube and it was shaken. A second NMR spectrum recorded 16 minutes later showed complete disappearance of the signals due to the diamagnetic starting material and conversion to a paramagnetic product as shown in Figure 2.3. ^{1}H NMR (400MHz, C$_6$D$_6$): δ = 7.16 (t, under peak of C$_6$D$_6$ at 7.16ppm, 4H), 6.65 (s, broad, 8H), 6.11 (s, broad, 4H), 3.29 (s, very broad, 32H), 1.67 (s, broad, 24H).

The spectrum of starting material Pd(IPr)$_2$ and product Pd(IPr)$_2$(O$_2$)$_2$ are shown as an overlay in Figure 2.8.
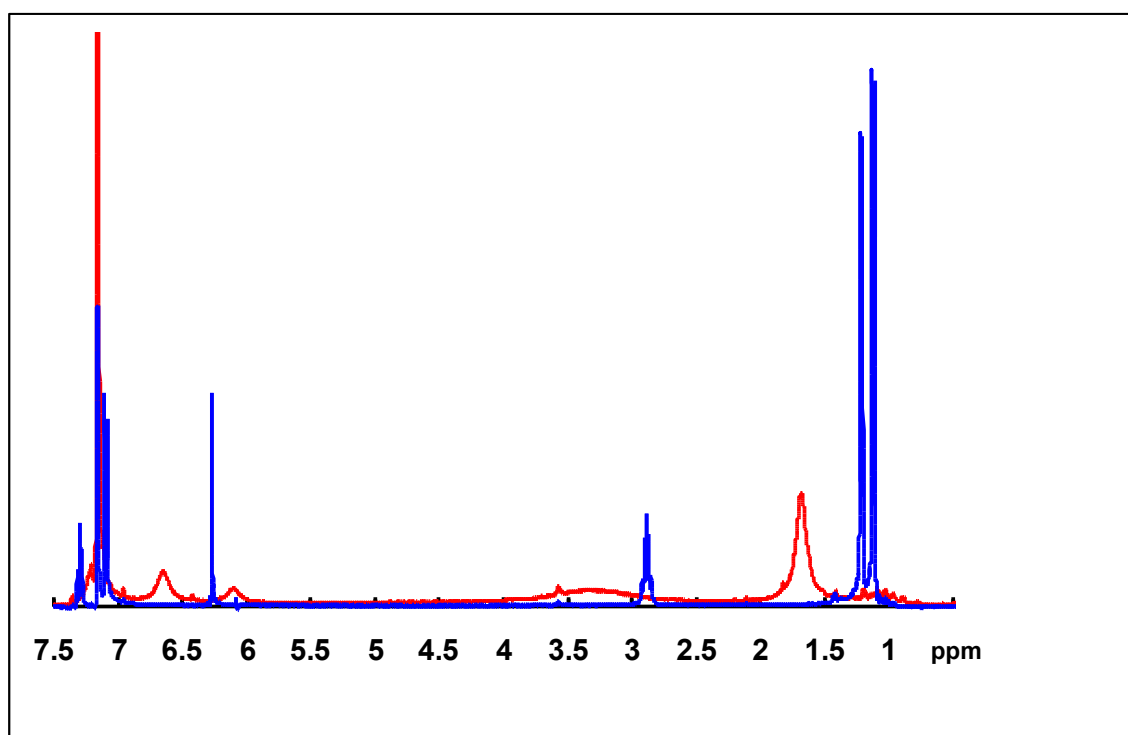
Figure 2.8 ^{1}H NMR spectrum in C$_6$D$_6$ of Pd(IPr)$_2$ before addition of O$_2$ (blue spectrum) and after addition of O$_2$ (red spectrum). The red spectrum has been multiplied by 4 due to its broad nature.
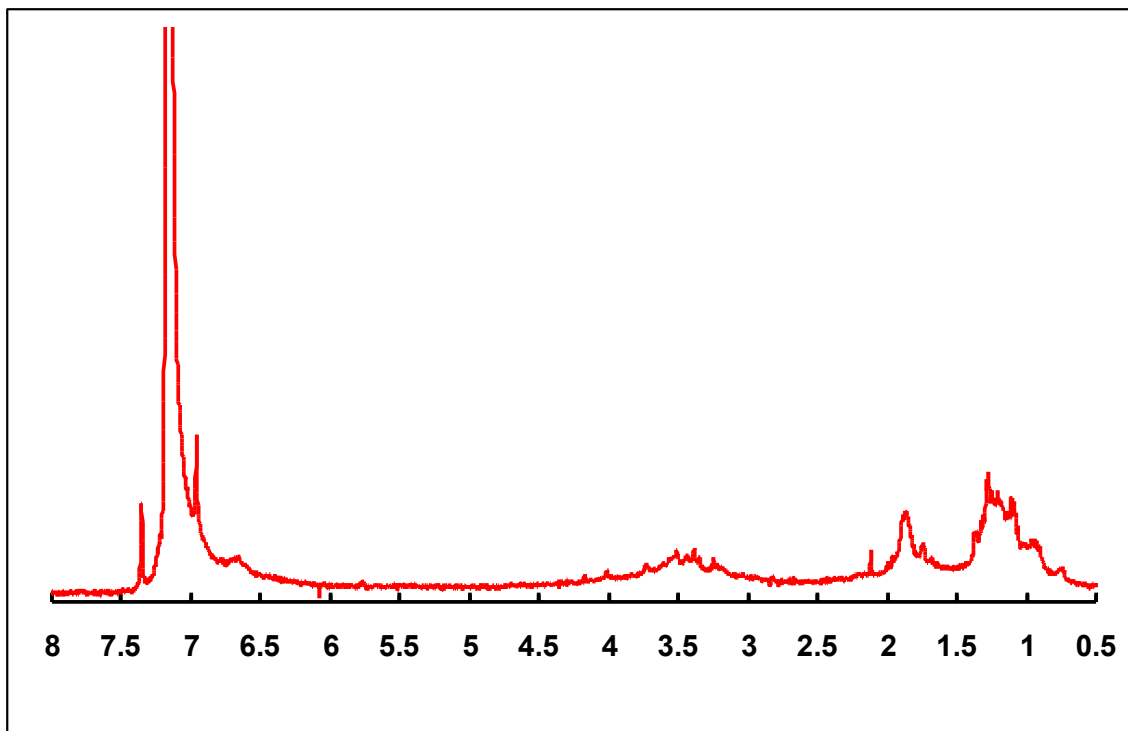
Figure 2.9 ^{1}H NMR spectrum in C_6D_6 of Pd(SIPr)$_2$(O$_2$)$_2$.

In a similar manner, a solution of Pd(SIPr)$_2$ in C_6D_6 was prepared inside the glovebox and the Schlenk flask containing the solution was brought out of the glovebox. Pure O$_2$ was added to the flask. After shaking the flask for a few minutes, the color of the solution changed from orange-red to orange-yellow. Excess O$_2$ was evacuated out of the flask. The NMR spectrum of Pd(SIPr)$_2$(O$_2$)$_2$ in C_6D_6 is shown in Figure 2.9. For both Pd(IPr)$_2$(O$_2$)$_2$ and Pd(SIPr)$_2$(O$_2$)$_2$ evacuation to dryness and redissolving in C_6D_6 did not result in regeneration of the starting Pd(NHC)$_2$ complex.

Synthesis and Recrystallization of *trans*-Pd(IPr)$_2$(O$_2$)$_2$. In a Schlenk tube in the glovebox, 100 mg of Pd(IPr)$_2$ was dissolved in 3 mL of THF and then taken out of the glovebox. It was exposed to one atmosphere of pure O$_2$ for 10 minutes and evaporated to dryness and dried *in vacuo* overnight. The complex so formed is spectroscopically and analytically pure in essentially quantitative yield. Elemental analysis was performed on

this sample: Chemical Formula: $C_{54}H_{72}N_4O_4Pd$; Molecular Weight: 947.5: Theoretical: C, 68.44; H, 7.66; N, 5.91; Found: C, 68.58; H, 7.71; N, 5.82.

Magnetic susceptibility measurements were performed on a sample that had been further recrystallized (in $\approx$ 40 % yield) by filtering a saturated heptane solution into a Schlenk tube, reducing the volume and storing overnight in the freezer at -20 ^{o}C. Crystals suitable for X-ray crystallography were obtained by recrystallization from hexane.

Qualitative Study of Rate of Reaction of Pd(IPr)$_2$ and O$_2$ (1 atm) at -78 ^{o}C in Toluene Solution. A stock solution of 49 mg recrystallized Pd(IPr)$_2$ was prepared in 5 mL toluene in the glovebox under an argon atmosphere and divided equally between two identical Schlenk tubes. The tubes were taken from the glove box and were identical in their yellow-orange color. One of the tubes was exposed to 1 atm of O$_2$ and shaken for approximately 5 minutes. During this time the color of the solution changed to the red-orange color characteristic of Pd(IPr)$_2$(O$_2$)$_2$. Both tubes were then placed in a dry-ice/acetone bath at -78 ^{o}C and their colors again compared. At that time the atmosphere of the tube that had not been exposed to O$_2$ was evacuated and filled with pure O$_2$ gas. The solution was shaken but kept at -78 ^{o}C. During a period of 5-10 minutes there was no visible color change indicating a lack of reaction. The tube was then taking from the dry ice bath, and allowed to slowly warm to room temperature. During warm up at a temperature estimated to be T $\approx$ - 40 ^{o}C the color of the tube originally under Ar began to change color and by the time it had reached T $\approx$ 0 ^{o}C it matched in color the authentic sample of Pd(IPr)$_2$(O$_2$)$_2$. Identical experiments performed with Pd(IPr) (P-*p*-tolyl$_3$) and

Pd(IMes)$_2$ showed that reaction with O$_2$ was rapid even at -78 ^{o}C and only for Pd(IPr)$_2$ did we observe a slow rate of reaction in a dry ice/acetone bath.

Synthesis of Pd(IPr)$_2$(OOH)$_2$ and Pd(SIPr)$_2$(OOH)$_2$. In a test tube 0.053g Pd(IPr)$_2$ was dissolved in 4 mL of C$_6$D$_6$ inside the glovebox. Then the tube was brought out of the glovebox and pure O$_2$ was added to the solution. The color of the solution changed from fluorescent orange to orange-red. After evacuating the excess O$_2$, the tube was again taken into the glovebox and 0.0255g HMo(CO)$_3$Cp solid was added to the solution. The solution immediately turned to the red-purple color characteristic of [Mo(CO)$_3$Cp]$_2$. The solution was filtered into an NMR tube and showed quantitative conversion of HMo(CO)$_3$Cp to [Mo(CO)$_3$Cp]$_2$ with a chemical shift near 4.65 ppm as shown in Figure 2.10. A clear red solution was obtained. Peaks assigned to Pd(IPr)$_2$(OOH)$_2$: ^{1}H NMR (400MHz, C$_6$D$_6$): δ = 7.28 (t, 4H), (d, under peak of C$_6$D$_6$ at 7.16ppm, 8H), 6.42 (s, 4H), 3.99 (s, 2H), 3.03 (sept, 8H), 1.17 (d, 24H), 1.00 (d, 24H) (Different chemical shifts of protons e and f depend on their relative position to the Pd metal center.)

Attempts to grow X-Ray quality crystals of Pd(IPr)$_2$(OOH)$_2$ were not successful. Similar procedures were utilized to synthesize Pd(SIPr)$_2$(OOH)$_2$ which yielded X-Ray quality crystals upon slow evaporation of a saturated heptane solution kept in a vial inside the glovebox.
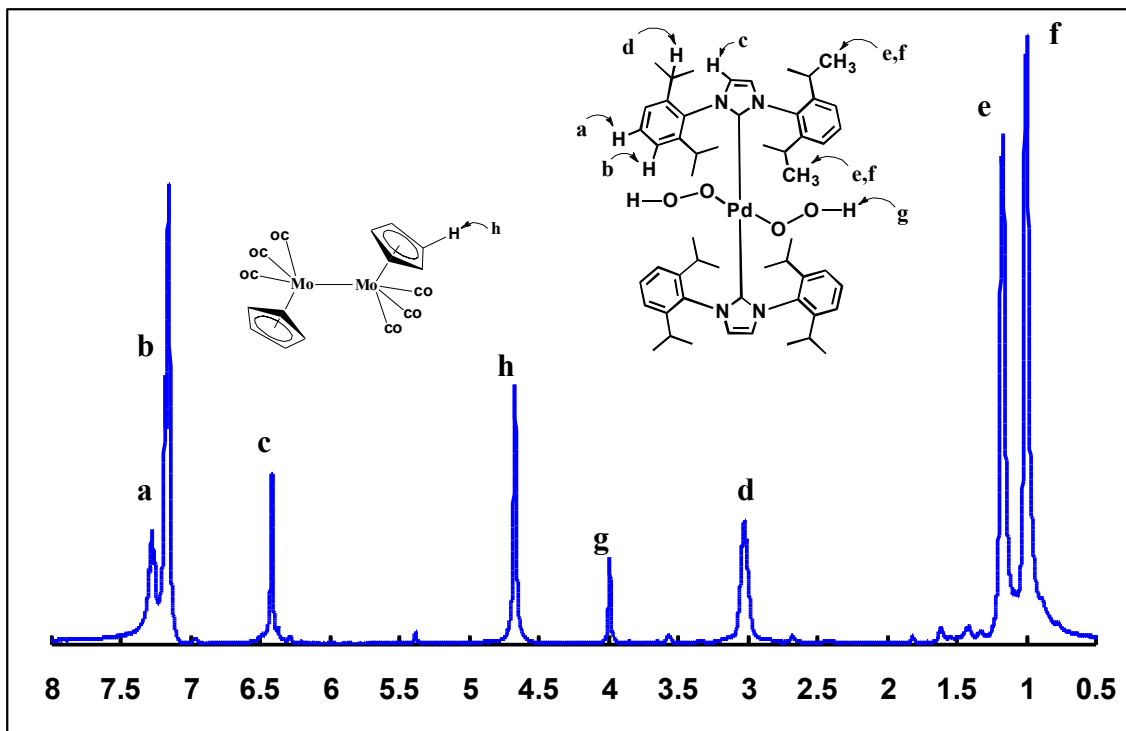
Figure 2.10 ^{1}H NMR spectrum of the reaction in C_6D_6 of $Pd(SIPr)_2(O_2)_2$ and $HMo(CO)_3Cp$.

B. Stopped-Flow Kinetic Measurements

THF solutions of the reagents were prepared in a MBraun glovebox under Argon and placed in Hamilton gastight syringes. Time-resolved spectra (400-650 nm) were acquired at temperatures from -90 to -75 °C using a Hi-Tech Scientific (Salisbury, Wiltshire, U.K.) SF-61DX2 Multi-Mixing CryoStopped-Flow Instrument and a J&M TIDASDAQ diode array detector with a Hi-Tech Scientific LHT50 tungsten lightsource. The stopped-flow instrument was equipped with stainless steel plumbing, a 1.00 cm^3 stainless steel mixing cell with sapphire windows, and an anaerobic gas-flushing kit. The temperature in the mixing cell was maintained to 0.1 °C, and the mixing time was 2-3 ms. The driving syringe compartment and the cooling bath, filled with ethanol (Fisher), were flushed with argon before and during the experiments, using anaerobic kit flush lines. All flow lines of the SF-61DX2 instrument were extensively washed with degassed, anhydrous toluene

before charging the driving syringes with reactant solutions. The reactions were studied

by rapid scanning spectrophotometry under stoichiometric conditions (1:1 molar ratio).

All of the experiments were performed in a single-mixing mode of the instrument, with a

1:1 (v/v) mixing ratio.
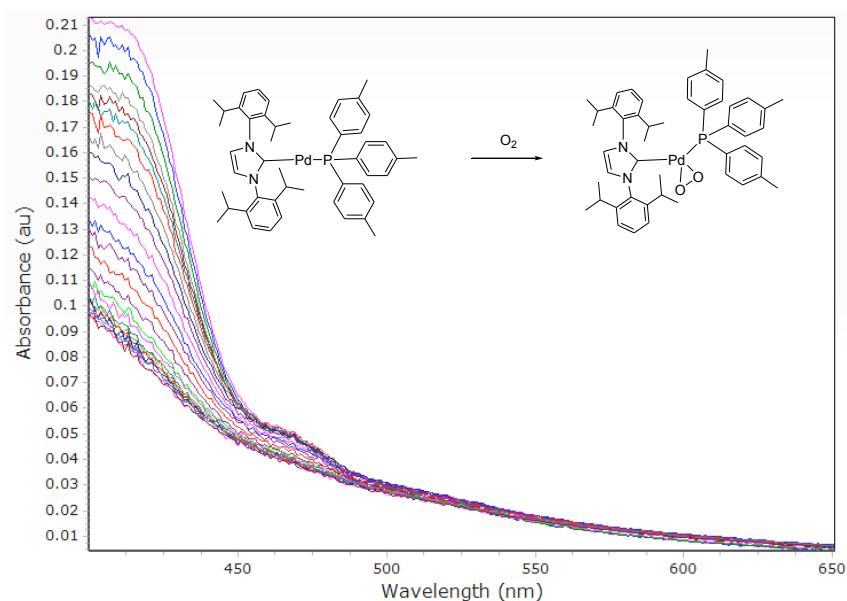
Figure 2.11 Diode array spectrum of O_2 (0.125mM) binding to Pd(IPr)(P(p-tolyl)$_3$) (0.122 mM) at -90 °C, all concentrations reported after mixing. Reaction kinetics were measured by monitoring the decay at $\lambda_{max} = 414$ nm.

A series of three to six measurements at each temperature gave an acceptable

standard deviation (within 10%). Data analysis was performed with Kinetic Studio

software from Hi-Tech Scientific, IGOR Pro 5.0 by Wavemetrics, Inc. The kinetics of O_2

binding to Pd(IPr)(P(p-tolyl)$_3$) were measured in THF by stopped flow kinetic methods at

very low temperature (-90 to -75 °C). The experiment was performed under

stoichiometric conditions, with a 1:1 molar ratio of Pd(IPr)(P(p-tolyl)$_3$) to dioxygen. The

O_2 solutions were prepared by bubbling a dilute O_2 gas mixture into THF (5% O_2 /95%

N_2) to saturation, and then further dilutions achieved a final concentration of 0.125 mM

after mixing (for saturated O_2 /THF solutions, [O_2] = 10mM). The rapid binding event

was monitored by the decay of the Pd(IPr)(P(p-tolyl)$_3$) peak at λ= 414 nm over 2.5 seconds (Figure 2.11) with Pd(IPr)(P(p-tolyl)$_3$) = 0.122 mM after mixing.

The decay curves (Figure 2.12) for each temperature fit to a second order function under conditions where [A] = [B], are shown in Eqn. (2.4).

$$A_t = A_f - \left(\frac{(A_f - A_o)}{1 + (k*[Pd]_o*t)} \right)$$

(2.4)
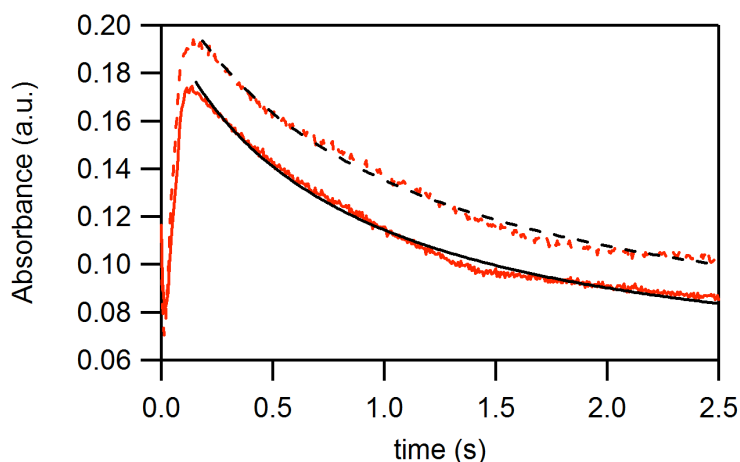
Figure 2.82 Decay curves (red) and second order fit curves (black) for -90 °C (dotted), and -85 °C (solid) with [Pd] = [O$_2$] = 0.12 M. Decay and growth under 0.2 s is due to mixing at low temperature and is not a feature of the reaction.

Second order rates were collected at each temperature and tabulated in Table 2.2. The temperature dependent rate constants measured in this work were extrapolated to 29 °C and yielded a rate, k = 146,000 M^{-1}s^{-1}.

Table 2.2 Rate constants measured for O$_2$ binding with Pd(IPr)(P(p-tolyl)$_3$). Stopped-flow kinetics measured under stoichiometric conditions, Pd(IPr)(P(p-tolyl)$_3$) = 0.122 mM and [O$_2$] = 0.125 mM. *Rate constant at 29 °C was extrapolated from low temperature measurements.

T (°C)	k$_2$ (M^{-1}s^{-1})
-90	8,240
-85	10,700

-80	12,000
-75	14,300
29	146,000*
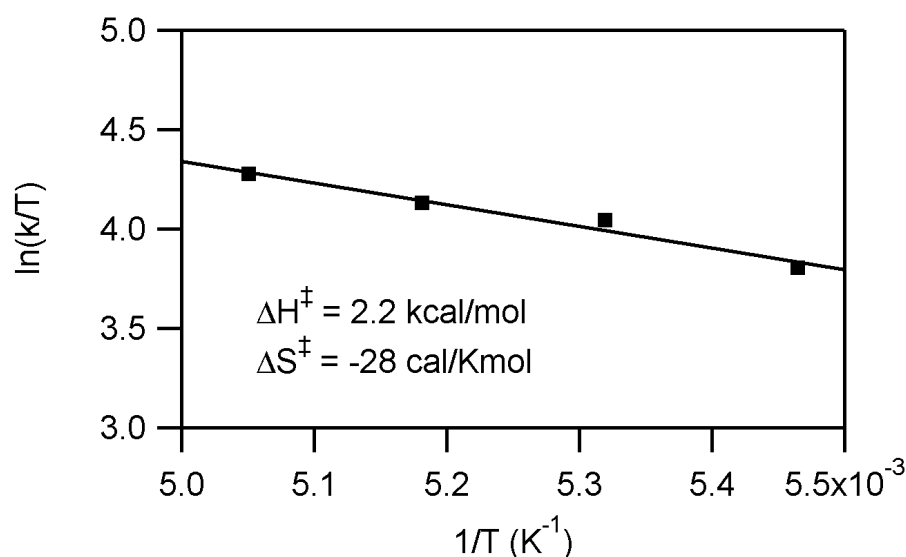
Figure 2.13 Eyring plot for O_2 binding with Pd(IPr)(P(p-tolyl)$_3$).

Activation parameters were obtained from the generated Eyring plot (Figure 2.13). The values obtained, $\Delta H^{\ddagger} = 2.2 \pm 0.3$ kcal/mol and $\Delta S^{\ddagger} = -28 \pm 2$ cal/mol•K, describe a small kinetic barrier and a binding step that is rate limiting. These data are combined with thermochemical data to generate a combined potential energy diagram shown in Scheme 2.2.

C. Computational Details and Coordinates for Ia, Ib, and Ic

Computational methods and models. All calculations were performed using the Gaussian 03 program.[52] The geometries of the structures were optimized in gas-phase without any symmetry constraints at the B3LYP/Lanl2dz level of theory using the Hay-Wadt effective core potential (ECP) for Pd.[53] The available X-ray structures of the

Pd(IPr)$_2$(η^1-O$_2$) (Ia), Pd(IMes)$_2$(η^1-O$_2$) (Ib) and Pd (IPr)(PPh$_3$)(η^1-O$_2$) (Ic) complexes were utilized as the starting points for these calculations.

D. Structural Data for Compounds *trans*-Pd(IPr)$_2$(η^1-O$_2$)$_2$ and *trans*-Pd(SIPr)$_2$(OOH)$_2$.

Crystallographic Analyses for Compound *trans*-Pd(IPr)$_2$(η^1-O$_2$)$_2$: Very small single crystals of *trans*-Pd(IPr)$_2$(η^1-O$_2$)$_2$ suitable for diffraction analysis were grown by slow evaporation of solvent from a hexane solution at room temperature in a dry box. X-ray diffraction studies were performed at 93K using a Rigaku MM007/Mercury/ diffractometer (confocal optics Mo-Kα radiation) Intensity data were collected using ω and φ steps accumulating area detector frames spanning a hemisphere of reciprocal space (data were integrated using CrystalClear[54]). All data were corrected for Lorentz, polarisation and long-term intensity fluctuations. Absorption effects were corrected on the basis of multiple equivalent reflections. The structure was solved by direct methods and refined by full-matrix least-squares against F^2 (SHELXTL[55]). All hydrogen atoms were assigned riding isotropic displacement parameters and constrained to idealized geometries. The *R* factor reflects the very small crystal size and the presence of half a hexane solvate molecule.

Crystallographic Analyses for Compound *trans*-Pd(SIPr)$_2$(OOH)$_2$. Single crystals of *trans*-Pd(SIPr)$_2$(OOH)$_2$ suitable for diffraction analysis were grown by slow evaporation of solvent from a heptane solution at room temperature in a dry box. The data crystal of compound *trans*-Pd(SIPr)$_2$(OOH)$_2$ was glued onto the end of a thin glass fiber. X-ray intensity data were measured by using a Bruker SMART APEX2 CCD-based diffractometer using Mo Kα radiation (λ = 0.71073 Å).[56] The raw data frames were integrated with the SAINT+ program by using a narrow-frame integration algorithm.[56]

Corrections for Lorentz and polarization effects were also applied with SAINT+. An empirical absorption correction based on the multiple measurement of equivalent reflections was applied using the program SADABS. All structures were solved by a combination of direct methods and difference Fourier syntheses, and refined by full-matrix least-squares on F^2, by using the SHELXTL software package.[57] Crystal data, data collection parameters, and results of the analyses are listed in Table 2.3.

Compound *trans*-Pd(SIPr)$_2$(OOH)$_2$ crystallized in the triclinic crystal system. The space group $P\bar{1}$ was assumed and confirmed by the successful solution and refinement of the structure. All non-hydrogen atoms were refined with anisotropic displacement parameters. Hydrogen atoms were placed in geometrically idealized positions and included as standard riding atoms during the least-squares refinements.

Table 2.3 Crystallographic Data for Compounds $Pd(IPr)_2(\eta^1\text{-}O_2)_2$ and $Pd(SIPr)_2(OOH)_2$.

	$Pd(IPr)_2(\eta^1\text{-}O_2)_2$	$Pd(SIPr)_2(OOH)_2$
Empirical formula	$PdO_4N_4\,C_{54}H_{72}\bullet\tfrac{1}{2}C_6H_{14}$	$PdO_4N_4\,C_{54}H_{78}$
Formula weight	990.64	953.60
Crystal system	Monoclinic	Triclinic
Lattice parameters		
a (Å)	13.766(4)	12.2884(5)
b (Å)	15.624(4)	12.3340(5)
c (Å)	25.915(8)	17.2479(7)
α (deg)	90	82.982(1)
β (deg)	103.647(7)	87.966(1)
γ (deg)	90	89.015(1)
V (Å^3)	5416(3)	2592.74(18)
Space group	$P\,2_1/c$ (# 14)	$P\,\bar{1}$ (#2)
Z value	4	2
ρ_{calc} (g / cm^3)	1.215	1.221
μ (Mo Kα) (mm^{-1})	0.389	0.404
Temperature (K)	93	296
$2\Theta_{max}$ (°)	50.00	57.00
No. Obs. ($I > 2\sigma(I)$)	6664	10468
No. Parameters	595	586
Goodness of fit	1.138	1.021
Max. shift in cycle	0.013	0.001
Residuals*:R1; wR2	0.1261; 0.2906	0.0375; 0.0848
Absorption Correction, Max/min	Multi-scan 1.0000/0.9488	Multi-scan 0.7465/0.6552
Largest peak in Final Diff. Map (e$^-$ / Å^3)	3.271	0.597

$*R = \Sigma_{hkl}(\,|\,|F_{obs}|-|F_{calc}|\,|\,)/\Sigma_{hkl}|F_{obs}|$; $R_w = [\Sigma_{hkl}w(\,|F_{obs}|-|F_{calc}|\,)^2/\Sigma_{hkl}wF_{obs}^2]^{1/2}$, $w = 1/\sigma^2(F_{obs})$; $GOF = [\Sigma_{hkl}w(\,|F_{obs}|-|F_{calc}|\,)^2/(n_{data}-n_{vari})]^{1/2}$.

Chapter 3: A Tale of Two Dioxygen Adducts: Pd(IPr)$_2$(η^1-O$_2$)$_2$ and Pd(IMes)$_2$(η^2-O$_2$) - Comparison of η^1-O$_2$ and η^2-O$_2$ in Reactivity

It is the end-on O$_2$. It is the side-on O$_2$. It is reactive to substrates. It is inert to substrates. It is the primary product of O$_2$ binding. It is the secondary product of O$_2$ binding. It is the unstable intermediate. It is the stable final product.

The statement above is a variation on the introduction to Dicken's "A Tale of Two Cities". In this section we compare and provide evidence for an equilibrium between the η^1 and η^2-O$_2$ binding forms. No direct detection of the equilibrium is available, but two key experiments provide a sound basis for making this claim. The tale of the two dioxygen adducts is the detailed mechanism of O$_2$ binding for Pd(IPr)$_2$ in comparison to Pd(IMes)$_2$ and the difference in reactivity with water. In spite of the indirect nature of this evidence, it points the way towards future studies aimed at direct comparison, including additional stopped-flow kinetic as well as ^{18}O$_2$ experiments.

3.1   Background

The Schindler group[20] in Germany synthesized and characterized the first 1:1 end-on Cu-O$_2$ adduct [Cu(TMG$_3$tren)O$_2$]SbF$_6$ (TMG = tris(tetramethylguanidino) at temperature of -55 °C by using sterically hindered ligands. Remarkably, the formation of Cu-O$_2$ adduct is reversible: warming up of the adduct complex solution to room temperature caused the loss of O$_2$ from the superoxo Cu(III) complex, while cooling the same solution down to low temperature led to the reformation of the superoxo complex. No observable decomposition was found after this transformation cycle was repeated many times. This end-on Cu-O$_2$ adduct [Cu(TMG$_3$tren)O$_2$]SbF$_6$ is viewed as the first

product formed in the general mechanistic framework of molecular oxygen binding to copper complexes as described in Scheme 3.1.

$$LCu^I + O_2 \rightleftharpoons LCuO_2$$

$$\Big\Updownarrow + LCu^I$$

$$LCu-O{\diagdown}_{O-CuL} \quad \text{or}$$

$$LCu{<}^{O}_{O}{>}CuL \quad \text{and/or} \quad LCu{<}^{O}_{O}{>}CuL$$
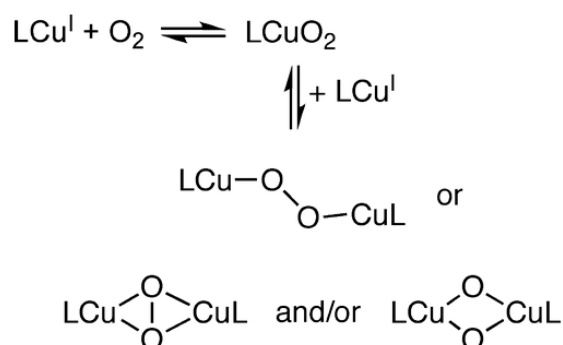
Scheme 3.1 General scheme of O_2 binding to copper complexes.

It is generally believed that the η^1-O_2 motif is more reactive than the η^2-O_2 motif for its intrinsic radical property.[13] The η^1-O_2 activated by transition metals may also be more accessible to substrates than its η^2-O_2 counterpart due to its hanging structure and longer distance from the metal center.
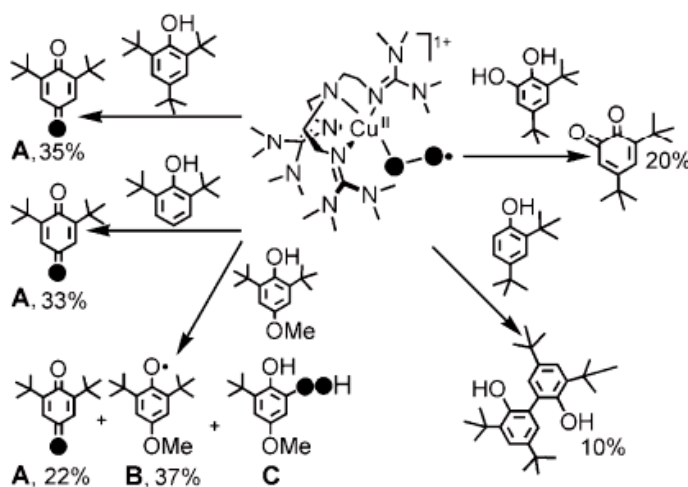
Scheme 3.2 Reactivity of [Cu(TMG$_3$tren)O$_2$]SbF$_6$ with exogenous phenolic substrates. (Dark circles represent ^{18}O) (Drawing taken from ref 58)

Following the work of Schindler, Karlin and coworkers[58] found that [Cu(TMG$_3$tren)(η^1-O_2)]SbF$_6$ readily oxidizes exogenous phenolic substrates as shown in Scheme 3.2. Furthermore, it can also undergo intramolecular oxidations forming a

hydroxylated product. In contrast, $Cu(\eta^2\text{-}O_2)$ complexes supported by β-diketiminate and anilide-imine ligands show rather inert reactivity with phenols and phosphines, and instead lose O_2 and form Cu-phosphine adducts.[59] The differences in reactivity between the η^1 and η^2-bound forms of O_2 is a "frontier" area in inorganic and bioinorganic chemistry.

Since this is a new area of research for the Hoff group it has presented a learning experience with numerous failed experiments occurring prior to successful ones. For example, the reaction with water described later in this chapter was discovered during attempted reactions with carbon dioxide--it later turned out that it was incidental exposure and trapping of water at low temperatures that led to formation of a novel hydroxyl, hydroperoxy complex. In addition, the reversible nature of initial O_2 binding arose out of stopped-flow kinetic studies done at -70 to -90 ^{o}C where an initial colorless product was discovered. NMR studies done at Miami, also at low T, confirmed that the first product of O_2 addition at low T was a diamagnetic complex and not the paramagnetic $(\eta^1\text{-}O_2)_2Pd(IPr)_2$.

3.2   Results and Discussion

Two-stage O_2 Binding to Pd(IPr)$_2$. Following the synthetic and structural work described in Chapter 2, we further investigated the kinetics of O_2 binding to Pd(IPr)$_2$. At the time these studies were begun, we believed that the sole product of reaction with O_2 was the paramagnetic $Pd(IPr)_2(\eta^1\text{-}O_2)_2$ and spectroscopic changes such as those shown in Figure 2.2 (at room temperature) were expected to occur over the entire temperature range of binding. To our great surprise, at very low temperatures in the range of -90 ^{o}C to -70 ^{o}C a nearly complete bleaching of color, similar to what occurs when O_2 binds to

Pd(IMes)$_2$ to form Pd(IMes)$_2$(η^2-O$_2$) were discovered. Furthermore, this rate of binding was fast--comparable in speed to that of Pd(IPr)(P-p-tolyl)$_3$.[46] Results from stopped-flow kinetic studies in the reaction of O$_2$ binding to Pd(IPr)$_2$ show that the reaction between Pd(IPr)$_2$ and excess O$_2$ is rapid even at temperatures as low as -90 $^{\circ}$C and the first mole of O$_2$ binds in the temperature range -90 to -70 $^{\circ}$C following a first-order rate law with $\Delta H^{\ddagger}$ = 6.0 kcal/mol and $\Delta S^{\ddagger}$ = -6 cal/mol•K. The UV-Vis spectrum of this intermediate shows an intensity decay at all wavelengths and indicates this intermediate is white or pale yellow in color. At higher temperatures, near -60 $^{\circ}$C, the second mole of O$_2$ adds and the yellow-orange complex $trans$-Pd(IPr)$_2$(η^1-O$_2$)$_2$ is formed from the white or pale yellow Pd(IPr)$_2$($\eta^?$-O$_2$). The spectroscopic changes shown in O$_2$ binding to Pd(IPr)$_2$ forming $trans$-Pd(IPr)$_2$(η^1-O$_2$)$_2$ is a two-stage process characterized by stopped-flow and low-temperature NMR.

Based on these results low-T NMR is performed on adding O$_2$ to Pd(IPr)$_2$ at a series of temperatures as low as -70 $^{\circ}$C (Figure 3.1). The diamagnetic characteristics of the peaks and the pale-yellow color of the low-T O$_2$ adduct indicate that the first binding adduct may be the square planar palladium peroxide complex, Pd(IPr)$_2$(η^2-O$_2$). Upon elevating the temperature the diamagnetic features of the peaks slowly disappear and the emergence of the paramagnetic peaks indicate the formation of Pd(IPr)$_2$(η^1-O$_2$)$_2$. No spectroscopic evidence for Pd(IPr)$_2$(η^1-O$_2$) could be found-it would be expected to be a paramagnetic superoxide complex. Attempts to grow single crystals for the interesting intermediate Pd(IPr)$_2$(η^2-O$_2$) at low temperature have so far been unsuccessful.
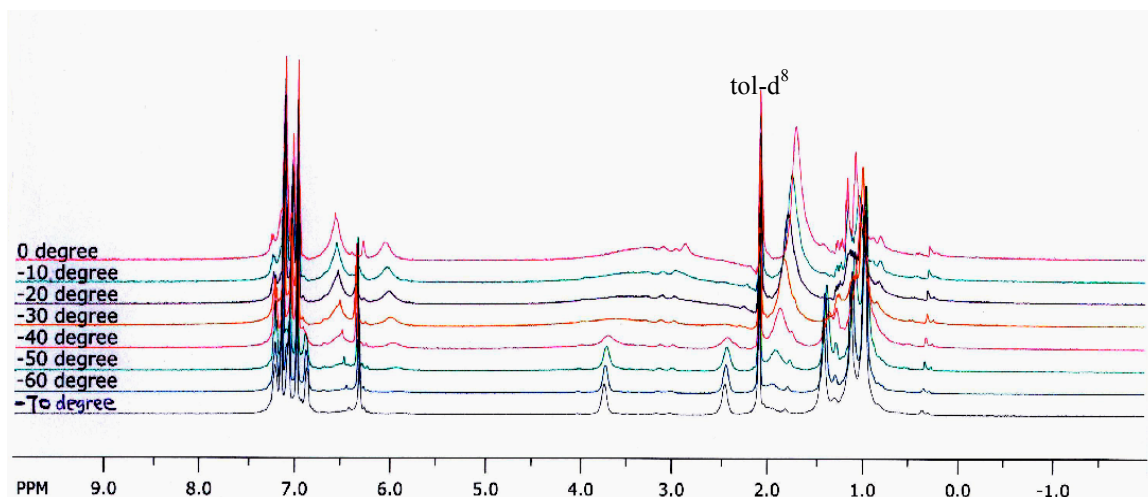
Figure 3.1 Low-T NMR spectra of adding O_2 to tol-d^8 solution of Pd(IPr)$_2$ at variable temperatures.

Reversibility of O_2 Binding. An additional interesting aspect of the complex Pd(IPr)$_2$(η^2-O_2) is its reversible nature of O_2 binding. Even at low temperatures, evacuation of O_2 causes regeneration of the starting Pd(IPr)$_2$ complex. This cycle can be performed several times without sample decomposition at low temperature. This is in contrast to all other Pd complexes we have studied--for example Pd(IMes)$_2$(η^2-O_2).[18] Once formed it exhibits irreversible binding and even prolonged evacuation above room temperature fails to regenerate Pd(IMes)$_2$.

The conclusion from these studies is that O_2 binds very rapidly at low T to form a diamagnetic complex with a very weakly bound O_2 which can be removed by evacuation even at - 70 ^{o}C. The complex gradually loses O_2 and converts back cleanly to quantitative Pd(IPr)$_2$ in the process of warming up to room temperature under vacuum without any spectroscopic degradation. This vacuum/O_2 cycle can be repeated many times and no decomposition was observed. However if Pd(IPr)$_2$(η^2-O_2) is warmed up under O_2 atmosphere, a second mole of O_2 will add and form the unique final product Pd(IPr)$_2$(η^1-O_2)$_2$. Once this forms, applying vacuum does not regenerate the deoxygenated Pd(IPr)$_2$ or

any other complex. This reversible O_2 binding provides evidence that the $Pd(\eta^1\text{-}O_2)$ adduct may be accessible. It is the logical first step in loss of O_2, as well as in binding of O_2. From the principle of microscopic reversibility the same transition occurs. Numerous calculations, as well as chemical intuition, are in agreement with an initial attachment of O_2 to a sterically demanding environment would be through one and not both of the O atoms. This is illustrated in the earlier picture Figure 2.7. Since there is no spectroscopic evidence of significant buildup of the $Pd(\eta^1\text{-}O_2)$ adduct, it can not be concluded that an equilibrium amount of this proposed complex is formed. However, its presence as a steady state intermediate in the facile on/off binding of O_2 at low T is reasonable.

These observations can be compared to the conclusions of Stahl and coworkers who calculated that O_2 binding to $Pd(IMe)_2$ with truncated ligands "IMe" has $\Delta G^0 = +3.6$ kcal/mol in gas phase and $\Delta G^0 = -5.7$ kcal/mol in toluene.[22] The ΔG^0 is low--actually similar to that of the Vaska's complex ($\Delta G^0 = -5.9$ kcal/mol) which is known to bind O_2 reversibly. This serves to point out the difficulty in calculation of binding energetics to heavy metal complexes. In spite of the low calculated free energy of binding, Stahl determined that dissociation of O_2 from $Pd(IMes)_2O_2$ experimentally was unsuccessful. This complex forms rapidly even at -78 °C after the introduction of O_2. Sparging the toluene solution of $Pd(IMes)_2O_2$ with inert gas and evaporating all the solvent cannot regenerate the deoxygenated material, and heating up a solid sample of $Pd(IMes)_2O_2$ to a high temperature for one week only resulted a small percentage of conversion.[22] A proposed scheme for binding of O_2 to $Pd(IPr)_2$ is shown in Scheme 3.3 below.
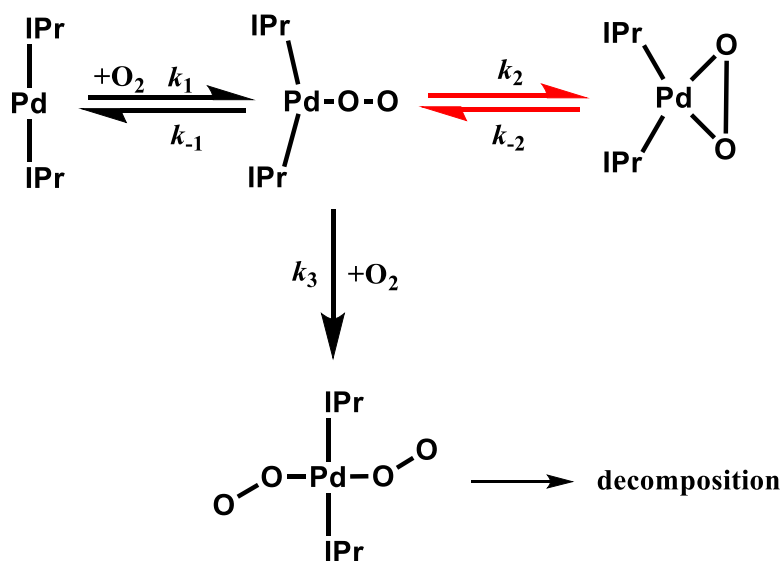
Scheme 3.3 General Scheme of O_2 binding to Pd(IPr)$_2$.

This scheme involves initial reversible formation of an end-on η^1 adduct in the k_1/k_{-1} step. This key intermediate $(\eta^1\text{-}O_2)$Pd(IPr)$_2$ is at a branching point in the mechanism--it could conceivably convert to $(\eta^2\text{-}O_2)$Pd(IPr)$_2$ in the k_2/k_{-2} step, or add a second mole of O_2 in the k_3 step. The mechanism proposed for binding to Pd(IMes)$_2$ corresponds to only the top line of Scheme 3.3 and is shown in Scheme 3.4 below:
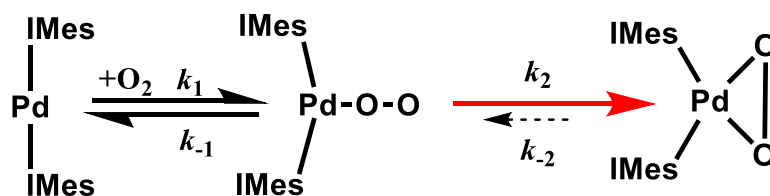
Scheme 3.4 General Scheme of O_2 binding to Pd(IMes)$_2$.

The difference between these two schemes ultimately lies in the magnitudes of the relative rate constants. The observed reactivity of Pd(IMes)$_2$ implies that the Scheme 3.3 for Pd(IPr)$_2$ has been altered--either a much larger value exists for k_2 driving the initial adduct swiftly to product, or k_{-2} is much smaller for Pd(IMes)$_2$ and reverting back to the Pd(η^1-O_2) adduct is thermodynamically disfavored for the IMes complex but not for the

IPr complex. The final possibility, that the k_3 step which is present in Scheme 3.3 is not available to Pd(IMes)$_2$ is unreasonable since, if anything, it would be expected to be both faster and more favorable for the smaller IMes system. The most likely conclusion based on these observations is that the Pd(η^2-O$_2$) adduct for the IPr system is destabilized and the Pd(η^1-O$_2$) adduct is closer in energy to it than is the case for the IMes system. This implies a possible equilibrium buildup of the Pd(η^1-O$_2$) adduct, and a probable kinetic accessibility to it. That accessibility might lead to different reactivity patterns, and our initial probing of that question is described in the next section.

Reaction of H$_2$O with Pd(IPr)$_2$(η^2-O$_2$) and Pd(IMes)$_2$(η^2-O$_2$). This reaction was discovered accidentally. Initially, we investigated the reaction of Pd(IPr)$_2$ with oxygen followed by reaction with carbon dioxide. It was hoped that we would produce a peroxycarbonate complex as is known to occur with related complexes[40c] as shown in Scheme 3.5.
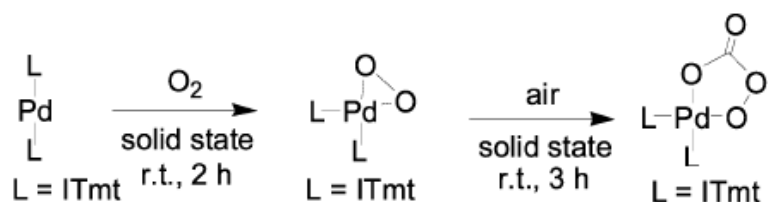
Scheme 3.5 Reaction of Pd(ITmt)$_2$ with O$_2$ and CO$_2$. (ITmt = 1,3-bis(2,2'',6,6''-tetramethyl-*m*-terphenyl-5'-yl)imidazol-2-ylidene)

This reaction was investigated several times under different conditions and was found to be difficult to reproduce. In spite of that a solid complex was formed, isolated, and a preliminary crystal structure determined by Professor Captain. Surprisingly this structure, as well as the NMR spectra indicated that the complex did not involve carbon dioxide binding at all, but rather was of the form: Pd(IPr)$_2$(OH)(OOH). In addition, full

analytical results (C, H, N, Pd, O) was in keeping with this formulation. At that time

direct reaction with water was attempted--the reaction must be done at low T because

only at low T is Pd(IPr)$_2$(η^2-O$_2$) stable. Due to the freezing point of water, use of toluene

as a solvent did not give good yields of products since the water froze out of solution. It

was found that reaction in CH$_3$OH/H$_2$O mixtures in ether or toluene gave good yields of

Pd(IPr)$_2$(OH)(OOH). The complex Pd(IPr)$_2$(η^2-O$_2$) synthesized at -78 $^{\circ}$C converted

cleanly to *trans*-Pd(IPr)$_2$(OOH)(OH) (Figure 3.2) in 4 hours at -78 $^{\circ}$C.

Under these conditions, and depending upon the CH$_3$OH/H$_2$O ratio small amounts

of a second complex could be detected by NMR. This is proposed to be *trans*-

Pd(IPr)$_2$(OMe)(OOH). Under identical conditions, reaction of Pd(IMes)$_2$ was found to

not occur--the complex Pd(IMes)$_2$(η^2-O$_2$) was unchanged even for three days at room

temperature. The reactions with H$_2$O and CH$_3$OH are proposed to proceed as shown in

eqns. (3.1) and (3.2).

Pd(IPr)$_2$(η^2-O$_2$) $\rightleftharpoons$ Pd(IPr)$_2$(η^1-O$_2$) + H$_2$O $\longrightarrow$ *trans*-Pd(IPr)$_2$(OOH)(OH)   (3.1)

Pd(IPr)$_2$(η^2-O$_2$) $\rightleftharpoons$ Pd(IPr)$_2$(η^1-O$_2$) + CH$_3$OH $\longrightarrow$ *trans*-Pd(IPr)$_2$(OMe)(OOH)   (3.2)
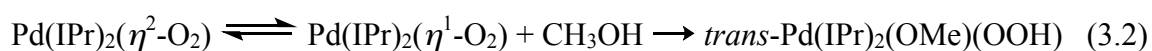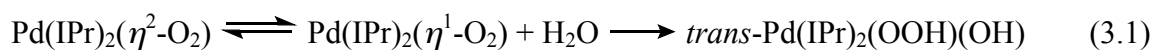
The crystal structure of *trans*-Pd(IPr)$_2$(OOH)(OH) is shown in Figure 3.2. It is

viewed as a near perfect square planar Pd(II) complex with two near 180° angles (O2 –

Pd1 – O1 = 177.64(13)$^{\circ}$ and C1 – Pd1 – C31 = 179.30(13)$^{\circ}$) and two equal lengths Pd-O

bonds (Pd1 – O1 = 2.009(3) Å and Pd1 – O2 = 2.009(3) Å).
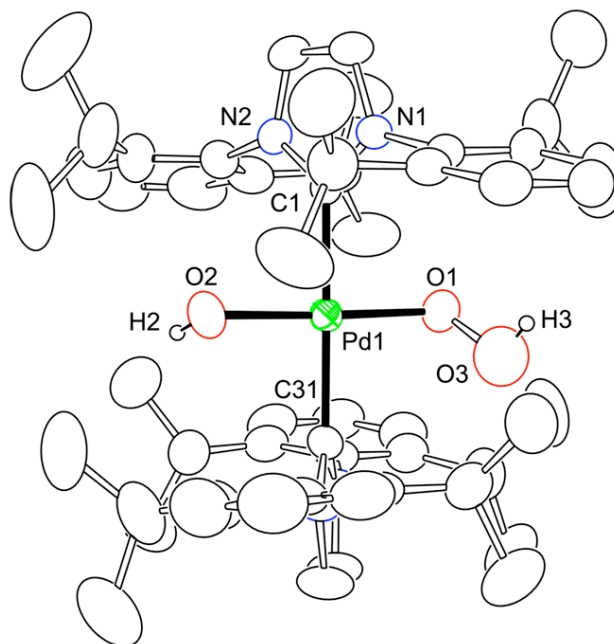
Figure 3.2 ORTEP diagram of Pd(IPr)$_2$(OOH)(OH). Pd1 – O1 = 2.009(3) Å, Pd1 – O2 = 2.009(3) Å, O1 – O3 = 1.465(6) Å, Pd1 – C1 = 2.051(3) Å, Pd1 – C31 = 2.050(3) Å; O2 – Pd1 – O1 = 177.64(13)°, C1 – Pd1 – C31 = 179.30(13)°, Pd1 – O1 – O3 = 111.1(3)°.

This kind of Pd(II)-OOH complexes is considered as important intermediate in selective oxidation reactions. The author is unaware of any other report in which reaction of O$_2$ and H$_2$O lead directly to a complex of this type. So far, attempts to use this complex in catalytic or stoichiometric oxidations have not been successful. As discussed later, that is presumably due to the absence of an accessible vacant coordination site at the Pd center. Pd(IMes)$_2$(η^2-O$_2$) is known to be able to do rapid acetic acid addition at room temperature (Eqn. (3.3)).

(3.3)
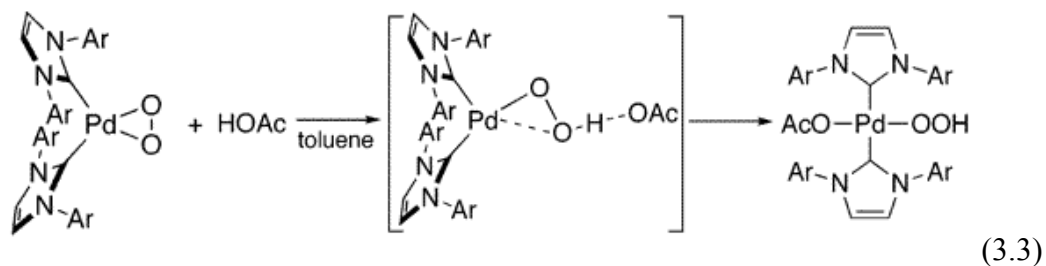
The attack of the peroxo O_2 ring by hydrogen on the acetic acid to force it to open and be protonated may depend considerably on the acidity of the electrophile. Compared to acetic acid (pKa = 4.76 in H_2O, pKa = 12.3 in DMSO), H_2O (pKa = 15.7 in H_2O, pKa = 32 in DMSO) is a much weaker acid and therefore may not be able to "crack" the Pd-O-O ring to open up and do protonation. However in the case of Pd(IPr)$_2$, while the Pd-O_2 complex mainly exist as Pd(IPr)$_2(\eta^2$-$O_2)$, Pd(IPr)$_2(\eta^1$-$O_2)$ may be kinetically accessible, which is able to be protonated by H_2O and may go through a radical pathway (Scheme 3.5).
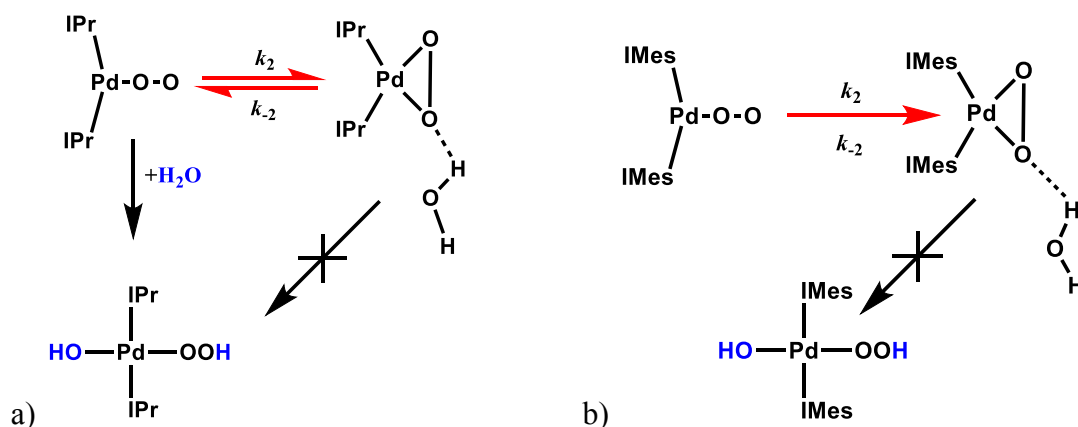
Scheme 3.6 Reaction of H_2O with a) Pd(IPr) (η^2-O_2) and b) Pd(IMes)$_2$, respectively.

3.3 Conclusions

Molecular O_2 binding to Pd(IPr)$_2$ is a two-stage process as characterized by stopped-flow and low-temperature NMR. The first mole of O_2 binds to Pd(0) forming Pd(IPr)$_2(\eta^2$-$O_2)$ at temperatures lower than -70 $^\circ$C with $\Delta H^{\ddagger}$ = 6.0 kcal/mol and $\Delta S^{\ddagger}$ = - 6 cal/mol•K. The second mole of O_2 binds at higher temperature forming the final product Pd(IPr)$_2(\eta^1$-$O_2)_2$. An equilibrium is proposed to exist between the η^1-O_2 form and η^2-O_2 form in the Pd(IPr)$_2$ system. It is not favorable enough to allow detection of η^1-O_2 form but does serve to allow it to be more accessible to reactivity that is indicated for the very

similar Pd(IMes)$_2$ system. This unique property of Pd-O-O ring opening up to end-bound Pd-O$_2$ enables the spliting of H$_2$O forming Pd(IPr)$_2$(OOH)(OH) and reversible O$_2$ binding at low temperature.
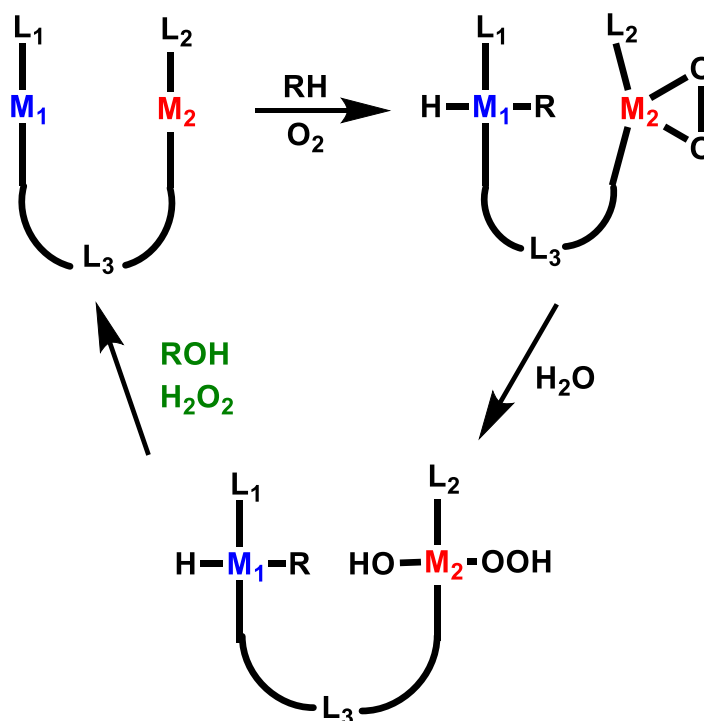
Scheme 3.7 Designed catalytic system for selective oxidation by using O$_2$ and H$_2$O as oxidants. L$_1$ and L$_2$ are modified to tune the binding properties of M$_1$ and M$_2$. L$_3$ is a bindentate ligand.

The fact that small changes in the ligand system can result in these observed changes in reactivity provides hope for catalyst design. Since the Pd system that binds and activates O$_2$ will likely not be the site that activates the substrate, this will require a two site catalyst as illustrated in Scheme 3.6--one for binding of O$_2$ and rection with H$_2$O and a second proximate site to bind a substrate for oxidation.

3.4   Experimental

A. Synthetic Experiments.

General Methods. Unless stated otherwise all reactions were carried out inside an MBraun or Vacuum Atmospheres glovebox or utilizing Schlenk tube techniques under inert atmosphere conditions. Solvents were purified by distillation under argon from an appropriate drying agent into flame dried glassware. NMR spectra were recorded on either a Bruker 400 MHz or a Bruker 300 MHz NMR spectrometer. Calorimetric measurements were performed using a Setaram Calvet C-80 or modified Guild Solution Calorimeter as described previously. Elemental analyses were performed at London Metropolitan University. Pd-NHCcomplexes and their O_2 derivatives were prepared by methods strictly analogous to those reported previously. Representative procedures for preparation and reactions of new complexes are described below.

Low-Temperature NMR study on O_2 binding to Pd(IPr)$_2$. In an NMR tube 8 mg Pd(IPr)$_2$ was dissolved in 1 mL of tol-d^8 inside the glovebox. Then the tube was brought out of the glovebox and put into a Bruker 400 MHz NMR spectrometer, which was tuned to -70 ºC and equilibrated for 10min. When the temperature of the solution in the NMR tube was at -70 ºC and steady for 10min, a spectrum was taken for the stock solution. Then pure excess O_2 was introduced by a tight syringe and the tube was shaken to make sure of good mixing. The tube was then put back into the NMR machine and waited until its temperature reached -70 ºC and steady for 10min. A series of NMR spectrum were run at the temperature range of -70 ºC to 20 ºC.

Reversible O_2 Binding to Pd(IPr)$_2$ at Low Temperature. 5ml Pd(IPr)$_2$ toluene solution of 0.0045M (20mg Pd(IPr)$_2$) was made and filled in a Schlenk tube in the glovebox. The

tube was brought out of the glovebox and cooled down to -78 ºC in a dry ice/acetone bath until the temperature was stable, followed by introduction of excess O_2. The tube was shaken with the solution part emerged in the bath all the time to keep it at -78 ºC. The color of Pd(IPr)$_2$ solution faded from fluorescent yellow-orange color to light yellow in less than 2min. Then vacuum was applied to the tube and it was taken out of the bath. The tube was shaken and kept under vacuum while warming up. The light yellow color turned back to yellow orange in less than 2min. This whole O_2 addition/vacuum procedure was repeated 10 times. In the end the Pd(IPr)$_2$ solution was dried up under vacuum and an NMR spectrum was taken for its C_6D_6 solution.

Synthesis of Pd(IPr)$_2$(OOH)(OH). 60 mg of Pd(IPr)$_2$ was dissolved in 8ml Et_2O and the solution was filled into a Schlenk tube inside the glovebox. The tube was then brought out of the glovebox and cooled down to -78 ºC in a dry ice/acetone bath until the temperature was stable, followed by introduction of excess O_2. The color of Pd(IPr)$_2$ solution faded from fluorescent yellow-orange color to light yellow in less than 2min. Then vacuum was carefully applied to the tube at -78 ºC without shaking in order not form any Pd(IPr)$_2$. A 4.5ml mixture of MeOH/H_2O containing 4ml MeOH and 0.5ml H_2O was premade. Under Argon gas flow, 4 drops of this MeOH/H_2O mixture was added to the solution under -78 ºC. Off-white precipitates were observed immediately floating in the solution. The reaction mixture was kept under Ar at -78 ºC for 4h before it turned yellow/orange. The liquid part of the mixture was evacuated off and the remaining yellow-orange solid was dried under vacuum for 1h. The yield of the synthesis of Pd(IPr)$_2$(OOH)(OH) is 73.8%. Peaks assigned to Pd(IPr)$_2$(OOH)(OH): ^{1}H NMR (300MHz, tol d^8): δ = 7.28 (t, 4H, *p*-Ar), 7.13 (d, 8H, *o*-Ar), 6.36 (s, 4H, backbone of IPr),

3.77 (s, 1H, OOH), 2.97 (hep, 8H, CH on ^{i}Pr), 1.12 (d, 24H, ^{t}Bu on ^{i}Pr), 0.98 (d, 24H, ^{t}Bu on ^{i}Pr), -4.71 (s, 1H, OH).

SpinWorks 3: Pd(IPr)2(OOH)(OH) in tol d8

file: ...12 Pd(IPr)2+O2+CO2 in tol d8\1\fid expt: <zg30>
transmitter freq.: 300.131501 MHz
time domain size: 83930 points
width: 11990.41 Hz = 39.9505 ppm = 0.142862 Hz/pt
number of scans: 32

freq. of 0 ppm: 300.130010 MHz
processed size: 16384 complex points
LB: 0.300   GF: 0.0000
Hz/cm: 168.238   ppm/cm: 0.56055
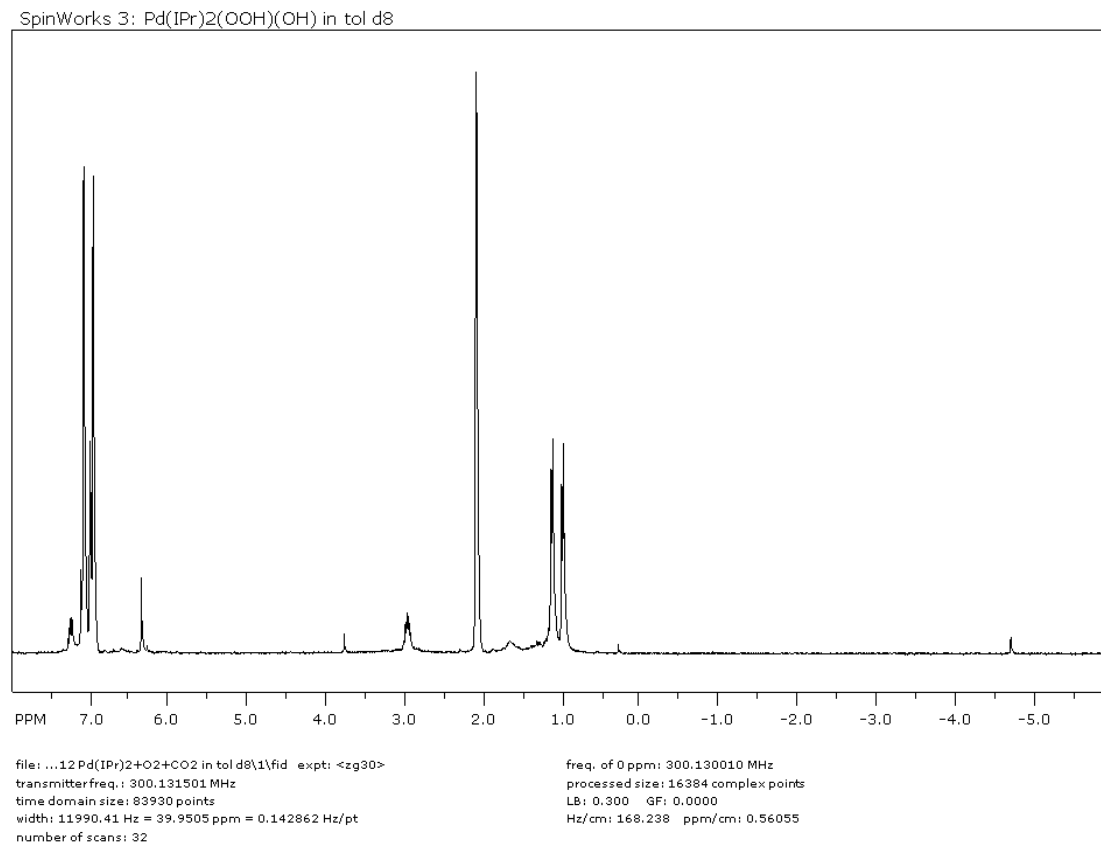
Figure 3.3 ^{1}H NMR spectrum in tol-d^8 of Pd(IPr)$_2$(OOH)(OH)

Synthesis of Pd(IPr)$_2$(OOD)(OD). In an NMR tube, 5 mg Pd(IPr)$_2$(OOH)(OH) was dissolved in 1ml tol-d^8. An NMR spectrum was taken at room temperature of this solution. Peaks at 3.77 ppm and 2.97 ppm show the presence of hydroxide and hydroperoxide groups. 1 drop of D$_2$O was added to the same NMR tube by pipette and NMR spectrum was taken again. The disappearance of these two peaks shows the replacement of H by D.

Controlled Experiments of H$_2$O with Pd(IPr)$_2$(η^2-O$_2$) and Pd(IMes)$_2$(η^2-O$_2$).

7 mg Pd(IPr)$_2$ was dissolved in 3ml toluene and the solution was filled into a 25ml Schlenk tube. Then the procedure described above in synthesis of Pd(IPr)$_2$(OOH)(OH) was followed. An NMR spectrum was run for the final product and confirmed it was Pd(IPr)$_2$(OOH)(OH).

7.3 mg Pd(IMes)$_2$(η^2-O$_2$) was dissolved in 3ml toluene and exactly the same procedure was followed. An NMR spectrum was run for solid left after vacuum and drying. The starting material Pd(IMes)$_2$(η^2-O$_2$) was retrieved and there was no evidence that any other products were made.

B. Stopped-Flow Kinetics

Toluene solutions of complex Pd(IPr)$_2$ were prepared in an MBraun glovebox filled with ultra high purity argon (Airgas) and loaded in Hamilton gastight syringes equipped with three way valves. Saturated solutions of ultra high purity O$_2$ (ultra dry grade, Airgas) were prepared by bubbling gas into gastight syringes containing dry toluene for at least 20 minutes; dilutions of the O$_2$ saturated solvent were performed anaerobically to obtain the desired [O$_2$]. The solubility of O$_2$ in toluene was taken as 8.3 mM at 20 °C. Time resolved spectra (λ = 400–800 nm) were acquired over a range of temperatures (-80 to -70 °C) using a Hi-Tech Scientific KinetAsyst SF-61DX2 CryoStopped-Flow system (TgK Scientific Ltd.) equipped with a quartz tungsten halogen light source, a J&M TIDAS diode array detector and a Brandenburg 4479 Series PMT monochromator. The instrument was equipped with stainless steel plumbing lined with PEEK tubing and a 1.00 cm^3 quartz mixing cell submerged in an ethanol cooling bath. The temperature in the mixing cell was maintained to ± 0.1 °C. Data acquisition was

performed using TIDAS-DAQ and/or Kinetic Studio software programs and mixing times were 2–3 ms. All flow lines were washed extensively with Ar-saturated dry toluene prior to loading reactant solutions. All experiments were performed in a single-mixing mode of the instrument with a 1:1 (v/v) mixing ratio. Reactions were studied under pseudo-first order conditions using excess O_2. Data analysis was performed using Kinetic Studio and IGOR Pro 5.0 (Wavemetrics, Inc.) software programs. Decay over the entire spectrum is observed for this rapid binding event. Single wavelength measurements were taken at $\lambda = 474$ nm in an effort to quantify kinetic parameters. Reasonable data was acquired at four different temperatures thus far (-85, -80, -75, -70°C) using 30 to 80 fold excess of dioxygen. The kinetic traces were fit to either a single exponential (traces at T = -80°C and higher) or double exponential equation (traces at T = -85°C) which gave the value of the pseudo first order rate constant (k_{obs}). All k_{obs} values reported represent an average from at least three runs.
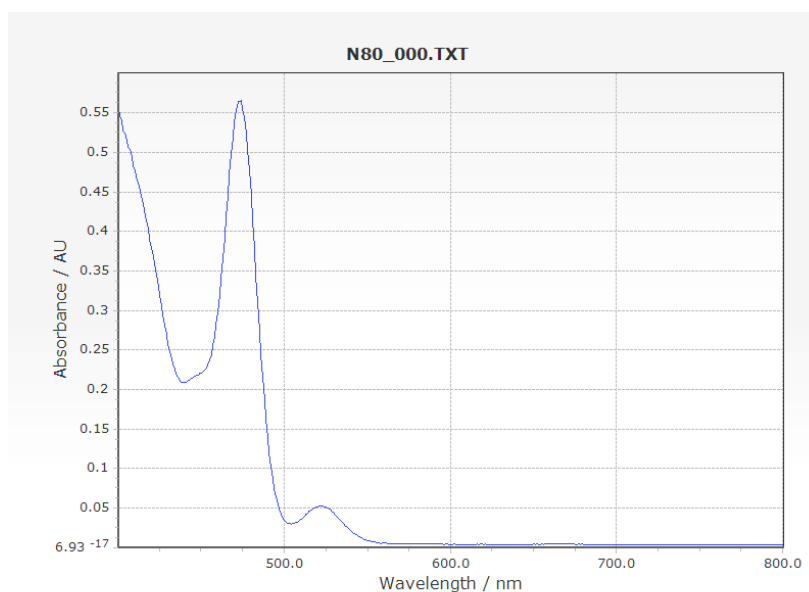
Figure 3.4 Diode array spectrum of Pd(IPr)$_2$ (0.2 mM unmixed).
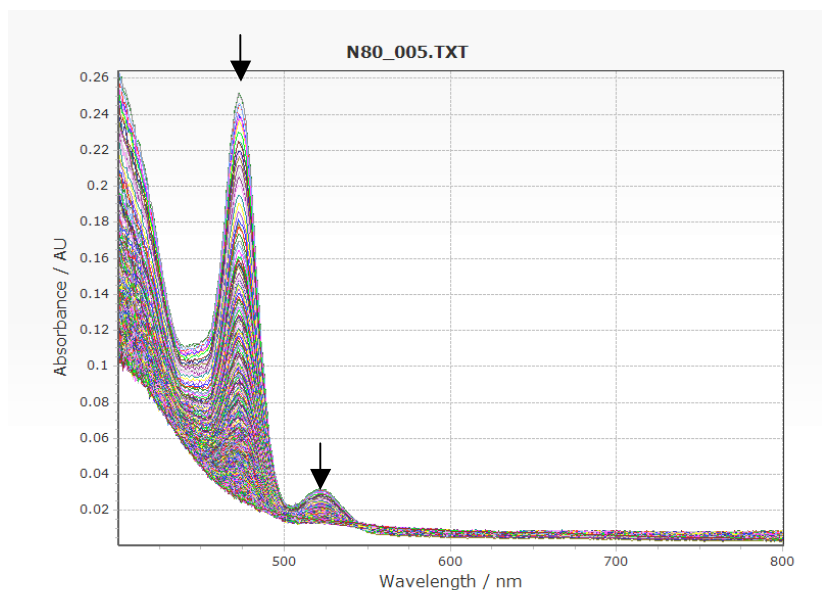
Figure 3.5 Diode array spectra of the reaction between Pd(IPr)$_2$ (0.1 mM) and excess O$_2$ (4.1 mM) over 3 seconds at -80°C (concentrations after mixing). The rapid binding of dioxygen leads to decay at all wavelengths.

Table 3.1 Temperature dependent pseudo first order rates and second order rate constants for Pd(IPr)$_2$ decay at λ = 474 nm with 0.05 mM Pd(IPr)$_2$.

-80°C			-75°C			-70°C		
[O$_2$] M	k_{obs} (s^{-1})	k (M$^{-1}\cdot$s^{-1})	[O$_2$] M	k_{obs} (s^{-1})	k (M$^{-1}\cdot$s^{-1})	[O$_2$] M	k_{obs} (s^{-1})	k (M$^{-1}\cdot$s^{-1})
1.7 × 10^{-3}	116	31,112	1.7 × 10^{-3}	160	48,089	1.7 × 10^{-3}	197	66,801
2.5 × 10^{-3}	145		2.5 × 10^{-3}	196		2.5 × 10^{-3}	255	
3.3 × 10^{-3}	176		3.3 × 10^{-3}	241		3.3 × 10^{-3}	315	
4.1 × 10^{-3}	192		4.1 × 10^{-3}	278		4.1 × 10^{-3}	361	

-85°C		
[O$_2$] M	k_{obs} (s^{-1})	k (M$^{-1}\cdot$s^{-1})
1.7 × 10^{-3}	47.2	18,570
2.5 × 10^{-3}	63.7	
3.3 × 10^{-3}	74.8	
4.1 × 10^{-3}	94.9	
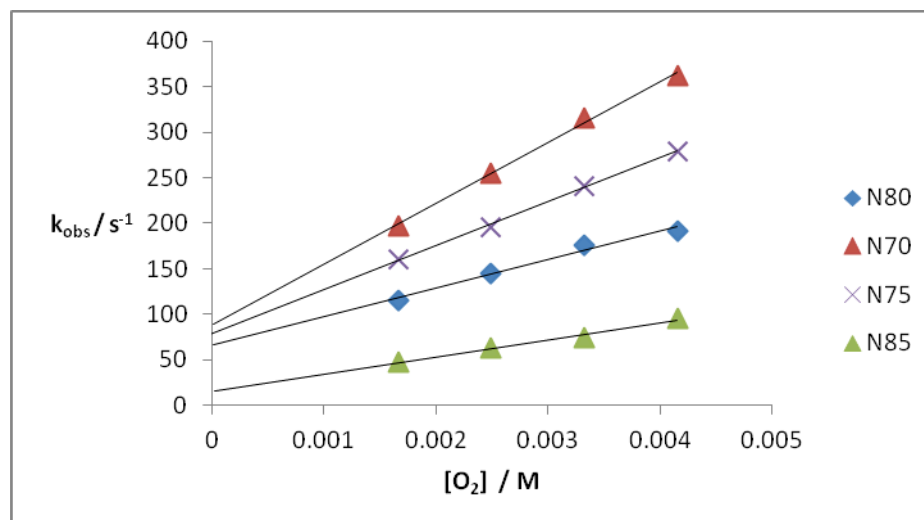
Figure 3.6 Bimolecular rate plot for reaction of Pd(IPr)$_2$ with excess O$_2$ at various temperatures. The bimolecular rate constants were obtained from the slopes.
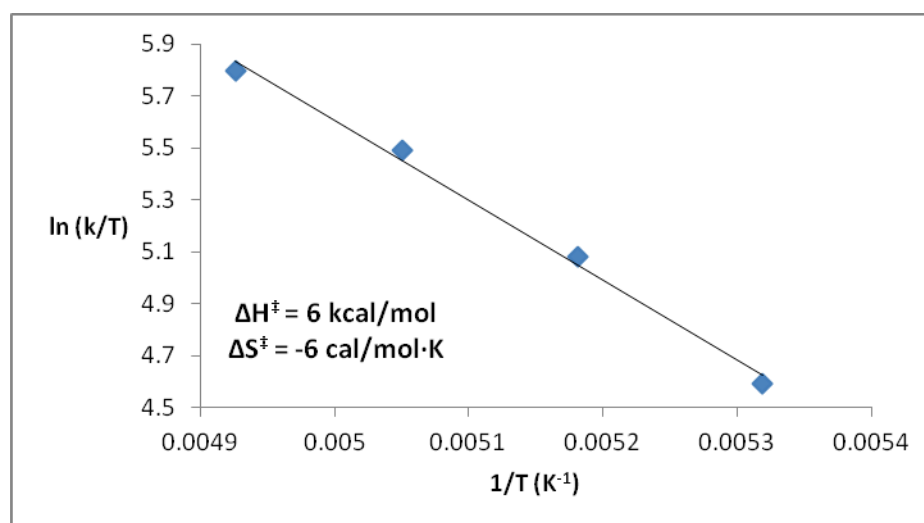
Figure 3.7 Eyring plot for O$_2$ binding with activation parameters.

The data clearly indicates reversible binding of dioxygen at the three higher temperatures. The next step is to monitor the longer process where two molecules of dioxygen bind to the complex and result in the formation of a red species. For these measurements, preliminary data suggests that much higher temperatures (> -30°C) are necessary to observe this process in a timely fashion.

Chapter 4: Two-Step Binding of O_2 to a Vanadium(III) Trisanilide Complex To Form a Non-Vanadyl Vanadium(V) Peroxo Complex

4.1 Background

Activation of dioxygen at a single transition-metal center can yield either end-bound (η^1) or side-bound (η^2) complexes.[13] It is generally held that the η^1 binding motif is more reactive than the η^2 motif.[60] The formation of side-bound O_2 complexes can proceed by initial end-on binding followed by isomerization or possibly by concerted binding of O_2 to form the side-bound product.

In spite of the fact that the two-step activation of O_2 to form a side-bound adduct is logical, limited evidence for this pathway exists. Cases where both forms of binding can be observed are rare, and there are few quantitative kinetic studies in which the rates of binding and interconversion have been directly measured. Kinetic data obtained for the treatment of four- and five-coordinate iridium(I) complexes with oxygen are in keeping with initial end-on binding followed by rapid rearrangement upon dissociation of a ligand,[61] but since ligand dissociation is a prerequisite for η^2 coordination, that result is not reflective of systems having an open coordination site, where η^2 binding could in principle occur directly. Treatment of a Cu^I complex with O_2 leads to a side-bound O_2 complex that density functional theory (DFT) calculations indicate is formed by initial end-on binding followed by a low-barrier isomerization to give the final side-bound product.[62] As reported in previous chapters that increasing the steric constraints with bulky ligands yields bis-superoxo binding of O_2 in the complex $(\eta^1\text{-}O_2)_2Pd(IPr)_2$[43] as opposed to single peroxo binding in $(\eta^2\text{-}O_2)Pd(IMes)_2$.[22]

Vanadium peroxo complexes are important as both natural[63] and industrial[64] oxidation catalysts. Vanadium peroxides are typically formed from V^{IV} or V^{V} by reaction with hydrogen peroxide or alkyl hydroperoxides;[65] there are limited examples where O_2 is the oxidant.[66] In fact, there are only a limited number of cases in which structurally characterized early transition-metal peroxo complexes have been prepared directly by reaction with O_2.[67] In the case of V^{III} complexes, oxidation by O_2 typically produces a V^{V} oxo species resulting from a bimetallic, four-electron reduction of O_2.[68] This Chapter is on studies of O_2 binding to the sterically crowded early transition-metal complex $V(N[^tBu]Ar)_3$ (Ar = 3,5-$Me_2C_6H_3$), which proceeds through an η^1-peroxo complex.

4.2 Results and Discussion

The reactions of $V(N[^tBu]Ar)_3$ with a variety of oxygen atom transfer (OAT) reagents to form cleanly the vanadium oxo complex $O{\equiv}V(N[^tBu]Ar)_3$ were recently investigated.[69] The $O{\equiv}V$ bond in $O{\equiv}V(N[^tBu]Ar)_3$ (154 ± 3 kcal/mol)[69] is strong enough that the reaction of $V(N[^tBu]Ar)_3$ with O_2 to generate an O atom is thermodynamically favorable, as shown in Eqn. (4.1):

$$V(N[^tBu]Ar)_3 + O_2 \rightarrow O{\equiv}V(N[^tBu]Ar)_3 + O \qquad \Delta H = \text{-35kcal/mol} \qquad (4.1)$$
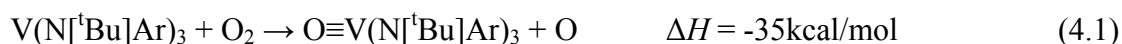
The reaction of $V(N[^tBu]Ar)_3$ with excess O_2 in toluene at −78 °C irreversibly produced a forest-green-colored solution, in contrast to the red-orange color of $O{\equiv}V(N[^tBu]Ar)_3$. NMR studies showed the green complex to be a diamagnetic species that slowly decomposed upon warming with minimal production of $O{\equiv}V(N[^tBu]Ar)_3$. Addition of excess $V(N[^tBu]Ar)_3$ followed by warming to room temperature did lead to

production of O≡V(N[^{t}Bu]Ar)$_3$. These observations suggested the sequence of reactions shown in Scheme 4.1.
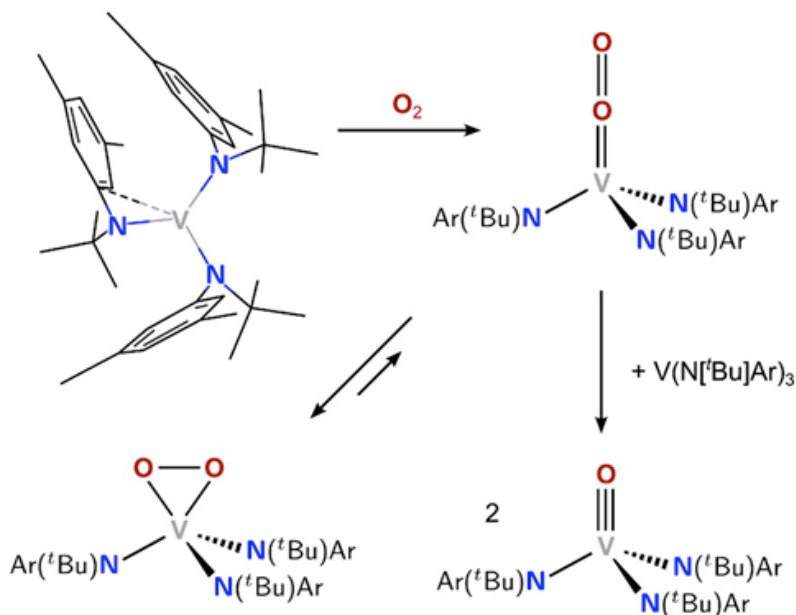
Scheme 4.1 Reaction of O$_2$ with V(N[^{t}Bu]Ar)$_3$

Initial attempts to isolate pure crystals of (η^2-O$_2$)V(N[^{t}Bu]Ar)$_3$ were frustrated by contamination with O≡V(N[^{t}Bu]Ar)$_3$, which has the same unit cell parameters as (η^2-O$_2$)V(N[^{t}Bu]Ar)$_3$ and readily cocrystallizes with it. Since the reaction of (η^2-O$_2$)V(N[^{t}Bu]Ar)$_3$ with V(N[^{t}Bu]Ar)$_3$ produces O≡V(N[^{t}Bu]Ar)$_3$, it was felt that reaction of a weakly bound nitrile adduct of V(N[^{t}Bu]Ar)$_3$ would minimize the concentration of free V(N[^{t}Bu]Ar)$_3$, resulting in cleaner formation of (η^2-O$_2$)V(N[^{t}Bu]Ar)$_3$ with less production of O≡V(N[^{t}Bu]Ar)$_3$ when O$_2$ was delivered to a concentrated solution of V(N[^{t}Bu]Ar)$_3$. Stopped-flow kinetic and NMR studies would later show that at temperatures below −30 °C, the reaction of (η^2-O$_2$)V(N[^{t}Bu]Ar)$_3$ and V(N[^{t}Bu]Ar)$_3$ is sufficiently slow that tempering the reactivity of V(N[^{t}Bu]Ar)$_3$ by this weak ligand binding is not required when O$_2$ is present in excess. A fortuitous byproduct of the

"nitrile method" was the accidental discovery of the pivaloylimido complex $^tBuC(=O)N\equiv V(N[^tBu]Ar)_3$, as discussed later.

The "nitrile method" proved to be a facile way to prepare and ultimately to isolate gram quantities of $(\eta^2\text{-}O_2)V(N[^tBu]Ar)_3$ at room temperature. ^{51}V NMR spectroscopy showed no contamination by $O\equiv V(N[^tBu]Ar)_3$ (-171 ppm) and only a peak at 198 ppm due to $(\eta^2\text{-}O_2)V(N[^tBu]Ar)_3$. This is a very high frequency relative to those for known V^V peroxides (-520 to -650 ppm)[70] and is reflective of the unique ligand environment used to support the vanadium peroxide moiety in $(\eta^2\text{-}O_2)V(N[^tBu]Ar)_3$, including the lack of a vanadyl moiety. Diffraction-quality crystals of $(\eta^2\text{-}O_2)V(N[^tBu]Ar)_3$ were obtained by recrystallizing $(\eta^2\text{-}O_2)V(N[^tBu]Ar)_3$ from pentane at -35 °C. The asymmetric unit consists of one-third of a molecule, the remainder being generated by a crystallographic threefold axis (Figure 4.1). This necessitates the disorder of the peroxo moiety over three positions, as clearly seen in the density map (Figure 4.2). The full molecule has a five-coordinate V^V center with two of the coordination sites occupied by the two oxygen atoms of the peroxo ligand. This is the first structurally characterized example of a non-vanadyl (i.e. containng a V=O group) peroxo species,[71] with the exception of per(peroxo)vanadium structures.[72] The structure exhibits unequal V–O bond distances (1.777(4) and 1.908(4) Å), the average of which (1.843 Å) is shorter than the average V–O_{peroxo} distance of structurally characterized vanadium peroxo systems (1.878 Å).[73] The oxygen atom that is farther away (O2) appears to engage in a weak hydrogen bond with a neighboring $CH_{aryl\text{-}Me}$ (O$\cdots$H = 2.68 Å, C(H)$\cdots$O = 3.36 Å;)[74] and furthermore is located trans to a V–N bond [141.5(1)°]. Thus, the V–O_2 bond is likely lengthened because of the synergistic influences of the hydrogen bond and the *trans* anilide ligand. The O–O

peroxide bond length [1.416(5) Å] is also short compared with the average O–O bond in known $V^V(O_2)$ complexes (average 1.430 Å, median 1.436 Å).[73]
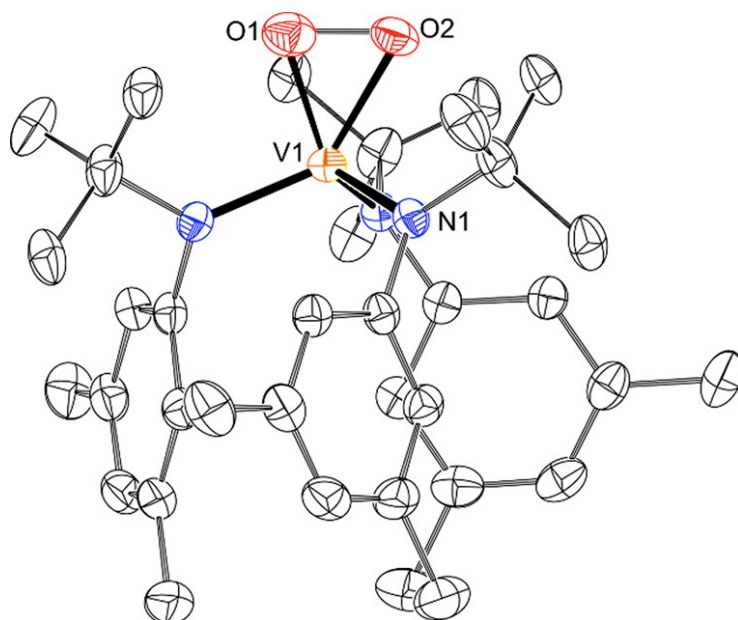
Figure 4.1 ORTEP diagram of $(\eta^2\text{-}O_2)V(N[^tBu]Ar)_3$ with thermal ellipsoids at 50% probability. H atoms, symmetry-related O atoms, and disordered ^tBu groups have been omitted for clarity. Selected distances (Å) and angles (deg): V1–N1, 1.887(1); V1–O1, 1.777(4); V1–O2, 1.908(4); O1–O2, 1.416(5); O1–V1–O2, 45.1(2).
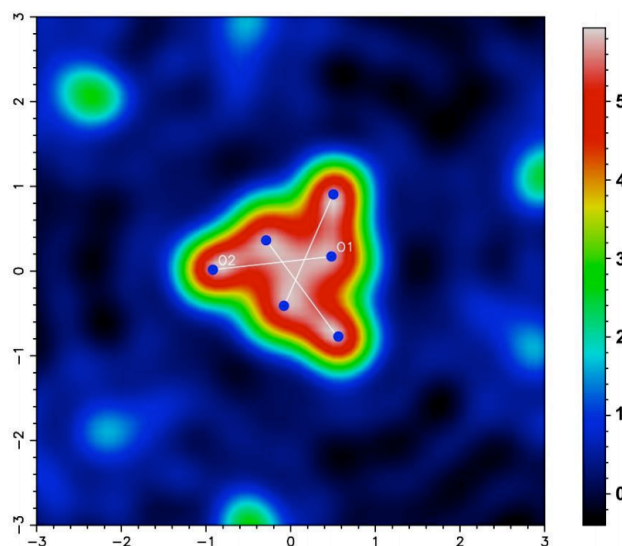
Figure 4.2 Electron density map $(e/\text{Å}^3)$ from crystal structure of $(\eta^2\text{-}O_2)V(N[^tBu]Ar)_3$ cut through the O_2 plane. Atom positions are indicated with blue spots and bonds are indicated with white lines. This shows the disordered structure which was modeled to get the final crystal structure.
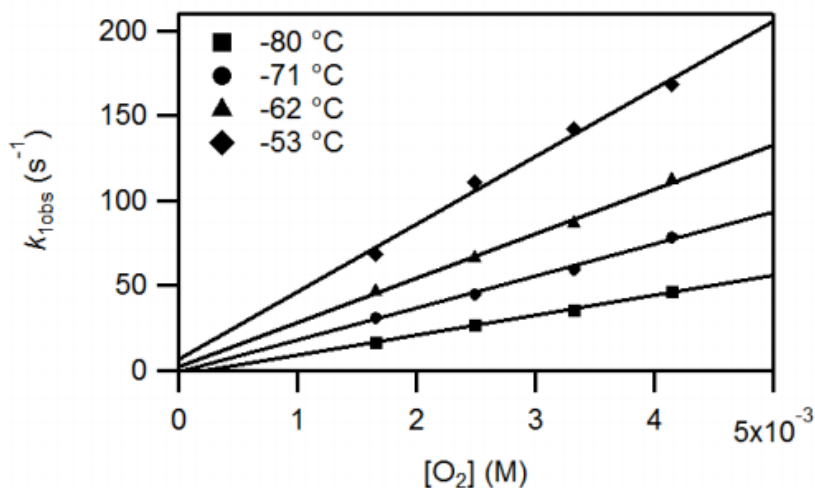
Figure 4.3 Second order rate plots for O_2 binding (η^1-peroxo formation, first process) at various concentrations (1.66 mM – 4.15 mM) over a temperature range of –80 °C to –53 °C. [V(N[^{t}Bu]Ar)$_3$] = 0.3 mM, concentrations after mixing.
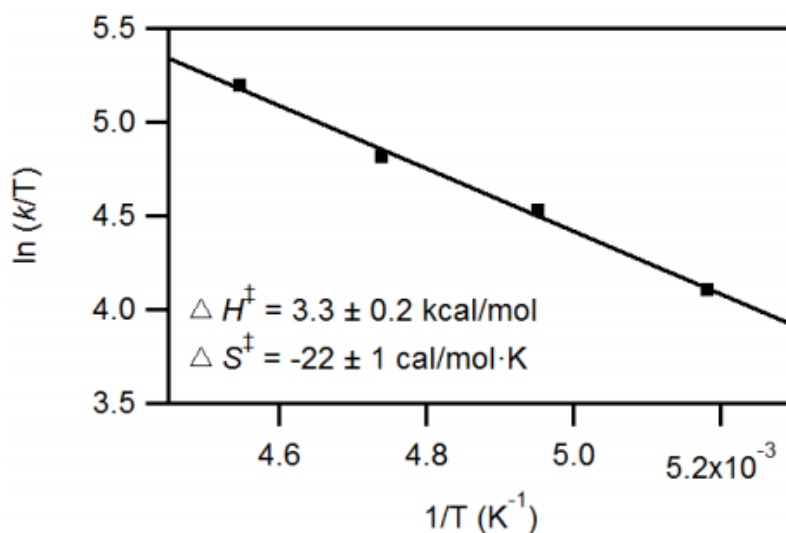
Figure 4.4 Eyring plot for O_2 binding to V(N[^{t}Bu]Ar)$_3$ (first process) with activation parameters.

Stopped-flow kinetic studies gave clear evidence for a two-step binding process. All reactions were studied under pseudo-first-order conditions using excess O_2. Binding of O_2 to V(N[^{t}Bu]Ar)$_3$ occurred within seconds at low temperatures (-80 to -53 °C). Upon mixing, a rapid growth in absorbance was observed across most of the spectrum (λ = 400–682 nm) with concomitant decay occurring at longer wavelengths (λ = 682–800 nm).

The first process showed a linear dependence on $[O_2]$ (Figure 4.3) and a low activation enthalpy ($\Delta H^{\ddagger}$) of 3.3 ± 0.2 kcal/mol (Figure 4.4), typical of O_2 binding at a vacant metal site.[43,75]

This rapid, low-barrier process was followed by a slower process characterized by an increase in absorbance at λ = 400–682 nm with concomitant decay occurring at λ = 682–800 nm. This second slower step, which was found to be independent of $[O_2]$ and to have a much higher $\Delta H^{\ddagger}$ and much lower activation entropy ($\Delta S^{\ddagger}$) than the initial bimolecular reaction step ($\Delta H^{\ddagger}$ = 10.3 ± 0.9 kcal/mol and $\Delta S^{\ddagger}$ = −6 ± 4 cal mol^{-1} K^{-1}; Figure 4.5), is assigned to the rearrangement of $(\eta^1\text{-}O_2)V(N[^tBu]Ar)_3$ to $(\eta^2\text{-}O_2)V(N[^tBu]Ar)_3$ (Scheme 4.1). Solution calorimetric studies of the reaction of $V(N[^tBu]Ar)_3$ with O_2 to form $(\eta^2\text{-}O_2)V(N[^tBu]Ar)_3$ (10 °C in heptane) yielded ΔH = −75.0 ± 2.0 kcal/mol.
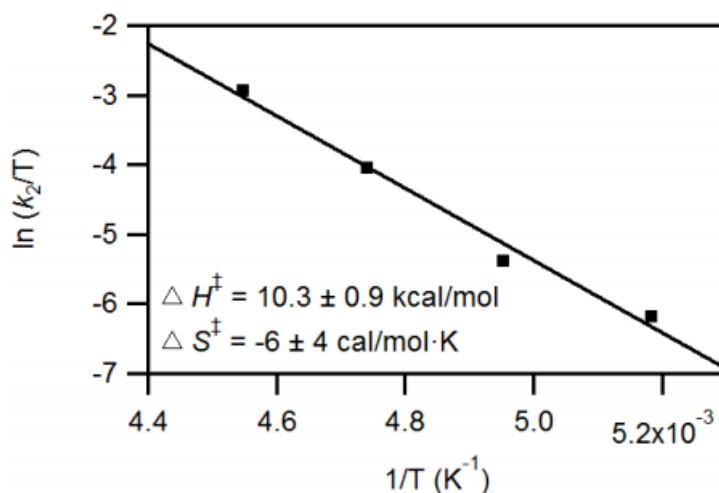
Figure 4.5 Eyring plot for isomerization from $(\eta^1\text{-}O_2)V(N[^tBu]Ar)_3$ to $(\eta^2\text{-}O_2)V(N[^tBu]Ar)_3$ (second process) with activation parameters.

Binding of O_2 to $V(N[^tBu]Ar)_3$ was investigated computationally, and DFT geometry optimizations of the $\eta^1\text{-}O_2$ and $\eta^2\text{-}O_2$ complexes were carried out for both the

singlet and triplet spin states. The minimal-energy triplet geometry was found to be 26.2 kcal/mol higher than the minimal singlet geometry. For the singlet manifold, two stable structures were computed, corresponding to the η^1 complex $(\eta^1\text{-}O_2)V(N[^tBu]Ar)_3$ and the η^2 complex $(\eta^2\text{-}O_2)V(N[^tBu]Ar)_3$. A small energy difference of only 4.2 kcal/mol was found for the two isomers, favoring η^2 binding. The DFT-minimized structure of $(\eta^2\text{-}O_2)V(N[^tBu]Ar)_3$ contains a more symmetrical peroxo ligand than found experimentally. The computed V–O distances are 1.830 and 1.851 Å, and the O–O distance is 1.471 Å. Minimization of $(\eta^2\text{-}O_2)V(N[^tBu]Ar)_3$ while constraining it to have the crystallographic V–O and O–O metrics gave an energy that is only 2.4 kcal/mol higher, an increase for which the formation of the weak hydrogen bond (<4 kcal/mol) compensates.[74a]

The computed metrical parameters and electronic structure of $(\eta^1\text{-}O_2)V(N[^tBu]Ar)_3$ are consistent with its formulation as a V^V peroxo as opposed to a V^{IV} superoxo species. The DFT-calculated $\eta^1\text{-}O_2$ complex has a V–O distance of 1.676 Å, an O–O distance of 1.307 Å, and a V–O–O bond angle of 179.3°. The Mayer bond order[76] of the O–O bond decreases upon isomerization, going from 0.98 in $(\eta^1\text{-}O_2)V(N[^tBu]Ar)_3$ to 0.82 in $(\eta^2\text{-}O_2)V(N[^tBu]Ar)_3$, consistent with a more activated, albeit less accessible, O_2 in the side-bound adduct. The end-bound complex has a Mayer bond order of 1.13 for the V–O bond, which is an increase in multiple-bond character with respect to the V–O bonds in $(\eta^2\text{-}O_2)V(N[^tBu]Ar)_3$ (ave 0.93 Å), consistent with the short V–O bond length. In fact, the main contributing resonance structure according to natural resonance theory analysis[77] contains a V–O double bond and an O–O single bond; the main contributing resonance structure for $(\eta^2\text{-}O_2)V(N[^tBu]Ar)_3$ contains two V–O single bonds and an O–O single bond.

The potential energy surface for the isomerization of $(\eta^1\text{-}O_2)V(N[^tBu]Ar)_3$ to $(\eta^2\text{-}O_2)V(N[^tBu]Ar)_3$ was mapped by varying the V–O–O bond angle from 180 to 67° (Figure 4.6). A transition state $([(\eta^1\text{-}O_2)V(N[^tBu]Ar)_3]^{\ddagger})$ was located at a V–O–O angle of 109.8°, providing an activation energy of 12.2 kcal/mol for the η^1 to η^2 process, which is in good agreement with experiment.

The isoelectronic chromium nitrosyl complexes, which are known to be N-bound, have been previously isolated and were readily deoxygenated by (THF)V(Mes)$_3$ to give the terminal Cr^{VI} nitrido species.[78]

If the analogous $\eta^1\text{-}O_2$ species exists in equilibrium with peroxo $(\eta^2\text{-}O_2)V(N[^tBu]Ar)_3$, then addition of $V(N[^tBu]Ar)_3$ could be used to deoxygenate peroxo $(\eta^1\text{-}O_2)V(N[^tBu]Ar)_3$ to give 2 equiv of oxo $O\equiv V(N[tBu]Ar)_3$ (Scheme 4.1). Indeed, ^1H NMR spectroscopic kinetic studies of the reaction of $(\eta^2\text{-}O_2)V(N[^tBu]Ar)_3$ with $V(N[^tBu]Ar)_3$ confirmed this, and an activation energy of 14 ± 3 kcal/mol was determined for this process. The computed $\Delta H^{\ddagger}$ for conversion of $(\eta^2\text{-}O_2)V(N[^tBu]Ar)_3$ to $(\eta^1\text{-}O_2)V(N[^tBu]Ar)_3$ (16.4 kcal/mol) is in good agreement with the experimental value. Despite the fact that it is thermodynamically comparable to N$_2$O as an OAT reagent, the deoxygenation of peroxo $(\eta^2\text{-}O_2)V(N[^tBu]Ar)_3$ by vanadium(III) complex $V(N[^tBu]Ar)_3$ is relatively slow. This is interpreted to be a result of the requisite formation of $(\eta^1\text{-}O_2)V(N[^tBu]Ar)_3$, which is sterically more accessible for OAT with $V(N[^tBu]Ar)_3$ than is $(\eta^2\text{-}O_2)V(N[^tBu]Ar)_3$, as illustrated by the Fukui functions when plotted on the electron density.[79]
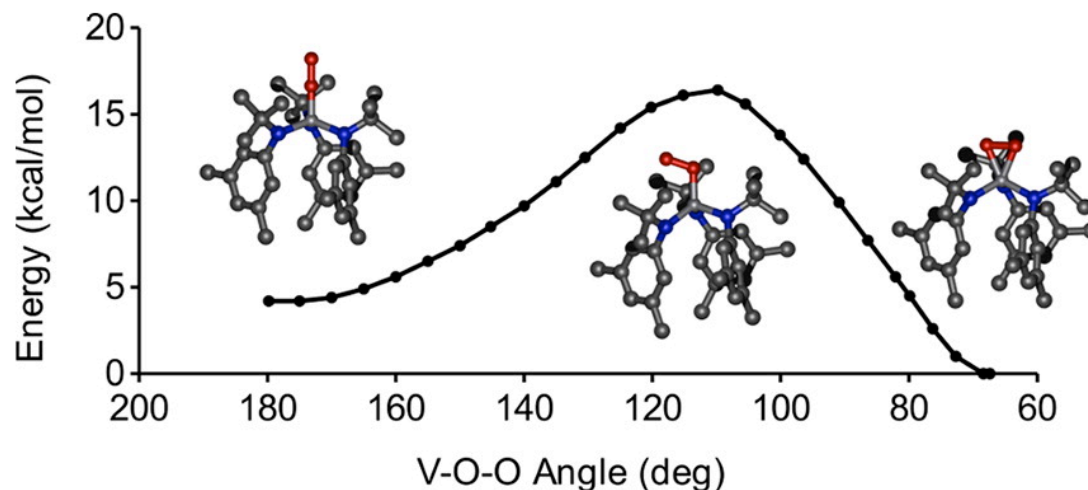
Figure 4.6 DFT-calculated potential energy surface for isomerization of (η^1-O$_2$)V(N[^{t}Bu]Ar)$_3$ to (η^2-O$_2$)V(N[^{t}Bu]Ar)$_3$.

Scheme 4.2 Experimental and DFT-calculated (in parentheses) potential energy diagram for the reaction between O$_2$ and V(N[^{t}Bu]Ar)$_3$ to ultimately form (η^2-O$_2$)V(N[^{t}Bu]Ar)$_3$. Energies are given in kcal/mol. (1 = V(N[^{t}Bu]Ar)$_3$, 2 = (η^1-O$_2$)V(N[^{t}Bu]Ar)$_3$, 3 = (η^2-O$_2$)V(N[^{t}Bu]Ar)$_3$)

Scheme 4.2 shows a combined potential energy diagram for this system in which the experimental energy of O$_2$ binding has been combined with the computed relative energies for (η^1-O$_2$)V(N[^{t}Bu]Ar)$_3$ and (η^2-O$_2$)V(N[^{t}Bu]Ar)$_3$ binding and interconversion; also incorporated in the diagram are the activation energies from the stopped-flow experiments and the ^{1}H NMR experiments. For reasons that are not yet understood, the

overall computed ΔH of binding of O_2 to $V(N[^tBu]Ar)_3$ to yield $(\eta^2\text{-}O_2)V(N[^tBu]Ar)_3$ is −51.2 kcal/mol, which is in nontrivial disagreement with the experimental value of −75 kcal/mol. In contrast, good agreement between theory and experiment was found for the computed O≡V bond strength in O≡V(N[^tBu]Ar)$_3$.[69]
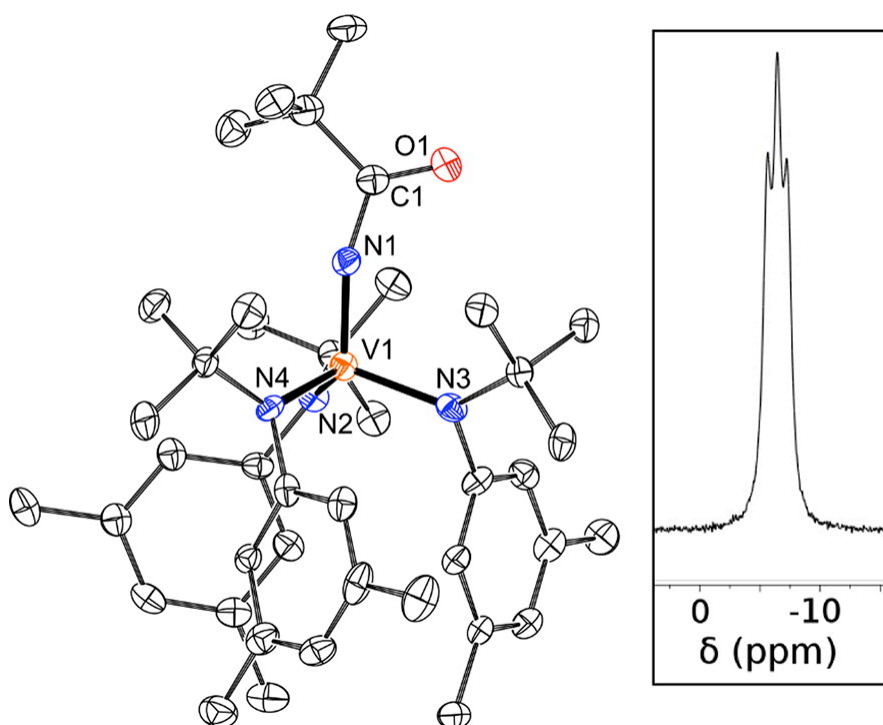
Figure 4.7 ORTEP diagram of $^tBuC(=O)N\equiv V(N[^tBu]Ar)_3$ with thermal ellipsoids at 50% probability and H atoms omitted for clarity. Selected distances (Å) and angles (deg): V1–N1, 1.695(3); V1–N2, 1.875(2); V1–N3, 1.888(2); V1–N4, 1.894(3); N1–C1, 1.390(4); C1=O1, 1.218(4); V1–N1–C1, 151.9(2); N1–C1=O1, 120.8(3); N1–C1–C11, 118.0(3). Inset: ^{51}V NMR spectrum of $^tBuC(=O)N\equiv V(N[^tBu]Ar)_3$ in THF.

Finally, during attempts to obtain pure $(\eta^2\text{-}O_2)V(N[^tBu]Ar)_3$ by addition of ^tBuCN to $V(N[^tBu]Ar)_3$ followed by reaction with O_2, it was observed that at −45 °C a change in color from royal purple to dark green occurred over the course of 1 h. The reaction mixture was assayed by ^{51}V NMR spectroscopy and found to contain $(\eta^2\text{-}O_2)V(N[^tBu]Ar)_3$ and a new product whose ^{51}V NMR signal was split into a 1:1:1 triplet (Figure 4.7 inset). Crystals of the new product were isolated manually and determined to

be the result of oxidation of the bound nitrile to form the acylimido species $^tBuC(=O)N\equiv V(N[^tBu]Ar)_3$ (Figure 4.7). Acylimido moieties have been prepared by the treatment of terminal metal nitrides with acylating agents.[80] Rarer is the direct oxidation of a metal-bound nitrile to form the acylimido.[81] In $^tBuC(=O)N\equiv V(N[^tBu]Ar)_3$, the spin–spin coupling is assigned to $^1J^{14}_{N-}{}^{51}_V$ coupling (83 Hz). The identity of $^tBuC(=O)N\equiv V(N[^tBu]Ar)_3$ was confirmed by its independent synthesis from $Na[N\equiv V(N[^tBu]Ar)_3]^{82}$ and pivaloyl chloride.

Despite the industrial and biological importance of oxidation reactions mediated by metal centers,[63,64] the formation of early metal peroxides by the direct reaction of a low-valent and unsaturated transition-metal complex with O_2 is still remarkably rare. The first non-vanadyl V^V peroxide from the controlled reaction of an unsaturated V^{III} complex with O_2 has been isolated and structurally characterized. Moreover, the $\eta^1–\eta^2$ conversion in O_2 binding, which is a pathway that has been proposed as a general step in η^2-peroxide formation from O_2, has been observed.[13] Solution calorimetric studies of the binding of O_2 to $V(N[^tBu]Ar)_3$ suggest that peroxo (η^2-$O_2)V(N[^tBu]Ar)_3$) should be a potent oxidant. It is encouraging that careful tailoring of the reaction conditions led to the clean generation of peroxide (η^2-$O_2)V(N[^tBu]Ar)_3$) from O_2, suggesting that similar control may be applied more generally to other low-valent and unsaturated early transition-metal complexes, leading to a class of thermodynamically potent OAT reagents.

4.3   Conclusions

Treatment of $V(N[^tBu]Ar)_3$ (Ar = 3,5-$Me_2C_6H_3$) with O_2 was shown by stopped-flow kinetic studies to result in the rapid formation of (η^1-$O_2)V(N[^tBu]Ar)_3$ ($\Delta H^{\ddagger} = 3.3 \pm 0.2$ kcal/mol and $\Delta S^{\ddagger} = -22 \pm 1$ cal/mol K), which subsequently isomerizes to (η^2-

$O_2)V(N[^tBu]Ar)_3$ ($\Delta H^{\ddagger} = 10.3 \pm 0.9$ kcal•mol and $\Delta S^{\ddagger} = -6 \pm 4$ cal•mol^{-1}•K^{-1}). The enthalpy of binding of O_2 to form (η^2-O_2)V(N[^tBu]Ar)$_3$ is -75.0 ± 2.0 kcal/mol, as measured by solution calorimetry. The reaction of (η^2-O_2)V(N[^tBu]Ar)$_3$ and

V(N[^tBu]Ar)$_3$ to form 2 equiv of O≡V(N[^tBu]Ar)$_3$ occurs by initial isomerization of (η^2-O_2)V(N[^tBu]Ar)$_3$ to (η^1-O_2)V(N[^tBu]Ar)$_3$. The results of computational studies of this rearrangement ($\Delta H = 4.2$ kcal/mol; $\Delta H^{\ddagger} = 16$ kcal/mol) are in accord with experimental data ($\Delta H = 4 \pm 3$ kcal/mol; $\Delta H^{\ddagger} = 14 \pm 3$ kcal/mol). With the aim of suppressing the formation of O≡V(N[^tBu]Ar)$_3$, the reaction of O_2 with V(N[^tBu]Ar)$_3$ in the presence of ^tBuCN was studied. At -45 °C, the principal products of this reaction are (η^2-O_2)V(N[^tBu]Ar)$_3$ and $^tBuC(=O)N≡V(N[^tBu]Ar)_3$, in which the bound nitrile has been oxidized. Crystal structures of (η^2-O_2)V(N[^tBu]Ar)$_3$ and $^tBuC(=O)N≡V(N[^tBu]Ar)_3$ are reported.

4.4   Experimental

A. Synthesis

General Methods. Unless otherwise stated, all manipulations were carried out either in a Vacuum Atmospheres model MO-40M glovebox under an atmosphere of N_2 or using standard Schlenk techniques. All solvents were degassed and dried using a solvent-purification system provided by Glass Contour. After purification, all solvents were stored under an atmosphere of N_2 over 4 Å molecular sieves. Deuterated benzene, deuterated toluene and deuterated chloroform (Cambridge Isotope Labs) was dried by stirring over CaH_2 for 24 h and was subsequently vacuum-transferred onto 4 Å molecular sieves. Complexes V([^tBu]Ar)$_3$ and Na[N≡V([^tBu]Ar)$_3$] were prepared according to literature methods[83, 84] and tert-butyl nitrile was distilled from CaH_2. All other reagents

were used as supplied by the vendor without further purification. Celite 435 (EMD Chemicals), alumina (Aldrich) and 4 Å molecular sieves were dried prior to use by heating at 200 °C for 48 h under dynamic vacuum. All glassware was oven dried at 220 °C prior to use. NMR spectra were obtained on either a Varian 500 Inova spectrometer equipped with an Oxford Instruments Ltd. superconducting magnet, a Bruker 400-

AVANCE spectrometer equipped with a Magnex Scientific superconducting magnet, or a Varian Mercury 300 spectrometer equipped with an Oxford Instruments Ltd. superconducting magnet. Proton NMR spectra were referenced to residual C_6D_5H (7.16 ppm), residual $(CH_1D_2)C_6D_5$ (2.08 ppm) or residual CCl_3H_1 (7.26 ppm) and ^{51}V NMR spectra were referenced externally to $OVCl_3$. IR spectra were collected on a Bruker Tensor 37 FT-IR spectrophotometer. Elemental analysis was performed by Midwest Microlab, Indianapolis, IN.

Treatment of V([^{t}Bu]Ar)$_3$ with O$_2$ at 20 °C. A C_6D_6 solution (0.48 g) of V([^{t}Bu]Ar)$_3$ (0.04 g, 0.07 mmol) was transferred to a J-Young tube. Three freezepump-thaw cycles were performed. An atmosphere of O_2 was introduced into the thawed solution. The solution turned from dark green to orange/red over 5 min. An Evans method magnetic susceptibility measurement indicated that the reaction mixture was diamagnetic and ^1H NMR spectroscopy revealed a complex mixture of species which included $O\equiv V(N[^tBu]Ar)_3$ and $HN[^tBu]Ar$.

Treatment of V([^{t}Bu]Ar)$_3$ with O$_2$ at −78 °C. A solution of V([^{t}Bu]Ar)$_3$ (0.35 g, 0.61 mmol) in 10 mL tetramethylsilane was placed in a 100 mL side-arm round-bottomed flask. The flask was transferred to the vacuum line, a freeze-pump-thaw cycle was

performed before an atmosphere of O_2 was introduced at −78 °C. The temperature was maintained while the solution was stirred under an atmosphere of O_2 for 20 min. A dark precipitate began forming as the O_2 was added. The solvent was removed at low temperature and the solids were transferred to the glove box. Dark green solids (0.11 g) were quickly recovered and stored at −35 °C. ^{51}V NMR of the sample revealed a mixture of O≡V(N[^{t}Bu]Ar)$_3$ and (η^2-O$_2$)V(N[^{t}Bu]Ar)$_3$. (Figure 4.8)
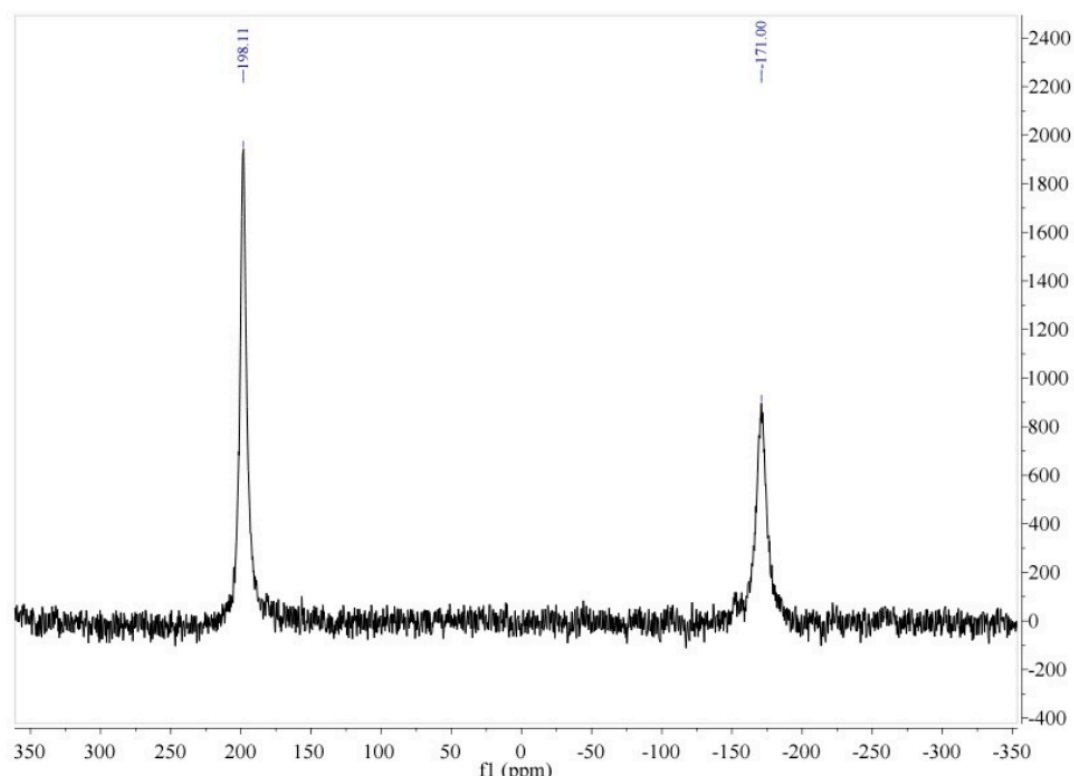
Figure 4.8 ^{51}V NMR spectrum of solids from reaction V([^{t}Bu]Ar)$_3$ with O_2 at −78 °C dissolved in toluene revealing a mixture of O≡V(N[^{t}Bu]Ar)$_3$ (−171.00 ppm) and (η^2-O$_2$)V(N[^{t}Bu]Ar)$_3$ (198.11 ppm).

Preparation of ^{t}BuC(=O)N≡V(N[^{t}Bu]Ar)$_3$. A THF (3 mL) solution of Na[N≡V([^{t}Bu]Ar)$_3$] (0.10 g, 0.16 mmol) was treated with a THF (2 mL) solution of pivaloyl chloride (0.021 g, 0.174 mmol). The solution turned from pale yellow to bright red over the course of 10 min. The solution was allowed to stir for 1 h, before the solvent was removed under vacuum. The solid was triturated twice with benzene and then taken

up in benzene and filtered through Celite. Removal of benzene under vacuum left 0.081 g

of red solids (0.12 mmol, 75%) 1H NMR (C$_6$D$_6$, δ ppm) 6.70 (3H, p-Ar), 6.6 (3H, br, o-

Ar) 5.2 (3H, br, o-Ar) 2.15 (18H, Me), 1.60 (9H, ^{t}Bu(CO)), 1.47 (9H, ^{t}Bu); ^{1}H NMR

(CDCl$_3$, δ ppm) 6.73 (3H, p-Ar), 6.5 (3H, br, o-Ar) 4.8 (3H, br, o-Ar) 2.14 (18H, Me),

1.42 (9H, ^{t}Bu(CO)), 1.23 (9H, ^{t}Bu). 13C NMR (CDCl$_3$, δ ppm) 155.3 (C$_{Ar}$), 136.1 (C$_{Ar}$),

127.2 (br, C$_{Ar}$), 126.8 (C$_{Ar}$), 65.5 ((CH$_3$)$_3$C), 40.4 ((CH$_3$)$_3$C(CO)), 32.3 ((CH$_3$)$_3$C), 28.8

((CH$_3$)$_3$C(CO)), 21.6 (C$_{Ar}$-CH$_3$). Note: the signal for the carbonyl carbon could not be

located, likely due to ^{14}N coupling. ^{51}V NMR (THF, δ ppm) –6.43 (triplet, ^{1}J^5 ^{1}V-^{14} N

83Hz). IR (ATR, cm^{-1}) 2964, 2923, 2862, 1616, 1599, 1584, 1456, 1385, 1357, 1284,

1257, 1189, 1152, 1042, 1023, 940, 919, 880, 846, 713, 690, 645. Anal. Calcd for

C41H63N4V1O1: C, 72.54; H, 9.35; N, 8.25. Found: C, 72.49; H, 9.27; N, 8.21.
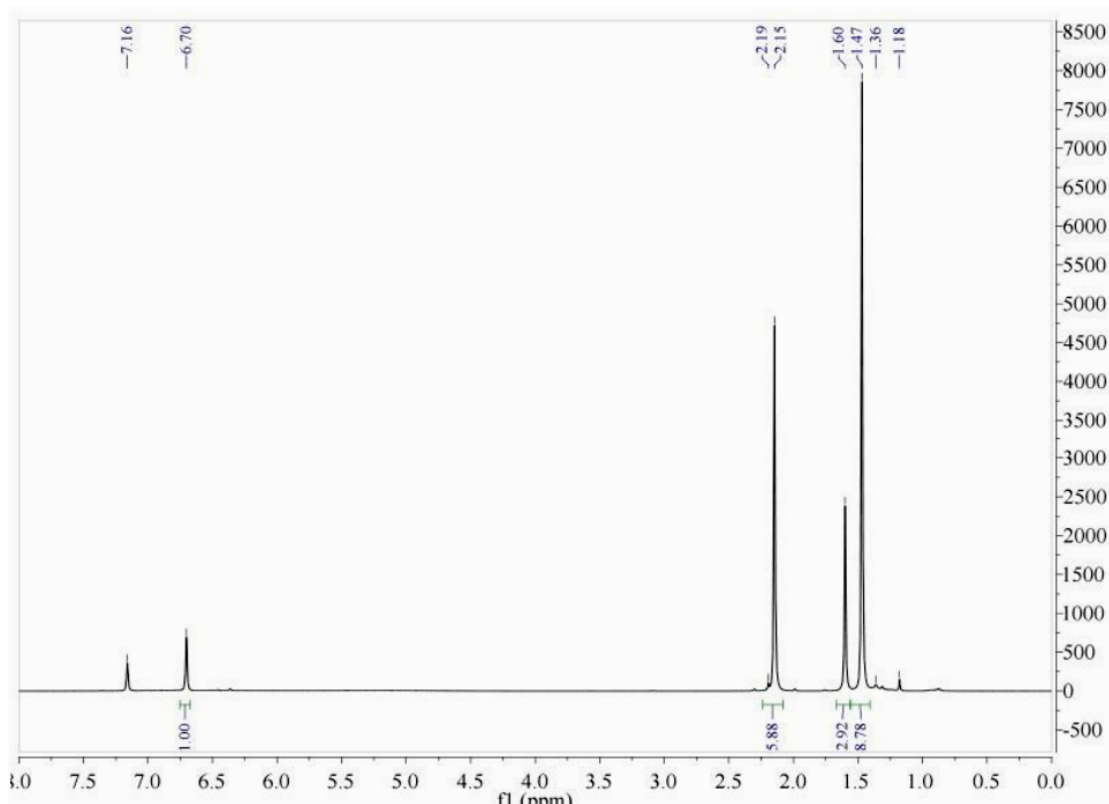
Figure 4.9 ^{1}H NMR spectrum of ^{t}BuC(=O)N≡V(N[^{t}Bu]Ar)$_3$ in C$_6$D$_6$
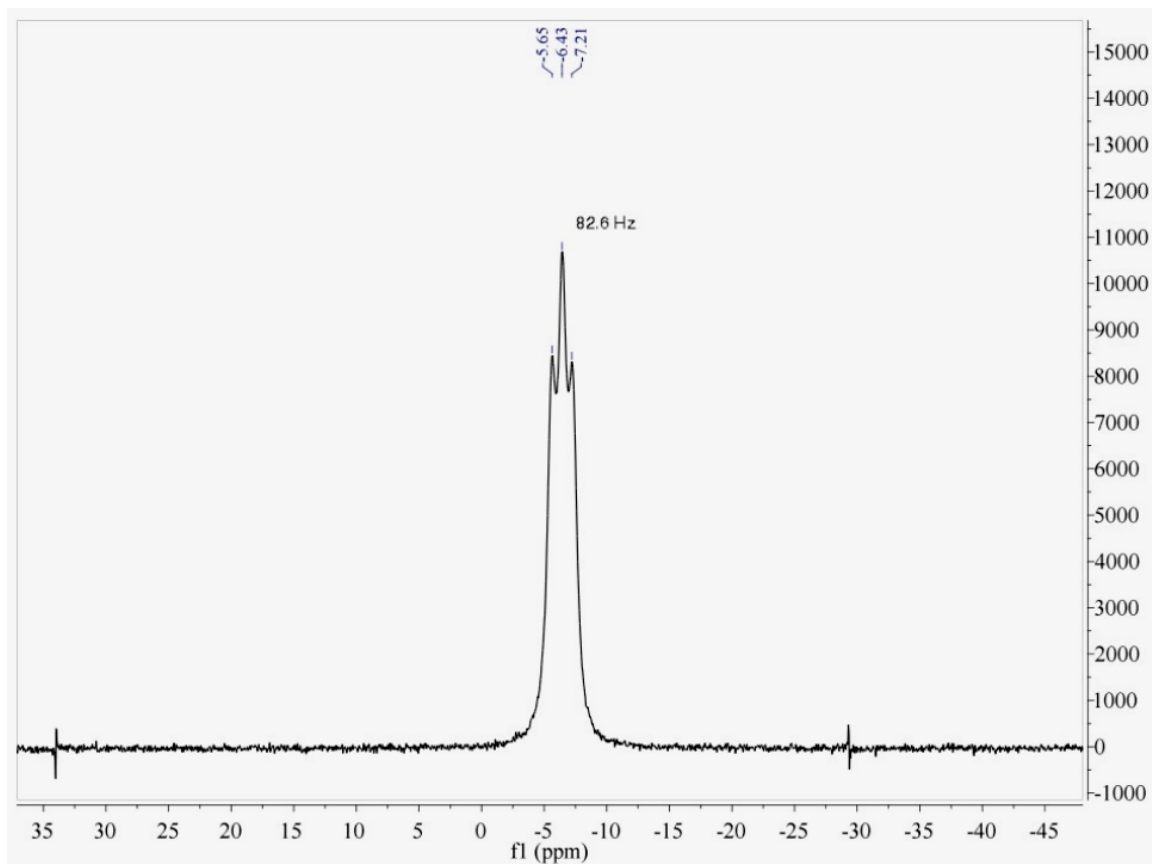
Figure 4.10 ^{51}V NMR spectrum of $^tBuC(=O)N\equiv V(N[^tBu]Ar)_3$ in THF.

Treatment of $V(N[^tBu]Ar)_3$ with ^tBuCN and O_2 at –45.2 °C. A solution of $V(N[^tBu]Ar)_3$ (0.9 g, 1.5 mmol) in pentane (20 mL) was treated with tert-butyl nitrile (0.16 g, 1.8 mmol) turning the solution from dark black/green to dark purple. The solution of $^tBuCN\cdot V(N[^tBu]Ar)_3$ was transferred to a 50 mL side-arm round-bottomed flask and capped with a septum. The flask was remove from the glove box and cooled to –45.2 °C in a dry ice/chlorobenzene bath.[85] While stirring, the septum was pierced two needles, one delivering a flow of O_2 and one acting as a relief needle. A slow color change from purple to black/green was observed over the course of 1 h during which time a purge of O_2 was maintained. The solvent was immediately removed under vacuum. Once the solvent was removed, the flask was allowed to warm to 20 °C and held there for 20 min to ensure that all tert-butyl nitrile has been removed. The flask was transferred to

the glove box and the solids were analyzed by ^{51}V NMR spectroscopy and found to be a mixture of $(\eta^2\text{-}O_2)V(N[^tBu]Ar)_3$ and $^tBuC(=O)N\equiv V(N[^tBu]Ar)_3$.
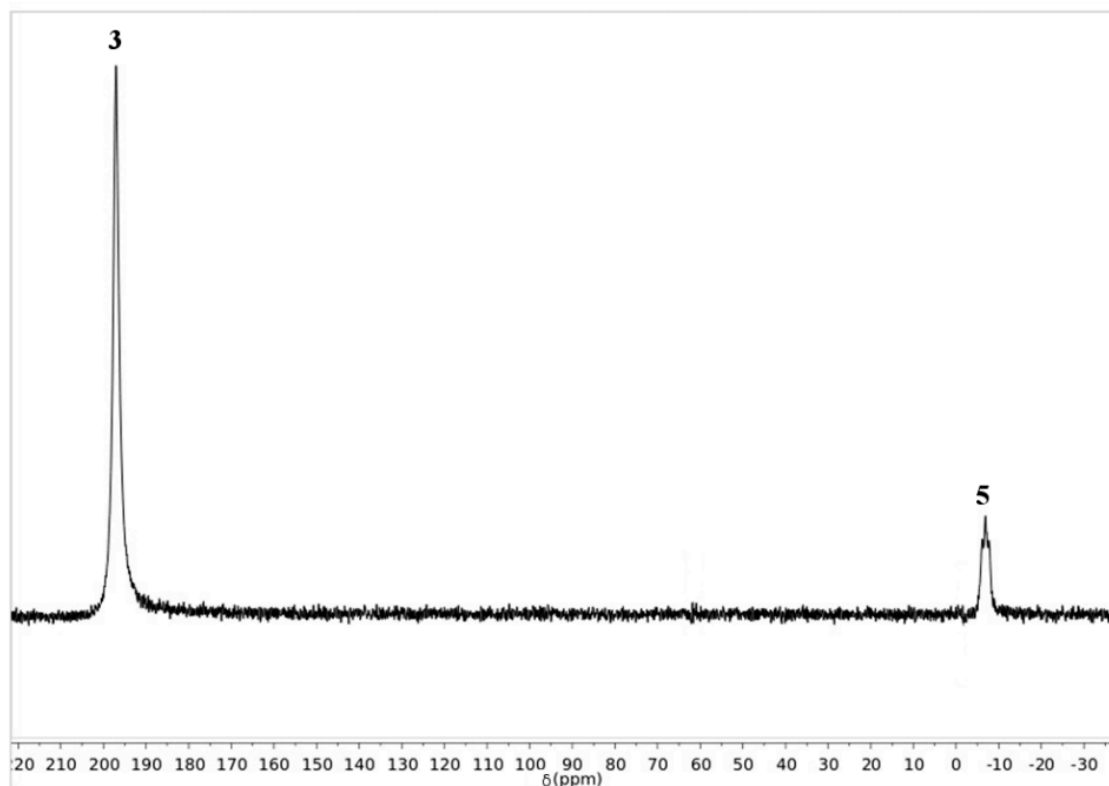
Figure 4.11 ^{51}V NMR spectrum from treatment of $V(N[^tBu]Ar)_3$ with ^tBuCN and O_2 at $-45.2\ °C$. $(\eta^2\text{-}O_2)V(N[^tBu]Ar)_3 = \textbf{3}$, $^tBuC(=O)N\equiv V(N[^tBu]Ar)_3 = \textbf{5}$.

Preparation of O$_2$V(N[^{t}Bu]Ar)$_3$. A solution of $V(N[^tBu]Ar)_3$ (1.3 g, 2.2 mmol) in pentane (25 mL) was treated with tert-butyl nitrile (0.21 g, 2.5 mmol) turning the solution from dark black/green to dark purple. The solution of $^tBuCN\cdot V(N[^tBu]Ar)_3$ was transferred to a 50mL side-arm round-bottomed flask and capped with a septum. The flask was removed from the glove box and, while stirring, the septum was pierced two needles, one delivering a flow of O_2 and one acting as a relief needle. An immediate color change from purple to black/green was observed. Purging with O_2 continued for 120 s to ensure complete conversion. The solvent was immediately remove under vacuum at such a rate that the flask was kept lower than 0 °C as determined by frozen condensation on

the exterior of the flask. The flask was kept under vacuum until it had warmed to 20 °C and held there for 20 min to ensure that all tert-butyl nitrile had been removed. The flask was transferred to the glove box and 0.97 g of black solids were collected (1.6 mmol, 73%) Due to the thermal instability of the product (vida supra), ^{13}C NMR and elemental analysis were not obtained. ^{1}H NMR (CDCl$_3$, δ ppm) 6.76 (1H, p-Ar), 4.50 (br, o-Ar), 2.20 (3H, Me), 2.09 (3H, Me), 1.17 (9H, tBu); 51V NMR ((CD$_3$)C$_6$D$_5$, δ ppm) 198.1; 51V NMR (CDCl$_3$, δ ppm) 216.9; 51V NMR (C$_5$H$_{18}$, ppm) 183.1. IR (ATR, cm^{-1}) 2977, 2956, 2927, 2863, 1599, 1583, 1460, 1387, 1356, 1285, 1259, 1232, 1170, 1149, 1042, 1017, 991, 933, 881, 845, 712, 693, 618, 581, 509, 477, 426.
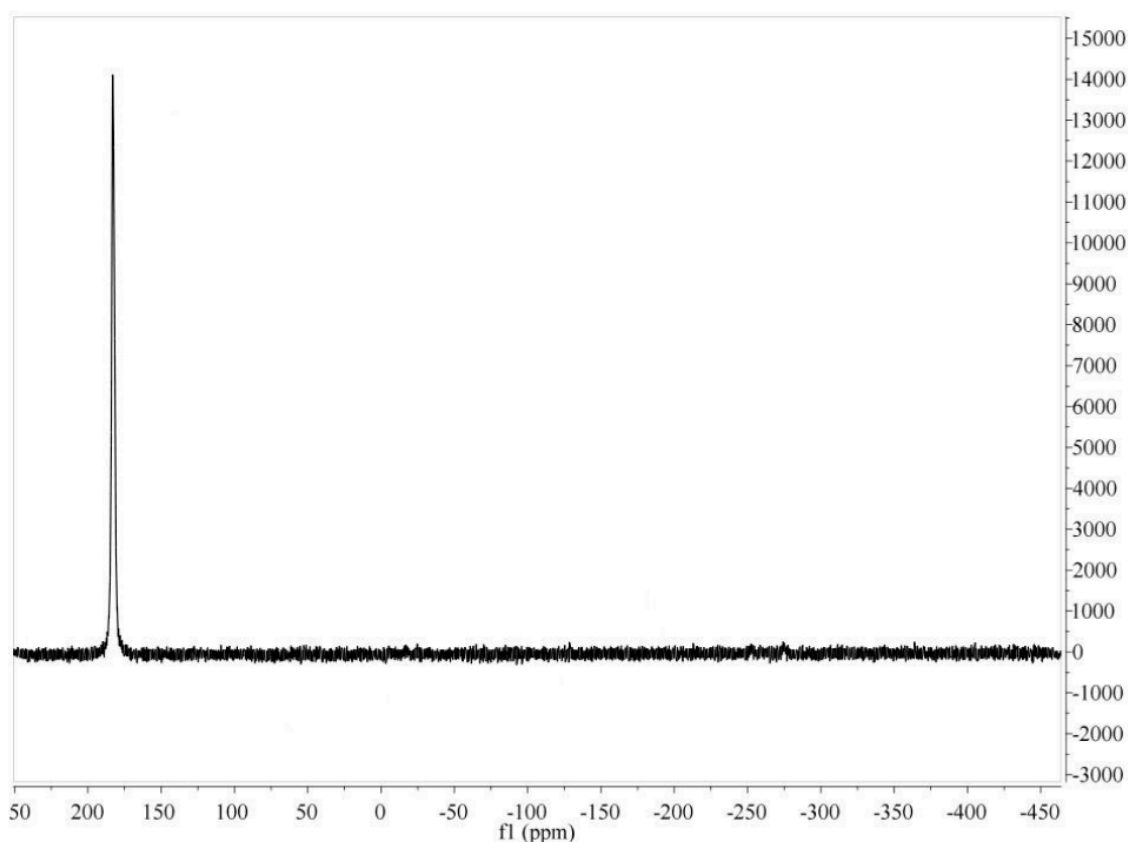
Figure 4.12 ^{51}V NMR spectrum of (η^2-O$_2$)V(N[^{t}Bu]Ar)$_3$ in pentane.

^{1}H NMR spectroscopic study of the kinetics of the reaction of $O_2V(N[^tBu]Ar)_3$ with $V(N[^tBu]Ar)_3$ to form $O\equiv V(N[^tBu]Ar)_3$. In the glove box, a solution was prepared of 0.1222 g (0.2108 mmol) $V(N[^tBu]Ar)_3$ in 6 mL toluene-d^8, yielding a 0.035 M solution. To separate NMR tubes, 1 mL (0.0400 mmol) of this solution was added. The tubes were sealed with a screw cap and Teflon faced rubber septum and taken from the glove box. Kinetic studies were performed at 0, 10, and 22 °C by first tuning on a Bruker 300 or 400 Avance NMR spectrometer. Following temperature equilibration, 0.1 mL (0.0045 mmol, assuming ideal gas behavior) of O_2 was added to the solution while it was still in the temperature controlled gas stream of the spectrometer. The tube was lowered back into the magnetic field and a series of spectra collected. The computed concentration of $V(N[^tBu]Ar)_3$ under these conditions is 0.0305 M, and of $(\eta^2\text{-}O_2)V(N[^tBu]Ar)_3$ is 0.0045 M. Thus the reactions were studied under pseudo-first order conditions with a 7 fold excess $V(N[^tBu]Ar)_3$.

Data showed a smooth decrease in the peak due to $(\eta^2\text{-}O_2)V(N[^tBu]Ar)_3$ at 1.37 ppm and an increase in the peak due to $O\equiv V(N[^tBu]Ar)_3$ at 1.52 ppm. A small amount of ligand is always present in the solution but does not interfere with the measurement. The majority of the sample is paramagnetic $V(N[^tBu]Ar)_3$ which has no resonances in the region between 1 and 2 ppm (see Figure 4.16). Some small bands assigned to unknown decomposition products were observed but they were below 10 % of the reaction product during the start of reaction and were not judged to interfere with the kinetics.

Pseudo-first order rate constants were obtained from plots of $\ln[(\eta^2\text{-}O_2)V(N[^tBu]Ar)_3]$ versus time. Doubling or halving the concentration of $V(N[^tBu]Ar)_3$ did not result in changes outside of the experimental error in the observed rate and

indicated that the rate determining step under conditions of 3–7 fold excess of V(N[^{t}Bu]Ar)$_3$ was conversion of (η^2-O$_2$)V(N[^{t}Bu]Ar)$_3$ to (η^1-O$_2$)V(N[^{t}Bu]Ar)$_3$. Due to difficulties in integration of the paramagnetic solutions, rate constants are considered accurate to 20 %. Representative spectra are shown in Figure 4.13, and a kinetic plot of the data in Figure 4.14. Due to the error associated with NMR integration, the reactions could only be followed for slightly more than one half life. The average values (s^{-1}) were: 0.000081 (0 °C), 0.000165 (10 °C), 0.00056 (22 °C). The data were not judge accurate enough to warrant making an Eyring plot, and the activation energy (Ea) of 14 ± 3 kcal/mol was obtained from the Arrhenius plot shown in Figure 4.15.
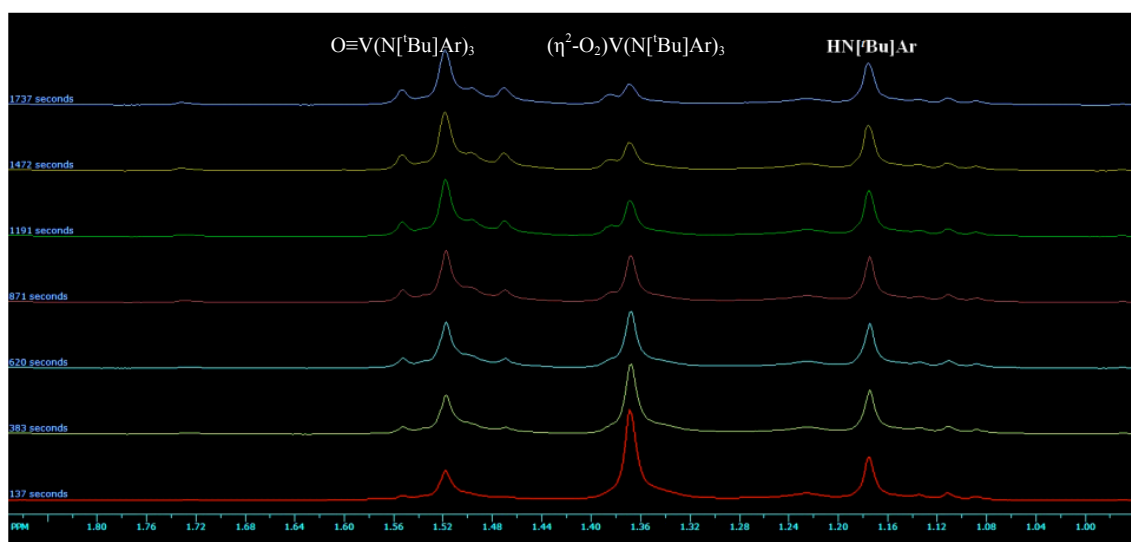
Figure 4.13 Time dependent ^{1}H NMR spectra for reaction: V(N[^{t}Bu]Ar)$_3$ + O$_2$ → (η^2-O$_2$)V(N[^{t}Bu]Ar)$_3$ + V(N[^{t}Bu]Ar)$_3$ → 2 O≡V(N[^{t}Bu]Ar)$_3$ + V(N[^{t}Bu]Ar)$_3$ at 22 °C illustrating the decrease in (η^2-O$_2$)V(N[^{t}Bu]Ar)$_3$ that is coupled with the increase of O≡V(N[^{t}Bu]Ar)$_3$ in the presence of V(N[^{t}Bu]Ar)$_3$.
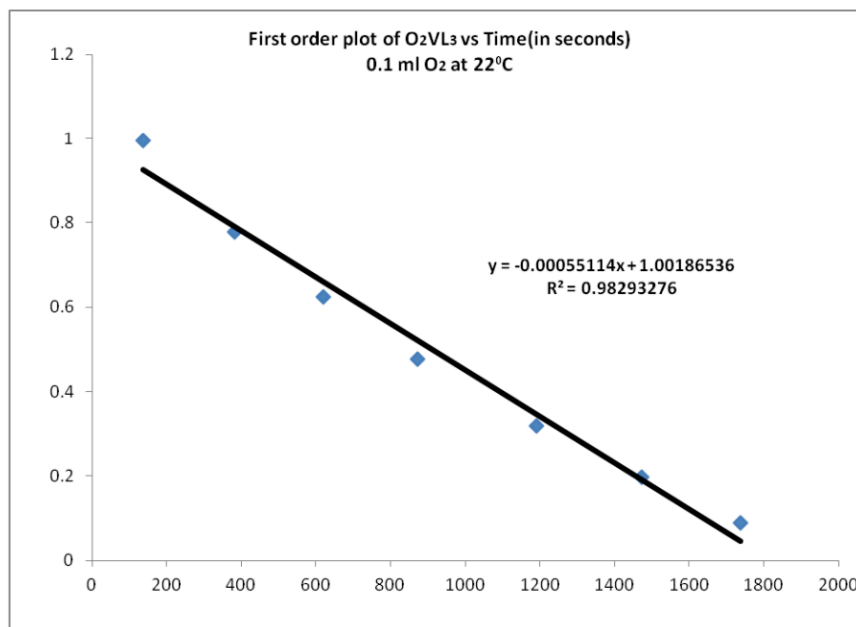
Figure 4.14 Plot for the time dependent reaction in reaction: $V(N[^tBu]Ar)_3 + O_2 \rightarrow (\eta^2\text{-}O_2)V(N[^tBu]Ar)_3 + V(N[^tBu]Ar)_3 \rightarrow 2\ O{\equiv}V(N[^tBu]Ar)_3 + V(N[^tBu]Ar)_3$ at 22 °C according to ^{1}H NMR spectroscopy.
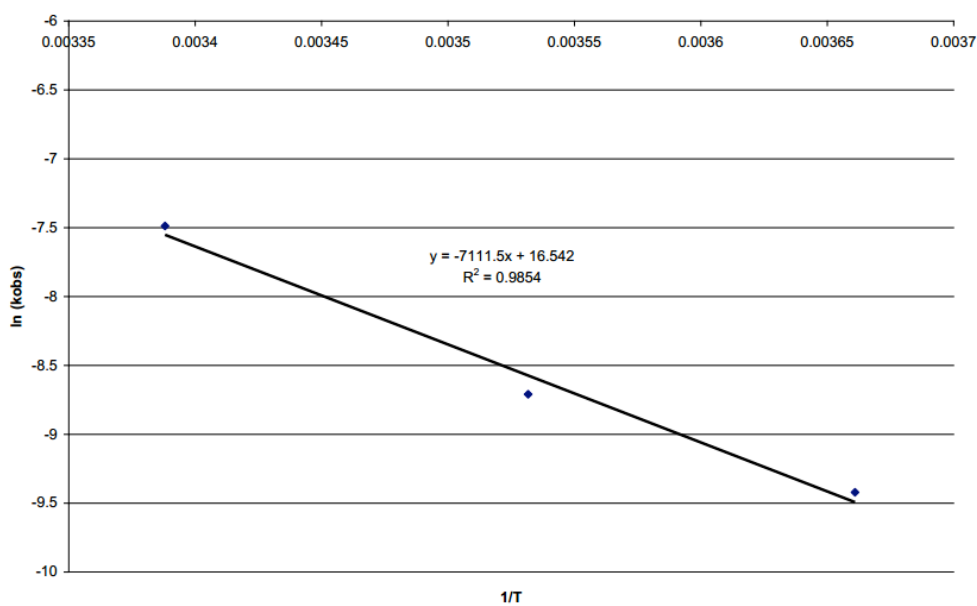
Figure 4.15 Arrhenius plot for data from reaction: $V(N[^tBu]Ar)_3 + O_2 \rightarrow (\eta^2\text{-}O_2)V(N[^tBu]Ar)_3 + V(N[^tBu]Ar)_3 \rightarrow 2\ O{\equiv}V(N[^tBu]Ar)_3 + V(N[^tBu]Ar)_3$ with an Ea of 14 ± 3 kcal/mol.
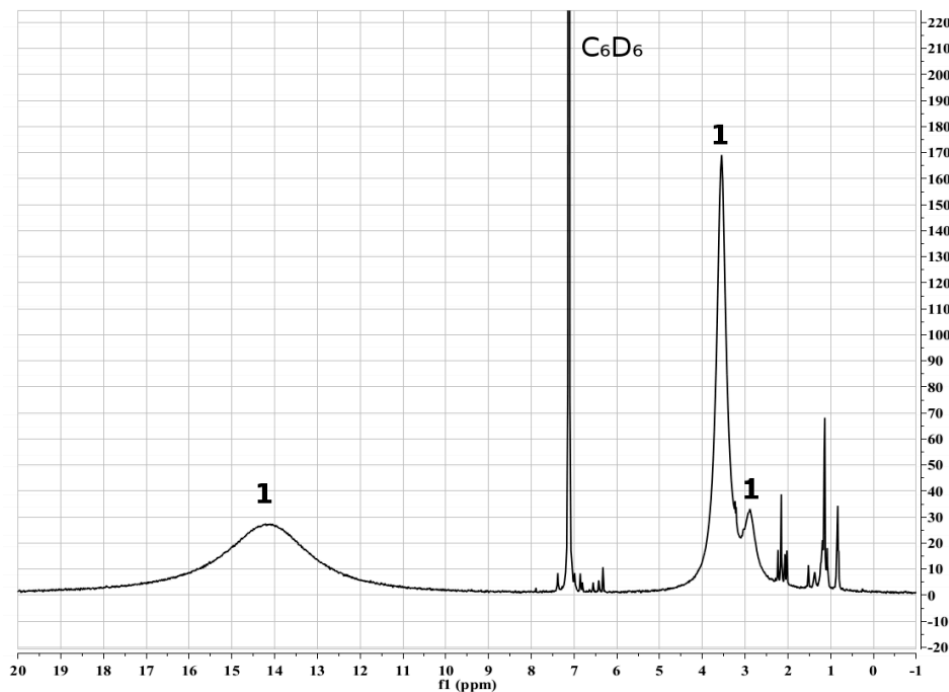
Figure 4.16 ^{1}H NMR spectrum of V(N[^{t}Bu]Ar)$_3$ (**1**) in C$_6$D$_6$.

B. Stopped-Flow Kinetic Measurements

Toluene solutions of complex V(N[^{t}Bu]Ar)$_3$ were prepared in an MBraun glovebox filled with ultra high purity argon (Airgas) and loaded in Hamilton gastight syringes equipped with three way valves. Saturated solutions of ultra high purity O$_2$ (ultra dry grade, Airgas) were prepared by bubbling gas into gastight syringes containing dry toluene for at least 20 minutes; dilutions of the O$_2$ saturated solvent were performed anaerobically to obtain the desired [O$_2$]. The solubility of O$_2$ in toluene was taken as 8.3 mM at 20 °C.[86] Time resolved spectra (λ = 400–800 nm) were acquired over a range of temperatures (−80 to 53 °C) using a Hi-Tech Scientific KinetAsyst SF-61DX2 CryoStopped-Flow system (TgK Scientific Ltd.) equipped with a quartz tungsten halogen light source, a J&M TIDAS diode array detector and a Brandenburg 4479 Series PMT monochromator. The instrument was equipped with stainless steel plumbing lined with PEEK tubing and a 1.00 cm^3 quartz mixing cell submerged in an ethanol cooling bath.

The temperature in the mixing cell was maintained to ± 0.1 °C. Data acquisition was performed using TIDAS-DAQ and/or Kinetic Studio software programs and mixing times were 2–3 ms. All flow lines were washed extensively with Ar-saturated dry toluene prior to loading reactant solutions. All experiments were performed in a single-mixing mode of the instrument with a 1:1 (v/v) mixing ratio. Reactions were studied under pseudo-first order conditions using excess O_2. Data analysis was performed using Kinetic Studio and IGOR Pro 5.0 (Wavemetrics, Inc.) software programs. Kinetic traces at $\lambda =$ 597 nm were fit to a biexponential equation, rate $= -A_1 * \exp(-k_{1obs}t) + -A_2 * \exp(-k_{2obs}t)$ + C, which yielded the observed rate constants (k_{1obs} and k_{2obs}) for η^1-peroxo and η^2-peroxo complex formation, respectively. Only k_{1obs} showed a dependence on $[O_2]$. All observed rate constants reported represent an average of three to seven measurements which gave an acceptable standard deviation (within 5–10%) and all remaining quantities derived from the kinetic data (k, k_2, K_{eq} and activation parameters) are reported with their standard deviations.

C. Calorimetric Measurements

In the glove box 0.1922 g (0.3315 mmol) of $V(N[^tBu]Ar)_3$ was dissolved in 20 mL heptane. The solution was loaded into a 25 mL ampoule with a fragile glass bottom and a threaded fitting containing a stainless steel plunger rod on the top. The ampoule was removed from the glove box and loaded into a modified Guild isoperibol solution calorimeter containing 350 mL of heptane which was saturated and purged with dry O_2 at 10 °C (4.46 mmol, 12.7 mM).[87] Electrical calibrations were performed before and after breaking the ampoule. The ampoule was broken and the enthalpy of reaction recorded during the first 100 seconds of reaction. During that time period, at 10 °C, and in the

absence of excess $V(N[^tBu]Ar)_3$, conversion to $(\eta^2\text{-}O_2)V(N[^tBu]Ar)_3$ is rapid and quantitative and conversion to $O{\equiv}V(N[^tBu]Ar)_3$ is negligible since the $t_{1/2}$ even in the presence of excess trapping $V(N[^tBu]Ar)_3$ is 4200 seconds as described. An average value of 75.4 ± 2.0 kcal/mol was determined.

D. Computational Details

Electronic structure calculations used to obtain thermodynamic values were carried out using the BP86[87,88] pure density functional method as implemented in the Gaussian 09 suite of programs.[89] Structures were optimized using the LANL2DZ[90–92] basis (LANL2DZ ECP and basis for V; the Dunning-Huzinaga D95V[93] basis for all other atoms). Optimizations of several conformers using several anilide environments were carried out to determine the geometry of the global minimum in each case. In order to obtain more reliable molecular structures, the lowest energy minima derived from these calculations were further optimized by including f functions and[94] Stuttgart-Dresden

MDF10[95] fully relativistic effective core potential and basis for V, and the triple-zeta quality basis set, 6-311G(d,p), for all other elements. To derive binding energies, the basis set superposition error (BSSE) was computed using counterpoise calculations.[96,97]

Additional calculations, including frequency calculations and those pertaining to reactivity, were performed using ORCA 2.8 quantum chemistry program package from the development team at the university of Bonn.[98] In all cases the LDA and GGA functionals employed were those of Perdew S33 and Wang (PW-LDA, PW91).[99] In addition, all calculations were carried out using the Zero-Order Regular Approximation (ZORA),[100,101] in conjunction with the SARC-TZV(2pf) basis set for vanadium, the SARC-TZV basis set hydrogen, and SARC-TZV(p) set for all other elements.[102,103]

Spin-restricted Kohn–Sham determinants have been chosen to describe the closed-shell wavefunctions, employing the RI approximation and the tight SCF convergence criteria provided by ORCA. Numerical frequency calculations were performed on the optimized structures. NBO calculations were performed using NBO 5.0.[104-107]

E. Crystallographic Data

Diffraction-quality dark green blocks of (η^2-O$_2$)V(N[^{t}Bu]Ar)$_3$ were grown from pentane at –35 °C, and diffraction quality dark red blocks of ^{t}BuC(=O)N≡V(N[^{t}Bu]Ar)$_3$ were isolated from a pentane solution of ^{t}BuCN·V(N[^{t}Bu]Ar)$_3$ following treatment with O$_2$ at –45.2 °C . The crystals were mounted in Paraton-N oil (Hampton Research) on a MiTeGen MicroMount (Ithaca, NY). Low-temperature data were collected on a Siemens Platform three-circle diffractometer coupled to a Bruker AXS Smart Apex CCD detector with graphitemonochromated Mo/κ radiation (λ = 0.71073 Å), performing ω- and φ-scans. Two domains with minimal overlap were identified in (η^2-O$_2$)V(N[^{t}Bu]Ar)$_3$. The structure solved and refined satisfactorily by integrating only the main domain The two domains in the crystal of ^{t}BuC(=O)N≡V(N[^{t}Bu]Ar)$_3$ were identified using CELL_NOW.[108] Both structures were solved by direct methods using SHELXS and refined against F^2 on all data by full-matrix least squares with SHELXL-97.[109] A semi-empirical absorption correction (SADABS or TWINABS) were applied to the diffraction data.[110,111] All non hydrogen atoms were refined anisotropically. All hydrogen atoms were included in the model at geometrically calculated positions and refined using a riding model. The isotropic displacement parameters of all hydrogen atoms were fixed to 1.2 times the U value of the atoms they are linked to (1.5 times for methyl groups). Compound (η^2-O$_2$)V(N[^{t}Bu]Ar)$_3$ crystallizes in the cubic I-43d space group with one

third of a molecule in the asymmetric unit. This enforces disorder of the peroxo ligand over three positions. The occupancy of the O atoms was allowed to refined freely to allow for the possibility of cocrystallization with O≡V(N[^{t}Bu]Ar)$_3$. The ^{t}Bu group was modeled as disordered over two positions (71.9%). Compound ^{t}BuC(=O)N≡V(N[^{t}Bu]Ar)$_3$ crystallizes in P2$_1$2$_1$2$_1$ with one molecule in the asymmetric unit. Two domains were identified using CELL_NOW and the data was reduced using TWINABS. The final data was refined against the HKLF4 data giving a minor component of 43.3%.

Table 4.1 Crystallographic and refinement parameters for (η^2-O$_2$)V(N[^{t}Bu]Ar)$_3$ (**3**) and ^{t}BuC(=O)N≡V(N[^{t}Bu]Ar)$_3$ (**5**).

	3	5
Empirical formula	C$_{36}$H$_{54}$N$_3$O$_2$V	C$_{41}$H$_{63}$N$_4$OV
Formula weight	611.76	678.89
Temperature (K)	100(2)	100(2)
Wavelength (Å)	0.71073	0.71073
Crystal system	Cubic	Orthorhombic
Space group	I-43d	P2$_1$2$_1$2$_1$
a (Å), α (deg)	23.919(2), 90	9.872(2), 90
b (Å), β (deg)	23.919(2), 90	19.708(4), 90
c (Å), γ (deg)	23.919(2), 90	19.941(4), 90
V (Å^3)	13685(2)	3880(1)
Z	16	4
ρ_{calc} (g·cm^{-3})	1.188	1.162
μ (mm^{-1})	0.324	0.291
F(000)	5280	1436
Crystal size (mm^3)	0.20 × 0.20 × 0.10	0.20 × 0.20 × 0.20
θ range (deg)	2.09 to 30.02	1.45 to 30.03

Index ranges	$-33 \leq h \leq 33$	$0 \leq h \leq 13$
	$-33 \leq k \leq 33$	$0 \leq k \leq 27$
	$-33 \leq l \leq 33$	$0 \leq l \leq 28$
Reflections collected	151622	6268
Independent reflections	3356 [R_{int} = 0.0690]	6268 [R_{int} = 0.0000][a]
Completeness to θ_{max} (%)	100.0	100.0
Absorption correction	Semi-empirical from equivalents	Semi-empirical from equivalents
Max. and min. transmission	0.9683 and 0.9380	0.9441 and 0.9441
Refinement method	Full-matrix least-squares on F^2	Full-matrix least-squares on F^2
Data / restraints / parameters	3356 / 118 / 183	6268 / 0 / 443
Goodness-of-fit on F^2	1.091	1.078
Final R indices [I>2sigma(I)][b]	R_1 = 0.0319, wR_2 = 0.0772	R_1 = 0.0633, wR_2 = 0.1143
R indices (all data)[b]	R_1 = 0.0386, wR_2 = 0.0826	R_1 = 0.0799, wR_2 = 0.1211
Absolute structure parameter	-0.01(2)	0.53(3)
Largest diff. peak and hole (e·Å^{-3})	0.200 and -0.269	0.349 and -0.380

[a] Statistics reflect the fact that the values are merged in TWINABS. An approximate R(int) from merging in TWINABS is 0.0622.

[b] $R_1 = \sum ||F_o| - |F_c||/\sum |F_o|$; $wR = \{\sum[w(F_o^2 - F_c^2)^2]/\sum w(F_o^2)^2\}^{1/2}$

Chapter 5: Oxygen Atom Transfer from Mesityl Nitrile Oxide to Metals and Non-Metals

5.1   Background

In previous chapters we investigated binding of O_2 to metal complexes. In the oxygenase pathway, metal-oxo complexes of general formula $O=ML_n$ are generated from O_2, but other sources can also be used in generation of $O=ML_n$ in particular where a single O atom is transferred. This chapter reports our studies of Oxygen Atom Transfer (OAT) based on the reactive OAT donor MesCNO.

OAT is a fundamental step in biochemical and industrial oxidative reactions.[112] Selective catalytic oxidation of substrates is at the heart of development of many environmentally benign processes,[113] and understanding the detailed mechanisms of OAT reactions will help in design of such catalysts. Nitrous oxide is of interest as a green oxidant both because the byproduct of its oxidations is the innocuous N_2 molecule, and because it is a thermodynamically powerful oxidant ($D_e(N-O)$ ca. 40 kcal mol^{-1}).[114] A reality to be dealt with in harnessing N_2O for oxidation chemistry is that it exhibits low reactivity and often can be regarded as essentially an inert gas.[115] Nitrous oxide oxidations may in principle be catalyzed, in furtherance of which coordination complexes of this small molecule have been studied.[116] Recently, an example of such a complex has been characterized in the solid state by X-ray crystallography.[117] A new approach to N_2O chemistry has also emerged in the form of its capture by frustrated Lewis pair (FLP) systems.[118]

Another common class of compounds frequently used in OAT processes is the amine-N-oxides. Here as well, transition metal based catalysis of non-metal oxidations is

often required since a number of thermodynamically favorable oxygen atom transfer reactions occur at prohibitively slow rates at room temperature. An example is transfer of an O atom from pyridine-*N*-oxide (PyO) to a phosphine as shown in Eqn. (5.1).

$$\tag{5.1}$$
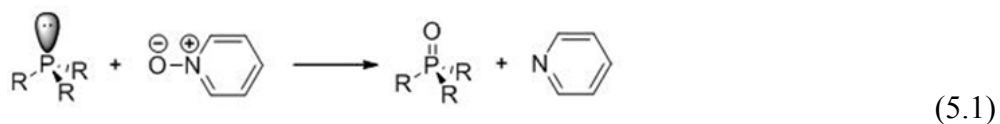
In spite of being exothermic by over 70 kcal mol^{-1} due to the strong P=O bond formed, reaction 5.1 does not occur readily since there is no low energy path available. A simple explanation is that lone pair/lone pair repulsion yields a high energy transition state for this very favorable reaction. This highlights the role kinetic barriers play in oxidative chemistry.[119] Transition metal based catalytic systems have been developed[120] to lower this barrier by the two general steps shown in Eqn. (5.2) and (5.3) which may be representative of a wide range of enzymatic biochemical and catalytic industrial oxidations.

$$\tag{5.2}$$

$$\tag{5.3}$$
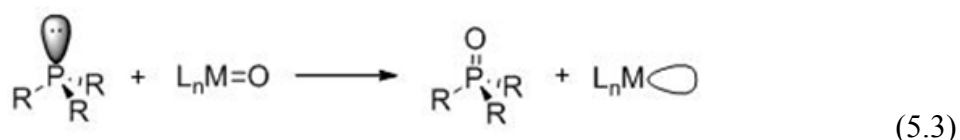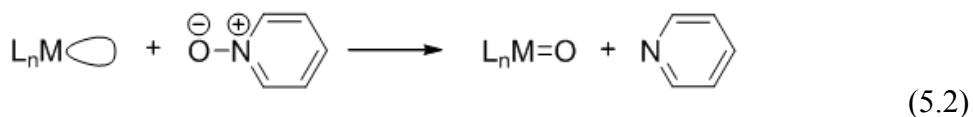
The step in Eqn. (5.2) involves OAT from the oxidant to the metal complex. Espenson and coworkers have recently shown that this requires a vacant coordination site at the metal center to be oxidized.[121] The step in Eqn. (5.3) involves OAT from the metal oxide to the substrate. Hall has postulated that this involves attack of the lone pair of the phosphine on an M=O π* orbital.[122] An alternative mechanism involving coupled electron transfer/atom transfer has also been proposed for some OAT steps.[123] The factors

controlling the kinetics of reactions 5.2 and 5.3 remain an area of great activity. These two steps serve to bracket the M–O bond strength available for a potential catalyst. Ideally this should be stronger than N–O in PyO but weaker than the P=O bond in R_3PO. Holm and coworkers have highlighted the importance of a thermodynamic scale for OAT.[124]

Less well appreciated than N_2O and amine-N-oxides for OAT reactivity is the class of molecules known as nitrile oxides, RCNO.[125] Like nitrous oxide, the 1,3-dipolar nitrile oxide functional group contains a linear triatomic sequence with a terminal oxygen atom bonded to an sp hybridized nitrogen atom. The dative[126] N→O bond distances in substituted benzonitrile oxides are for example 1.249(7) and 1.237(10) Å, these being shorter than corresponding distances for trimethylamine-N-oxide 1.388 Å or pyridine-N-oxide derivatives (1.28-1.30 Å),[127] while longer than that (1.184 Å) in nitrous oxide.[128] The N–O BDE in MesCNO is only 52.3 kcal mol^{-1}, compared to a value of 63.3 kcal mol^{-1} for the N–O BDE in PyO.[129] This makes it a potent OAT reagent thermodynamically, even more so than molecular oxygen itself as implied by the energetics of Eqn 5.4.[130]

$$2\ \text{MesCNO} \longrightarrow 2\ \text{MesCN} + O_2 \qquad \Delta H = -14.5\ \text{kcal mol}^{-1}$$

(5.4)
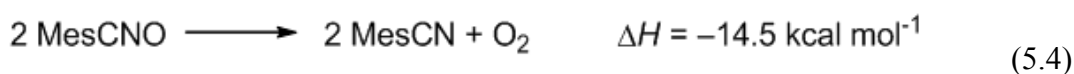
The endothermic nature of O_2 addition to MesCN suggests that this reagent may be of value for "difficult" oxidations. Indeed unlike both N_2O and amine-N-oxides, nitrile oxides are known to effect the oxidation of tertiary phosphines within minutes upon mixing in solution at room temperature according to Eqn. (5.5).[131] The reasons why Eqn. (5.1) requires a catalyst and Eqn. (5.5) does not have not been delineated.

$$R-\overset{\cdot\cdot}{\underset{R}{P}}{}'R + Mes-C\equiv\overset{\oplus}{N}-\overset{\ominus}{O} \longrightarrow R-\overset{\overset{O}{\|}}{\underset{R}{P}}{}'R + Mes-C\equiv N$$

$$(5.5)$$
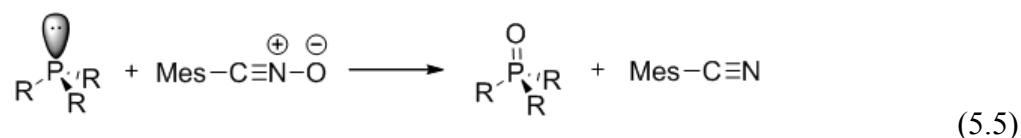
Furthermore, for conversion of the terminal phosphide complex $(Ar['Bu]N)_3MoP$ to its oxide, $(Ar['Bu]N)_3MoPO$, the harsh oxidant dimethyl dioxirane (DMDO) was required, as both N_2O and amine-N-oxides failed to react.[132] As described in this report, MesCNO smoothly effects OAT to $(Ar['Bu]N)_3MoP$, suggesting that this reagent class ought to be considered more generally for OAT processes. In this regard, Beck and coworkers have reported the oxidation of coordinated phosphines by stable nitrile oxides as shown in Eqn. (5.6).[133] $Fe(CO)_5$ is capable of deoxygenating nitrile oxides to nitriles in moderate yields.[134]

$$Pt(PPh_3)_3 + 2\,RCNO \longrightarrow Ph-\overset{\overset{PPh_3}{|}}{\underset{P(O)Ph_2}{Pt}}-NCR + RCN + Ph_3PO$$

$$(5.6)$$
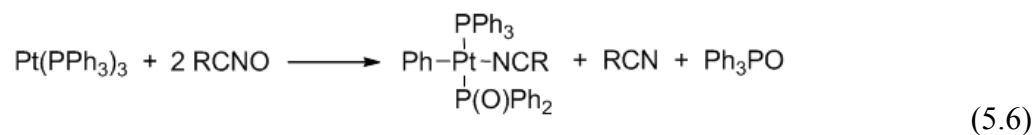
In spite of these attractive results we have found only limited use of MesCNO in literature reports of OAT reactions. A characteristic organic reaction of nitrile oxides is 1,3-cycloaddition.[135] Likewise, the use of nitrile oxides in cycloaddition reactions of organometallic complexes is well documented.[136]

The work reported here began with an interest in simply utilizing MesCNO as an oxidant in calorimetric studies, first for R_3P to calibrate it for work in solution calorimetry, and then for $(Ar['Bu]N)_3MoP$ (Ar = $3,5-C_6H_3Me_2$) to generate data on the Mo–P and P–O bond strengths in the known unique terminal phosphorous monoxide complex $(Ar['Bu]N)_3MoPO$.[132] This work extends earlier thermodynamic and kinetic studies of chalcogen atom transfer for E = S, Se, and Te (but not O) for R_3P, NHC (NHC

= N-heterocyclic carbene), $(Ar[^tBu]N)_3MoP$ and $(Ar[^tBu]N)_3Mo$.[137] In the studies of sulfur atom transfer (SAT) to NHCs, Ph_3SbS was utilized as a useful single S atom transfer reagent to NHCs as shown in Eqn. (5.7).

$$Ph_3SbS + SIPr \longrightarrow Ph_3Sb + SIPr=S \qquad (5.7)$$
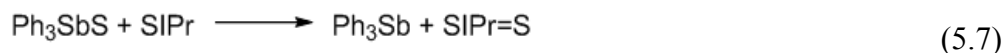
It was hoped in the current work to extend this to the OAT by using MesCNO as a single O atom transfer reagent for NHCs as shown in Eqn. (5.8).

$$MesCNO + SIPr \overset{}{\longrightarrow\!\!\!\times\!\!\!\!\!} MesCN + SIPr=O \qquad (5.8)$$

To our surprise, full oxidation as shown in Eqn. (5.8) did not occur. The potential oxidation of the NHC to a cyclic urea stopped at simple adduct formation and we were able to isolate and structurally characterize the blue SIPr·MesCNO complex in which the lone pair of electrons of SIPr binds to the electropositive C atom of MesCNO. NHCs ligands such as SIPr strongly resemble R_3P ligands in their bonding to both metal and non-metal acids.[138] Isolation of the SIPr·MesCNO adduct led us to postulate that the observed kinetic OAT facility of MesCNO to phosphines might be conferred by initial attack of R_3P at the MesCNO nitrile carbon atom to form an adduct related to that observed in SIPr·MesCNO. That hypothesis was confirmed by detailed computational studies of the reaction profile which are also reported here.

The primary focus of the current work is the energetics and mechanism of oxidation of non-metals by MesCNO. Limited preliminary results on reactions of transition metal complexes with MesCNO are reported here to confirm mechanistic ideas regarding these non-metal reactions. Detailed kinetic and thermodynamic studies of metal complex oxidations by MesCNO will be reported separately.[139]

5.2   Results

Reaction of MesCNO and (Ar[^{t}Bu]N)$_3$MoP. The initial target of this work was improved synthesis and determination of the thermochemistry of the previously characterized purple-blue complex (Ar[^{t}Bu]N)$_3$MoPO.[132] Attempted preparation from PyO as shown in Eqn. (5.9) did not occur at room temperature in toluene solution, which is in keeping with the known inability of PyO to oxidize phosphines.

$$(Ar[^tBu]N)_3MoP + PyO \xrightarrow{\quad\times\quad} (Ar[^tBu]N)_3MoPO + Py$$

$$(5.9)$$
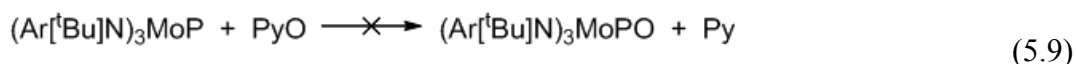
In contrast, reaction of MesCNO with the bright yellow complex (Ar[^{t}Bu]N)$_3$MoP was found to occur rapidly in toluene solution to yield purple (Ar[^{t}Bu]N)$_3$MoPO and MesCN in quantitative yield as determined by NMR spectroscopy and shown in Eqn (5.10).

$$(Ar[^tBu]N)_3MoP + MesCNO \longrightarrow (Ar[^tBu]N)_3MoPO + MesCN$$

$$(5.10)$$
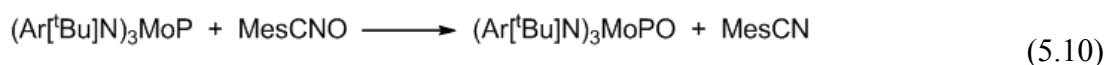
Previous preparation of (Ar[^{t}Bu]N)$_3$MoPO involved reaction with dimethyldioxirane at −78 ^{o}C. The pathway in Eqn. (5.10) provides a more convenient method for *in situ* generation of (Ar[^{t}Bu]N)$_3$MoPO and basis for further exploration of its reactivity.[132b]

Thermochemistry of OAT from MesCNO to (Ar[^{t}Bu]N)$_3$MoP or R$_3$P. Solution calorimetric measurements of Eqn. (5.4) and (5.10) were performed in toluene solution at 30 °C using Calvet calorimetry with solid mesityl nitrile oxide as limiting reagent. Values for the enthalpies of reaction with all species in toluene solution are collected in Table 1 together with bond strength estimates and earlier reported data for sulfur atom transfer (SAT).[137] Data on the BDE in toluene solution are considered accurate to ± 3 kcal•mol^{-1}.

Table 5.1 Enthalpies of reaction of MesCNO and A_nP in toluene solution and derived P=O BDE data in kcal mol^{-1}. For comparison purposes previously reported P=S data[137] are also included.

A_nP	ΔH	P=O BDE	P=S BDE
(Ar[^{t}Bu]N)$_3$MoP	-56.6 ± 0.8	108.9	78
Ph$_3$P	-79.9 ± 1.7	132.2	88
Cy$_3$P	-85.3 ± 1.8	137.6	98
Me$_3$P	-86.2 ± 1.7	138.5	94

Reaction of MesCNO and Pd(IPr)(P-*p*-tolyl$_3$). MesCNO was found to react slowly with the bright yellow-orange complex Pd(IPr)(P-*p*-tolyl$_3$), yielding a cyclic Pd(II) complex (Figure 5.1) and tritolylphosphine oxide (Eqn. (5.11)). It resembles the reported reaction of stable nitrile oxides with Pt(PPh$_3$)$_4$ resulting in oxidation of coordinated phosphines (Eqn. (5.6)). More detailed study of the mechanism of formation of this unique Pd(II) complex is planned.
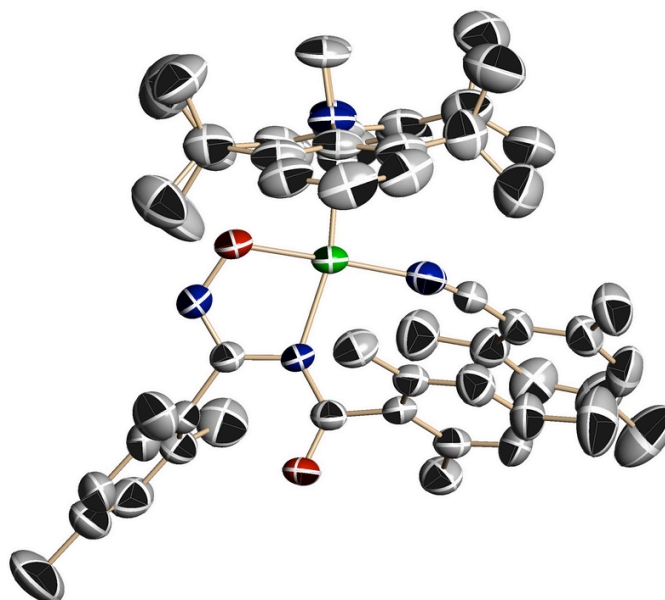
Figure 5.1 ORTEP diagram of Pd^{II}(IPr)(ONCMes)(NC(O)Mes)(NCMes).

(5.11)
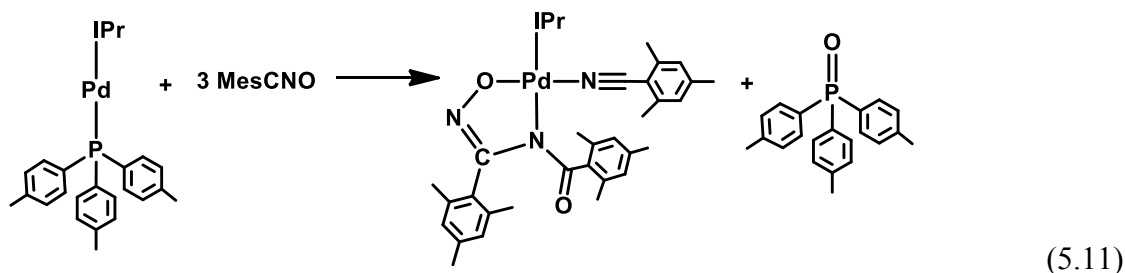
Computational Data on X–O Bond Dissociation Enthalpies. The X–O bond dissociation enthalpy of several species was calculated according to the procedure described by Lee and Holm[140] computing the enthalpy of reaction with molecular oxygen for several X/XO couples as shown in Scheme 5.1 (reaction ii.). The X–O bond dissociation enthalpy corresponding to reaction i. in Scheme 5.1 was then derived as $BDE = -\Delta H_{X/XO} + \Delta H^0{}_m(O(g))$, where $\Delta H^0{}_m(O(g)) = 59.55$ kcal mol^{-1}.[141]
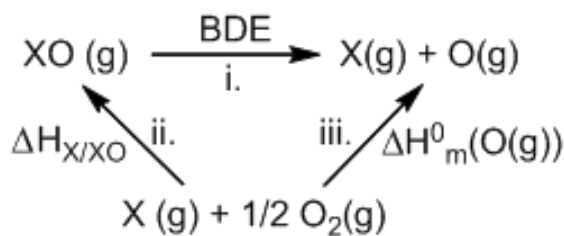
Scheme 5.1 Thermodynamic cycle used to obtain computationally the BDE.

Computed X–O bond dissociation enthalpies performed at the M05-2X/6-311G(3df,2p) and G3 level, together with experimental values, are collected in Table 5.2. G3 theory is known for delivering chemical accuracy, however its high computational cost most often give preference to the less computationally demanding DFT methods. Cundari and coworkers[142] have shown that the G3 method performs within the experimental error in calculating the thermochemistry of OAT reactions, while DFT methods such as the popular B3LYP functional provided inadequate results. As can be seen in Table 5.2, a good agreement between experimental data and calculated values at the M05-2X/6-311G(3df,2p) level is obtained for all the species studied. For the smallest

molecules where the G3 methodology is applicable, similar results are obtained at the M05-2X/6-311G(3df,2p) level. Calculated values using the B3LYP functional give worse results as previously shown by Cundari and coworkers[142] giving the worst agreement with the experimental (or G3-calculated) data with the phosphines.

Table 5.2 Bond dissociation enthalpies (BDEs) in kcal mol^{-1} for the reaction $XO(g) \rightarrow X(g) + O(g)$ computed at the M05-2X/6-311G(3df,2p) and G3 levels, and compared to experimental data. $BDE_{calc} - BDE_{exp}$ is shown in brackets beside the computed values.

X	M05-2X/6-311G(3df,2p)	G3	Experimental[a]
NN	38.0 [−2.0]	40.8 [0.8]	40.0
PhCN	48.5	50.0	---
MesCN	48.1 [−4.2]	48.8 [−3.5]	52.3[b]
Py[c]	61.7 [−1.6]	63.6 [0.3]	63.3
NP	74.6	78.3	---
THT[d]	82.1	84.8	---
Me$_2$S	88.3 [1.7]	86.0 [−0.6]	86.6
PP	90.1	90.1	---
(Ar[^{t}Bu]N)$_3$MoP	105.9 [−3.0][e]	---	108.9[f]
CO	128.2 [1.0]	128.7 [1.5]	127.2
Ph$_3$P	130.2 [−2.0]	---	132.2[f]
Cy$_3$P	135.3 [−2.3]	---	137.6[f]
Me$_3$P	133.0 [−5.5]	134.9 [−3.6]	138.5[f]
SIPr	151.5	---	---

[a] Unless stated otherwise, values taken from reference 130; [b] value taken from reference 129; [c] pyridine; [d] tetrahydrothiophene; [e] using the Stuttgart-Dresden MWB28[31] effective core potential and basis including a set of additional f functions for Mo and the 6-311G(d,p) basis set for all other elements; [f] this work.

Synthesis and Structure of SIPr·MesCNO. As discussed earlier, we initially studied reaction of SIPr and MesCNO in hopes of using this as an entry to measure enthalpies of OAT to NHC ligands forming cyclic ureas as shown in Eqn. (5.8). OAT did

not occur in spite of being thermochemically highly favorable (see Table 5.2), but simple

binding of the SIPr to MesCNO as shown in Eqn. (5.12). The crystal structure of the

adduct shows binding between the lone pair of electrons of the NHC at the electrophilic

C atom of MesCNO as shown in Figure 5.2.

$$(5.12)$$
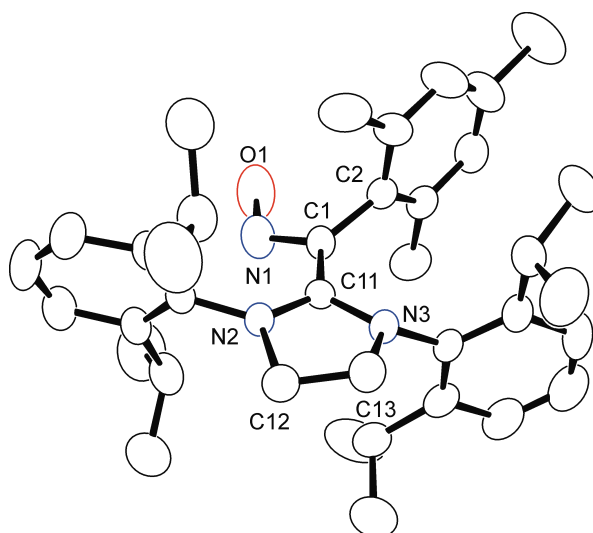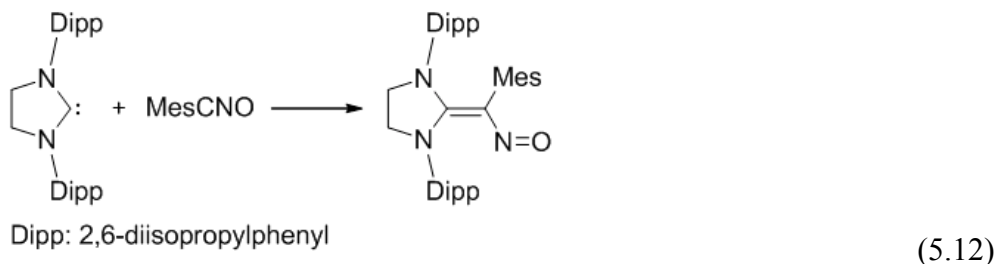
Figure 5.2 ORTEP diagram (40% probability) of the SIPr·MesCNO adduct. Selected distances (Å) and angles (°): C1–C8, 1.521(4); C8–N2, 1.326(2); C10–N2, 1.451(2); N1–C1–C8–N2, 84.6. Complete structural data is available in supporting information.

This mode of binding resembles that to CS_2 which is displayed for both NHC and

R_3P ligands.[138a] Loui and coworkers[138b] have even reported adducts between CO_2 and

NHCs. Based on the analogous Lewis basicity of NHCs and R_3P compounds, the

isolation and characterization of the adduct shown in Figure 5.2 suggested that attack of

R_3P at MesCNO might also proceed by initial attack at the C atom rather than the O atom

and that this was the explanation of why it, and not PyO is an efficient OAT reagent for phosphines. This prompted kinetic and computational study of the reaction mechanism of phosphines and MesCNO. Detailed synthetic and computational study of the adducts between a range of NHCs and MesCNO are in progress.[143]

UV-vis Kinetic Study of Reaction of MesCNO with (Ar[^{t}Bu]N)$_3$MoP. Kinetic analysis of the reaction of MesCNO with (Ar[^{t}Bu]N)$_3$MoP was performed on a UV-vis spectrophotometer under pseudo first order conditions with large excess of MesCNO in both CH_2Cl_2 and toluene solution. Time-resolved spectra show the appearance and growth of the peak at 550 nm that corresponds to the absorbance of independently prepared (Ar[^{t}Bu]N)$_3$MoPO. The exponential growth of this peak was used for kinetic analysis. Kinetic traces were fit to a single exponential function and rate constants were obtained, $k_{obs} = k_1$[MesCNO] (Figure 5.3).
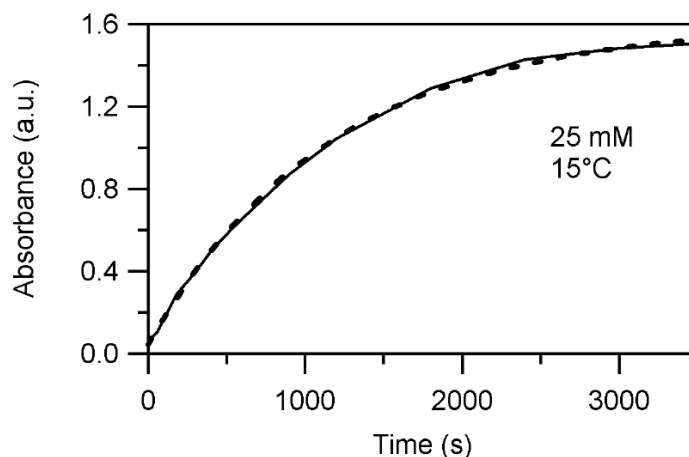
Figure 5.3 First-order fit of data of 25 mM MesCNO at 15 °C in CH_2Cl_2 with ([(Ar[^{t}Bu]N)$_3$MoP] = 0.6mM).

Under high concentrations of MesCNO (100 mM), complete formation of (Ar[^{t}Bu]N)$_3$MoPO was followed by its slow partial decomposition, which could be seen as a minor decrease in the intensity of the peak at 550 nm and a slow appearance of a

shoulder at 440 nm over longer periods of time (3-4 hours, Figure 5.4). The minor decomposition was judged to not compromise kinetic analysis of the $(Ar[^tBu]N)_3MoPO$ formation step. The identity of the decomposition products was not established. Plots of k_{obs} versus [MesCNO] gave straight lines as shown in Figure 5.5, and were used to derive second-order rate constants in CH_2Cl_2: $k_{15\,°C} = 0.11\ M^{-1}s^{-1}$; $k_{22\,°C} = 0.15\ M^{-1}s^{-1}$; $k_{30\,°C} = 0.20\ M^{-1}s^{-1}$.
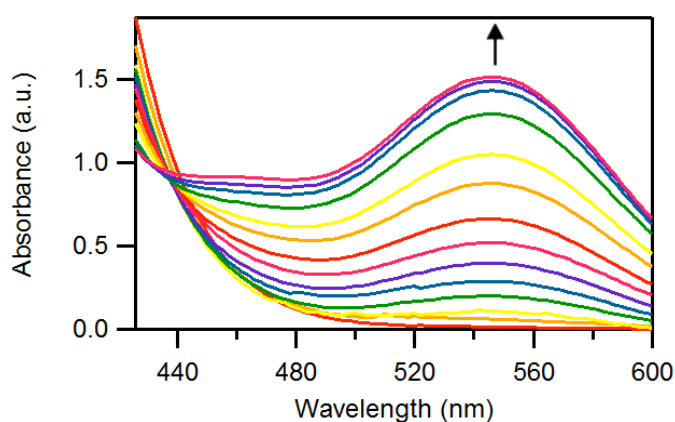
Figure 5.4 UV-vis spectrum of reaction of MesCNO with $(Ar[^tBu]N)_3MoP$. Spectral data as a function of time taken at 15 °C in CH_2Cl_2 with 25 mM MesCNO ($[(Ar[^tBu]N)_3MoP]$ = 0.6 mM), over a time interval of 60 min showing the rise in the band at 550 nm due to increase in $[(Ar[^tBu]N)_3MoPO]$.
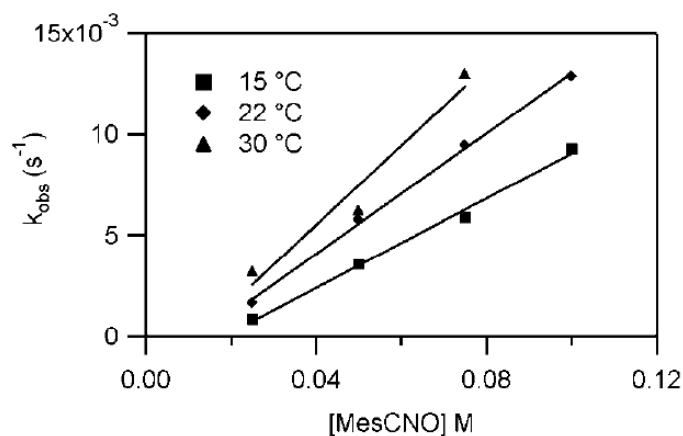
Figure 5.5 Plot of kobs, versus the [MesCNO] at 15, 22, and 30 °C used to calculate second order rate constants for OAT to ($[(Ar[tBu]N)_3MoP]$ in CH_2Cl_2.

Identical kinetic experiments were repeated in toluene solution. Reaction rate as a function of temperature was measured with [MesCNO] = 50 mM and [(Ar[^{t}Bu]N)$_3$MoP] = 0.6 mM at five different temperatures: 15, 22, 30, 38 and 45 °C. In the replicate experiments for the same temperature in each solvent, k_{obs} in CH$_2$Cl$_2$ and toluene were found to be similar. An Eyring plot was generated for the temperature dependence study in toluene solution and activation parameters were calculated (Figure 5.6). The graphical analysis provided $\Delta H^{\ddagger} = 11$ kcal/mol and $\Delta S^{\ddagger} = -27$ cal/mol K.
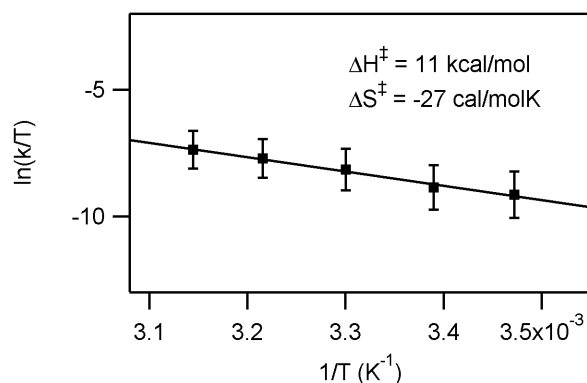
Figure 5.6 Eyring plot for reaction between MesCNO and (Ar[^{t}Bu]N)$_3$MoP in toluene.

FTIR Kinetic Studies of Reaction of MesCNO with R$_3$P, (Ar[^{t}Bu]N)$_3$MoP and SIPr.
In order to compare the rates of oxidation of tertiary phosphines to that of (Ar[^{t}Bu]N)$_3$MoP, it was necessary to use vibrational spectroscopy since there is no observable color change when the phosphines are oxidized to the phosphine oxides since both are colorless. In addition, discovery of binding of SIPr to MesCNO was investigated kinetically for purposes of comparison of simple binding of the NHC to binding plus OAT which occurs for the phosphines and phosphide substrates. Reactions were run in a thermostatted FTIR cell under argon atmosphere at a balanced 1:1 ratio of [MesCNO]:[R$_3$P]. As a check, the kinetics of (Ar[^{t}Bu]N)$_3$MoP oxidation was also investigated by FTIR in toluene. A typical difference plot for oxidation of

$(Ar[^tBu]N)_3MoP$ by MesCNO is shown in Figure 5.7 and the linear second order plot derived from it in Figure 5.8.
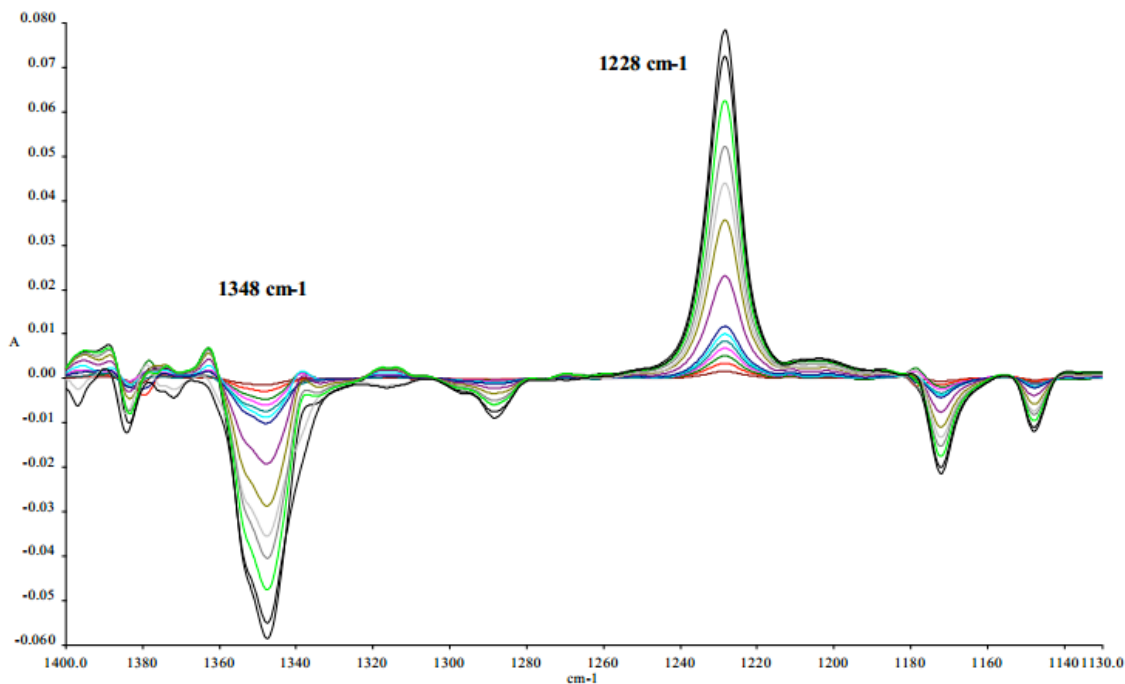
Figure 5.7 FTIR spectroscopic data for reaction of $(Ar[^tBu]N)_3MoP$ and MesCNO in toluene at 4 ^{o}C showing the decrease in the band due to ONCMes at 1348 cm^{-1} and increase in the band due to $(Ar[^tBu]N)_3MoPO$ at 1228 cm^{-1}.
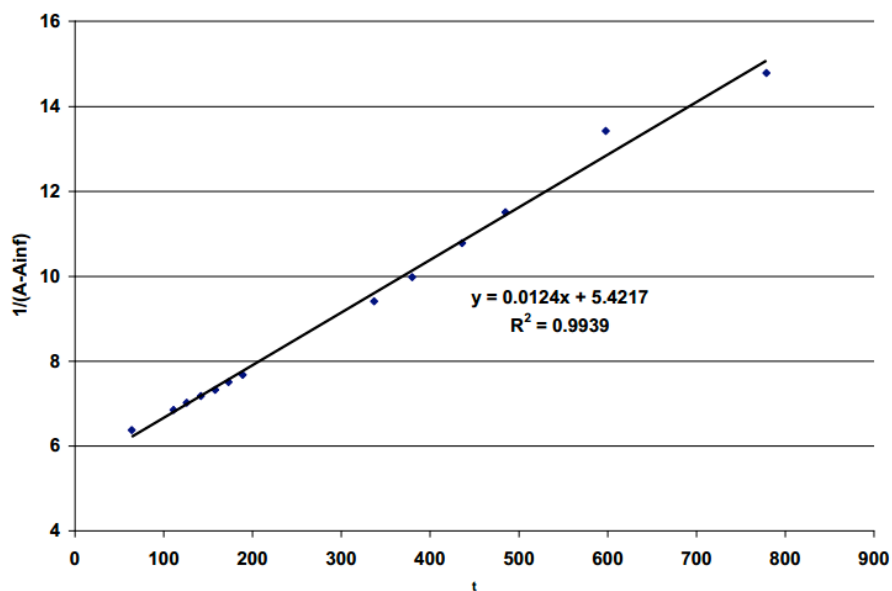
Figure 5.8 Second order plot of the spectroscopic data in Figure 5.7 for reaction of $(Ar[^tBu]N)_3MoP$ and ONCMes in toluene at 4 ^{o}C.

Attempts to detect intermediates in these reactions were not successful. Even at −40 °C, FTIR spectral data for the reaction of Cy$_3$P and MesCNO displayed isosbestic points and the rate of decay of MesCNO and the rate of buildup of Cy$_3$PO were equal and opposite in sign. Eyring plots are shown in Figure 5.9, rate constants and activation parameters are shown in Table 5.3.
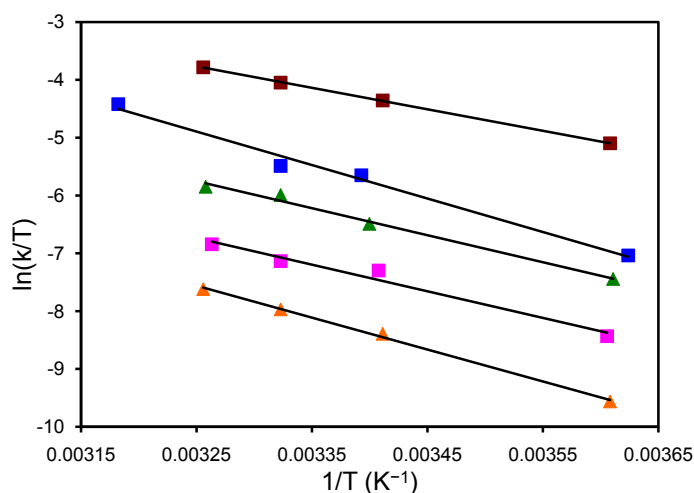
Figure 5.9 Eyring plots for reaction of MesCNO and SIPr (top line, brown square); Me$_3$P (second line, blue squares), Cy$_3$P (third line, green triangles), (*p*-tolyl)$_3$P (fourth line, pink square) and (Ar[^{t}Bu]N)$_3$MoP (bottom line, orange triangles).

Table 5.3 Rate constants at ≈ 20 °C and derived activation parameters as well as reaction enthalpies for interaction between X and MesCNO.

X	k(M^{-1}s^{-1})	$\Delta H^{\ddagger}$(kcal mol^{-1})	$\Delta S^{\ddagger}$(cal mol^{-1}K^{-1})	ΔH^{0}(kcal mol^{-1})
Me$_3$P	1.0	11.5	−19.5	−86.2
Cy$_3$P	0.45	9.3	−28.4	−85.3
(*p*-tolyl)$_3$P	0.20	9.1	−30.9	−79.9[a]
(Ar[^{t}Bu]N)$_3$MoP[b]	0.07	11.0	−26.6	−56.6
(Ar[^{t}Bu]N)$_3$MoP[c]	0.04	11.0	-27.0	−56.6

SIPR	3.8	7.4	−30.7

[a] Refers to reaction of Ph$_3$P, expected to be similar to (*p*-tolyl)$_3$P; [b] values obtained by FTIR spectroscopy; [c] values obtained by UV-vis spectrophotometry.

The entropies of activation are near −25 cal mol^{-1}K^{-1} in keeping with an associative transition state. The least unfavorable entropy of activation occurs, as might be expected, for Me$_3$P since it is sterically the least hindered. The enthalpies of activation are in the range $\Delta H^{\ddagger} = 10 \pm 2$ kcal mol^{-1}, except for SIPr which involves only binding and not oxidative addition. The data determined by FTIR kinetics for (Ar[^{t}Bu]N)$_3$MoP are in good agreement with those determined independently by UV-vis studies. The rate and activation parameters in Table 5.3 appear in keeping with a common mechanism to these reactions.

Theoretical Mechanism for Reaction of PhCNO and Me$_3$P. Experimental work described above prompted theoretical investigation of OAT between Me$_3$P and PhCNO as a model system. The reason OAT does not occur in the SIPr·MesCNO adduct is under computational study as part of a more detailed investigation of these adducts.[143] The frontier orbitals for Me$_3$P and PhCNO calculated at the M05-2X/6-311G(3df,2p) level are shown in Figure 5.10. The shape of the orbitals suggests that a probable reaction pathway would involve attack of the HOMO of Me$_3$P, which is essentially a lone pair orbital (C on Figure 5.10), to the LUMO of PhCNO (B on Figure 5.10), which is a delocalized π* orbital with a significant lobe on the C atom of PhCNO.
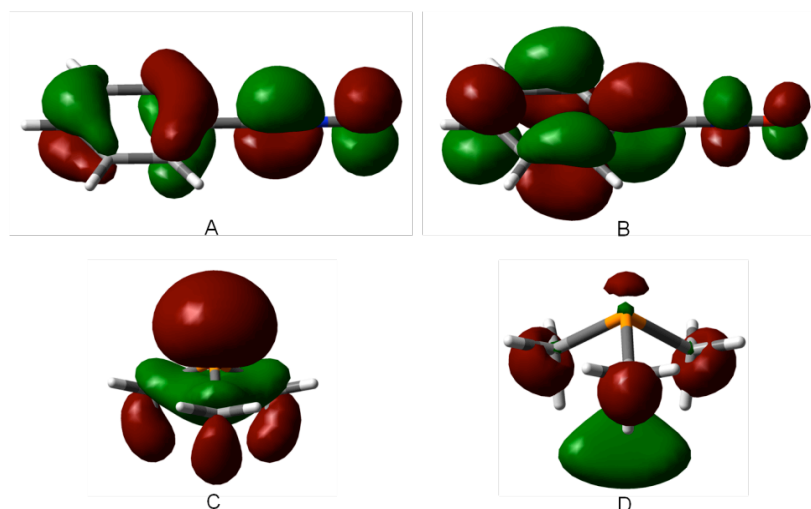
Figure 5.10 Computed frontier orbitals for Me₃P and PhCNO. A) HOMO of PhCNO; B) LUMO of PhCNO; C) HOMO of Me₃P; D) LUMO of Me₃P.

This is confirmed in the reaction mechanism obtained by computing the intrinsic reaction coordinate (IRC) at the same level of theory which is shown in Figure 5.11. The mechanism is composed of three consecutive stages, where three transition states have to be overcome, the first one assigned as the rate-limiting step. The structures of the computed transition states and intermediates are shown in Figure 5.12.
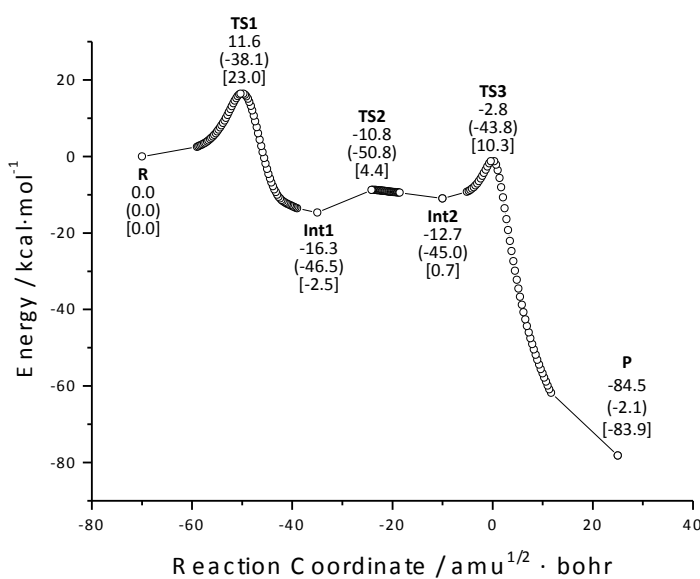
Figure 5.11 IRCs calculated at the M05-2X/6-311G(3df,2p) level. Relative enthalpies (in kcal mol^{-1}) (BSSE corrected), entropies between parentheses (in cal/mol K), and Gibbs energies between brackets (kcal mol^{-1}) at T = 298 K.
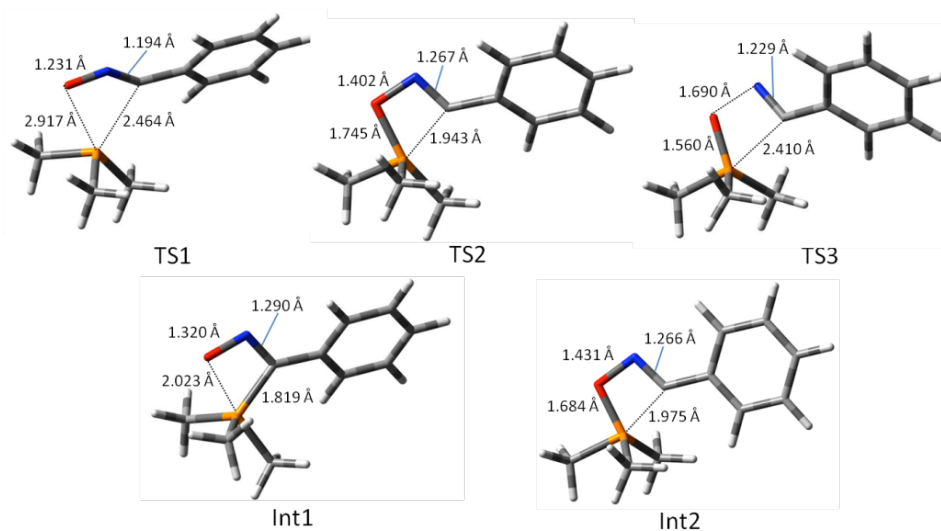
Figure 5.12 Computed structures of intermediates and transition states for reaction of Me₃P and PhCNO at the M05-2X/6-311G(3df,2p) level. See Figure 5.10 for relative energies.

Several alternative mechanisms were also considered. Neither minima nor transition states were located corresponding to a 1,3-cycloaddition of PhNCO to Me₃P according to a concerted mechanism. Likewise, direct OAT from PhNCO to Me₃P was found to be repulsive and did not lead to reaction. A transition state higher in energy with a *syn* disposition of the C_{ipso}–C–N–O moiety was also found (**TS1b**) which is shown in Figure 5.13. This structure resembles that of the SIPr·MesCNO adduct shown in Figure 5.2. The lower energy of TS1 compared to that TS1b can be attributed to electrostatic attraction between the positively charged P atom and the negatively charged O atom. Presumably steric forces do not allow this to be established for the SIPr·MesCNO adduct.[143]
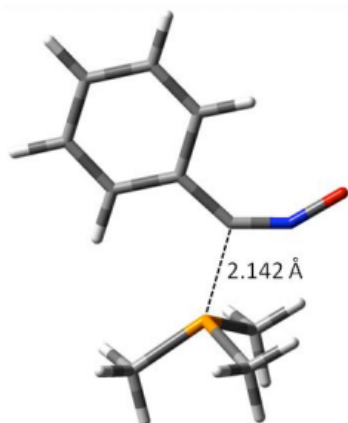
Figure 5.13 Structure of a higher energy transiton state TS1b for reaction between Me₃P and PhCNO.

Reaction of the SIPr·MesCNO Adducts with R₃P, (Ar[ᵗBu]N)₃MoP or (Ar[ᵗBu]N)₃V.

In view of the proposed mechanism of reaction of MesCNO with phosphines, it was of

interest to see how blocking the electrophilic C atom of MesCNO in the SIPr·MesCNO

adduct would affect its OAT reactivity. In that regard, it was important to first establish

that the OAT ability of the SIPr·MesCNO adduct was not reduced significantly with

respect to free MesCNO. Therefore, Eqn. (5.13) and (5.14) were investigated

qualitatively.

$$(Ar[^tBu]N)_3V \ + \ MesCNO \ \longrightarrow \ (Ar[^tBu]N)_3VO \ + \ MesCN \qquad (5.13)$$

$$(5.14)$$
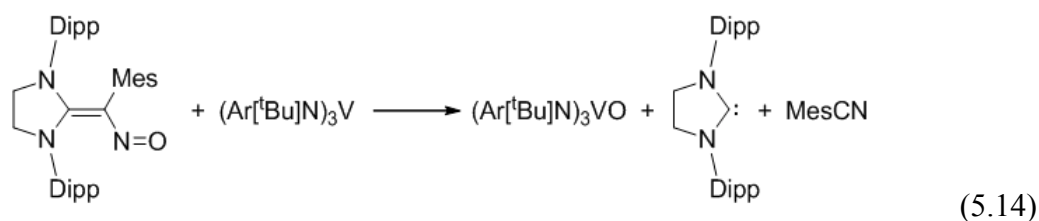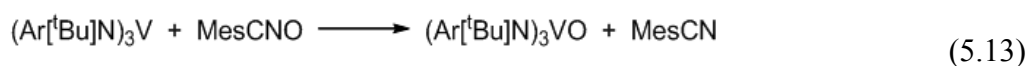
Based on visual observation, both reactions (5.13) and (5.14) occurred

immediately upon mixing at room temperature. Stopped flow kinetic studies have shown

that at room temperature, reaction of the adduct (Eqn. (5.14)) is actually more rapid than

OAT of MesCNO itself (Eqn. (5.13)).[139] It is clear that no significant kinetic reduction in

OAT ability through the O atom site occurred for the SIPr·MesCNO adduct compared to free MesCNO in its reaction with $(Ar[^tBu]N)_3V$. Thus it can be concluded that reaction of coordinatively unsaturated metal complexes with the SIPr·MesCNO adduct is not impaired by coordination of the NHC, in fact it is slightly enhanced.[139]

In contrast, reactivity with R_3P is shut down when an NHC coordinates and blocks the C atom binding site of MesCNO. Thus, reaction (5.15) did not proceed at room temperature over a four hour period.

$$(5.15)$$
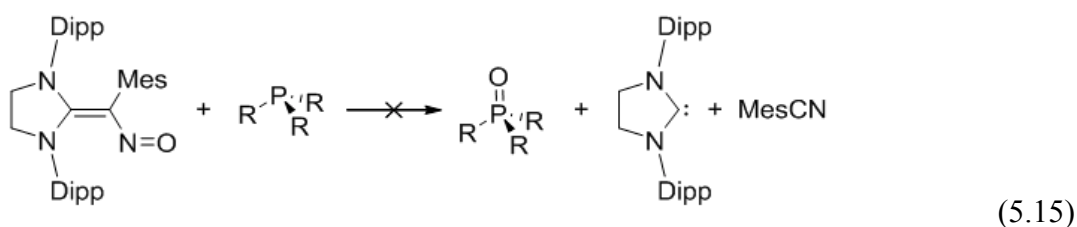
In a similar way $(Ar[^tBu]N)_3MoP$, which is efficiently oxidized by free MesCNO, undergoes no reaction with the SIPr·MesCNO adduct.

Reactions where MesCNO did not perform OAT. In addition to the inability of MesCNO to oxidize the N-heterocyclic carbenes to form the corresponding cyclic ureas, several reactions that are thermodynamically favorable for OAT from MesCNO were found not to occur at room temperature in toluene solution. In spite of the fact that reaction (5.10) occurs, corresponding reaction of $(Ar[^tBu]N)_3MoN$ as shown in Eqn.(5.16) was not observed.[144]

$$(Ar[^tBu]N)_3MoN + MesCNO \xrightarrow{\quad\times\quad} (Ar[^tBu]N)_3MoNO + MesCN$$

$$(5.16)$$
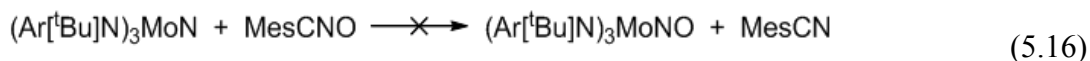
Oxidation of tetrahydrothiophene and of pyridine (Eqn. (5.17) and (5.18)) did not occur over four hours time at room temperature.

(5.17)

(5.18)
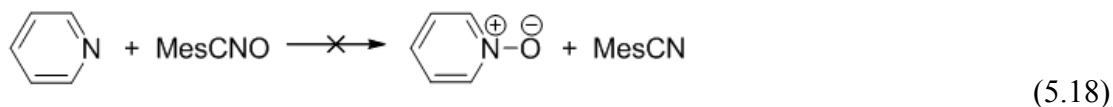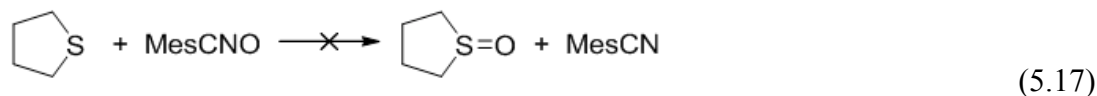
Attempts to oxidize dimethyl sulfoxide with MesCNO also showed no reaction at room temperature over several hours.

5.3 Discussion

MesCNO has proven to be a useful reagent for OAT to phosphines and phosphides for the systems shown in Table 5.1, and this work is now being extended to metal complexes.[139] OAT reactions of MesCNO can follow two different reaction channels: reaction with a Lewis acid may occur at the terminal O, but OAT reactions with a Lewis base may occur by attack at the electrophilic C atom. This second mechanistic possibility was envisioned only after stable adducts between NHC and MesCNO were discovered and shown to involve coordination of the nucleophilic carbene to the electrophilic C atom of MesCNO as shown in Figure 5.2. Since there is a strong similarity between NHCs and R_3P in their coordination chemistry to metals,[145] this suggested that non-metal oxidation by MesCNO may proceed through a similar adduct for the phosphine as that found to be stable for the NHC. The discussion focuses on two areas: *i*. thermochemistry of OAT and its implication for the Mo–P bond in $(Ar[^tBu]N)_3MoPO$, *ii*. The mechanism of OAT to phosphines and phosphides.

Thermochemistry of OAT Reactions. Much thermochemical data on organophosphines date back to work done in the 1950's to 1960's, and modern compilations of experimental data usually can be traced back to work done a half century ago. An exception to that is

Domalski's determination by rotating bomb calorimetry of accurate data for Ph$_3$P and Ph$_3$PO.[146] The data for Ph$_3$P were found to differ by $\approx$ 5 kcal mol^{-1} from work done by Mortimer using static bomb calorimetry.[147] Classic work in reaction calorimetry by Skinner and coworkers on enthalpies of reaction of trialkyl phosphines with H$_2$O$_2$ includes in its final paragraph the possibility that the oxidation reactions may not have been quantitative due to possible formation of trialkyl phosphine peroxides and concludes with the statement: *"In our opinion, the thermochemical results given here need independent verification, possibly by oxidation studies based on some other agent than hydrogen peroxide"*.[148] The value for the P=O BDE in Ph$_3$PO determined in this work in toluene solution of 132.2 ± 3.0 kcal/mol is in good agreement with the gas phase value of Domalski[120] of 135.4 ± 2.8 kcal/mol. The data for Me$_3$P and Cy$_3$P are also in reasonable agreement with values quoted for other trialkyl phosphines reported in the literature.[149] In addition, computed BDE values at the M05-2X/6-311G(3df,2p) level are in excellent agreement with experimental data as shown in Table 5.2.

It is of interest to compare the data in Table 5.1 for OAT to earlier data for SAT. Surprisingly, there is a smaller gap between Ph$_3$P and Cy$_3$P bonded to O than to S. This may be due to a greater significance to π bonding in the P=O compared to P=S bond in R$_3$PE (E = O, S). Thus, the weaker basicity of Ph$_3$P compared to Cy$_3$P may be compensated in its bonding to O by an increased π bonding capacity in Ph$_3$P which would be expected to be a poorer σ donor but better π acceptor than Cy$_3$P. For S, since π-bonding would be expected to be of less importance than for O, the difference between Ph$_3$P and Cy$_3$P would be greater since it is now dominated by the σ-donor ability of the phosphine.

The P=O BDE in Me_3PO (138.5 kcal mol^{-1}) is similar to the fundamental P=O BDE (140.8 kcal mol^{-1}) for the gas phase diatomic molecule phosphorous monoxide. The enthalpy of OAT from MesCNO to $(Ar[^tBu]N)_3MoP$ is nearly 30 kcal mol^{-1} lower than that for Me_3P and yields a very low P–O BDE. Detailed discussion of why the P–O BDE in $(Ar[^tBu]N)_3MoPO$ is so low is not warranted beyond noting that upon loss of an O atom, the Mo complex has a stronger Mo–P bond (Mo–P BDE of −92.2 kcal mol^{-1} in $(Ar[^tBu]N)_3MoP$ vs −60.2 kcal mol^{-1} in $(Ar[^tBu]N)_3MoPO$, see below), whereas this does not happen in the case of phosphines. Furthermore, it was considered of interest to compare the data for $(Ar[^tBu]N)_3MoPO$ to P≡P=O and N≡P=O. Computational studies (see Table 5.2) yielded the following values for the P–O bond dissociation enthalpy (kcal mol^{-1}): $(Ar[^tBu]N)_3MoPO$ [105.9], P≡P=O [90.1], and N≡P=O [78.3]. This trend appears to follow the expected decreasing basicity of the lone pair on P for $(Ar[^tBu]N)_3MoP$ versus P≡P versus N=P. Moreover, dissociation of an O atom from $(Ar[^tBu]N)_3MoPO$ forms $(Ar[^tBu]N)_3MoP$; dissociation of an O from PPO forms P≡P, and from NPO forms N≡P. Since it might reasonably be expected that the strongest triple bond in that series would be N≡P, then it seems reasonable the NPO would be more susceptible to O loss.

Since the enthalpy of formation of PO is known[150] the thermochemical data determined previously for the Mo–P bond in $(Ar[^tBu]N)_3MoP$[151] can be combined with the oxidation of $(Ar[^tBu]N)_3MoP$ to $(Ar[^tBu]N)_3MoPO$ reported here to calculate the enthalpy of coordination of PO to the $(Ar[^tBu]N)_3Mo$ fragment as shown in Scheme 5.2. Data are also included in Scheme 5.2 for N for comparison purposes.[152] The 60.2 kcal mol^{-1} Mo–P BDE in $(Ar[^tBu]N)_3MoPO$ represents a strong metal–ligand bond but is still lower than the Mo–N BDE in $(Ar[^tBu]N)_3MoNO$ of 82.5 kcal mol^{-1}.

$$(Ar[^tBu]N)_3Mo + E + O \xrightarrow[\text{iii.}]{\substack{-140.8\ E=P \\ -150.9\ E=N}} (Ar[^tBu]N)_3Mo + EO$$

$$\text{ii.}\ \substack{-92.2\ E=P \\ -155.3\ E=N} \downarrow \qquad\qquad\qquad \text{iv.}\ \downarrow\ \substack{-60.2\ E=P \\ -82.5\ E=N}$$

$$(Ar[^tBu]N)_3MoE + O \xrightarrow[\text{i.}]{\substack{-108.8\ E=P \\ -78.1\ E=N}} (Ar[^tBu]N)_3MoEO$$
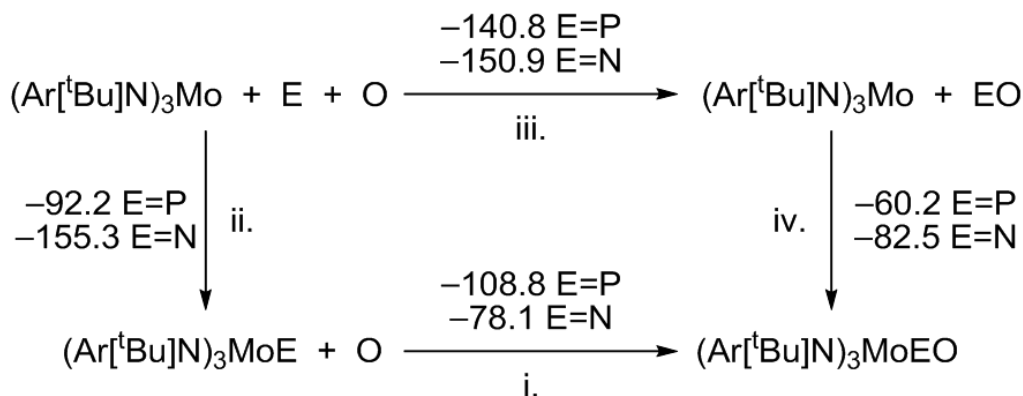
Scheme 5.2 Measured and derived enthalpies for the $(Ar[^tBu]N)_3MoEO$ (E = P, N) all data in kcal mol^{-1}. For data relevant to $(Ar[^tBu]N)_3MoNO$ binding and the $(Ar[^tBu]N)_3MoN$ BDE see ref 52.

It is noteworthy that based on step i. in Scheme 5.2, and a value of 59.5 kcal mol^{-1}

for step iii. of Scheme 5.1 that oxidation of $(Ar[^tBu]N)_3MoE$ by 1/2 O_2 to

$(Ar[^tBu]N)_3MoEO$ is exothermic by 18.6 kcal mol^{-1} for E = N, and 49.3 kcal mol^{-1} for E

= P. Thus, air oxidation of both the nitride and phosphide to the NO and PO complexes is

thermodynamically favored. Oxidation of $(Ar[^tBu]N)_3MoN$ is not as favorable as for

$(Ar[^tBu]N)_3MoP$ and this may be due to in part to the greater strength of the Mo≡N bond

in $(Ar[^tBu]N)_3MoN$. The Mo–N distance in the nitride is shorter than in the nitrosyl

complex. That is in keeping with the stronger Mo–N bond in $(Ar[^tBu]N)_3MoN$

(BDE=155.3 kcal mol^{-1}) than that for $(Ar[^tBu]N)_3MoNO$ (BDE = 82.5 kcal mol^{-1}).

However, as first pointed out by Cummins,[132] the Mo–P distance of 2.079 Å in

$(Ar[^tBu]N)_3MoPO$ is 0.04 Å shorter than the Mo–P distance in $(Ar[^tBu]N)_3MoP$. This

has led to speculation that the longer Mo–P bond in the phosphide may in fact be weaker

than that in the $(Ar[^tBu]N)_3MoPO$ complex. Computations by Frenking and coworkers[153]

are in agreement with the experimental bond distances and they have also concluded that

the Mo–P BDE in $(Ar[^tBu]N)_3MoPO$ is higher than that of $(Ar[^tBu]N)_3MoP$. That

conclusion is at odds with the data in Scheme 5.2 where the Mo–P BDE is nevertheless

30 kcal mol^{-1} higher in the phosphide than in (Ar[^{t}Bu]N)$_3$MoPO in spite of its longer

distance. Bond length and bond strength do not always correlate with each other.[154] The

BDE is the enthalpy of a homolysis reaction (Eqn. (5.19) and (5.20) for the Mo–P bonds

in both species) and thus depends exclusively on the relative stability of reactant and

product states.

$$(Ar[^tBu]N)_3MoP \xrightarrow{\overset{\Delta H = 92.2}{\text{kcal mol}^{-1}}} (Ar[^tBu]N)_3Mo + P \qquad (5.19)$$

$$(Ar[^tBu]N)_3MoPO \xrightarrow{\overset{\Delta H = 60.2}{\text{kcal mol}^{-1}}} (Ar[^tBu]N)_3Mo + PO \qquad (5.20)$$
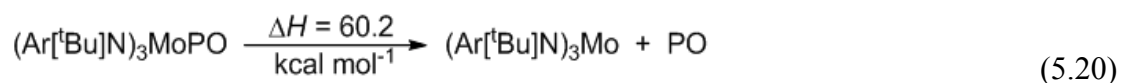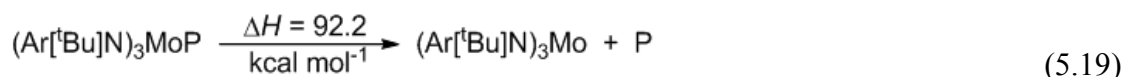
The difference between the two BDEs is related to the fact that when

(Ar[^{t}Bu]N)$_3$MoPO dissociates it produces the stable molecule PO. There is a large

increase in the P–O BDE which follows that dissociation. Subtracting Eqn. (5.19) from

Eqn. (5.20) yields Eqn. (5.21).

$$(Ar[^tBu]N)_3MoPO + P \xrightarrow{\overset{\Delta H = -32}{\text{kcal mol}^{-1}}} (Ar[^tBu]N)_3MoP + PO \qquad (5.21)$$

The difference in BDEs relates directly to the OAT value in Eqn. (5.20). The fact

that PO has a stronger P–O Bond (BDE=140.8 kcal mol^{-1}) than does (Ar[^{t}Bu]N)$_3$MoPO

(BDE=108.9 kcal mol^{-1}) accounts for the apparent discrepancy in bond length/BDE.

Mechanism of OAT from MesCNO to Phosphines and Phosphides. Computational

studies suggest that attack by Me$_3$P at the O atom of MesCNO leads to a repulsive

surface. The computed mechanism entails a gradual rise in energy as the reactants

approach each other at 4-5 Å to make an adduct between the Lewis basic lone pair of

electrons on Me$_3$P, and the Lewis acid site at the electrophilic C atom of MesCNO. The

first transition state (**TS1)** has the highest energy along the pathway in keeping with

experimental failure to observe buildup of any intermediate adduct in the reaction by FTIR or UV-vis spectroscopic studies. The calculated values of $\Delta H^{\ddagger} = 11.6$ kcal mol^{-1} and $\Delta S^{\ddagger} = -38.1$ cal mol^{-1}K^{-1} are in reasonable agreement with the experimental values determined by FTIR spectroscopy in Table 5.3. In the computed structure of **Int1**, corresponding to an adduct between Me$_3$P and the C atom of MesCNO, there is an electrostatic interaction between the positive P atom (formal charge = +1) in the adduct and the O of the NO group (formal charge = −1). For Me$_3$P steric hindrance to this configuration may be smaller than for bulkier phosphines. A shallow intermediate state (**TS2**) is computed along the second part of the reaction trajectory which corresponds to formation of what is approximately a cyclic structure in **Int2**. The enthalpy of activation for the last transition state (**TS3**) is $\Delta H^{\ddagger} = 9.9$ kcal mol^{-1} comparable to the energetic barrier in the first step, however the entropy of activation is $\Delta S^{\ddagger} = 1.2$ cal mol^{-1}K^{-1} making this step more favorable in terms of Gibbs energy. Full establishment of the P=O bond in Me$_3$PO is a powerful driving force for this highly exothermic reaction which proceeds smoothly to completion. This pathway avoids the lone pair-lone pair repulsion that would be present if R$_3$P underwent direct attack at the O atom of MesCNO. In this type of mechanism the C atom functions somewhat like a metal;[155] R$_3$P coordinates and as a consequence of its electron donation develops a partial positive charge. The C atom gains electron density in this interaction and this is delocalized to the O atom of MesCNO. It is noteworthy that blocking the C atom site by prior coordination of an NHC disrupts OAT activity for non-metal but not for metal compounds as shown in Eqn. (5.14) and Eqn. (5.15). This provides support for two different mechanisms being operative in OAT with MesCNO.

There is literature precedent for the second proposed mechanism. Oxidation of nitrile oxides by amine oxides has been proposed to yield nitrosocarbonyls which may be trapped by dienes or other receptors.[156] The proposed first step in this reaction involves nucleophilic attack of the O of the amine oxide at the C of MesCNO to produce a zwitterionic intermediate which then dissociates as shown in Scheme 5.3. The central intermediate zwitterion proposed resembles the computed intermediate **Int1** in Figure 5.11.
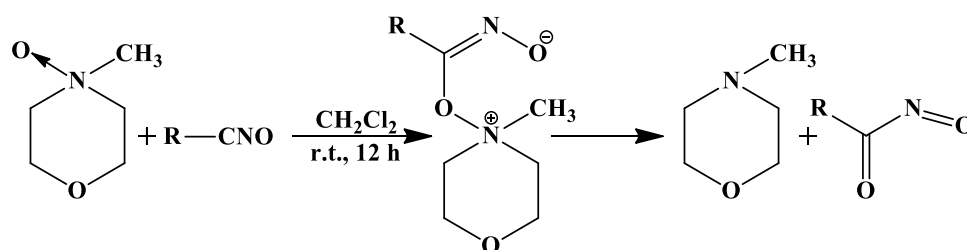
Scheme 5.3 Oxidation of nitrile oxides by amine oxides. See ref 156.

Also of interest are the unsuccessful OAT reactions involving non-metals that were surveyed here including tetrahydrothiophene, pyridine, and $(Ar[^tBu]N)_3MoN$. In spite of being computed to be exothermic in each case, for none of these combinations was OAT observed. An explanation is that for OAT to occur by the mechanism outlined here for non-metals, the nucleophile must be strong enough to form a zwitterionic intermediate by nucleophilic attack at the C atom of MesCNO; however it must also be capable of forming a cyclic intermediate by utilizing expanded valence. It seems plausible that $(Ar[^tBu]N)_3MoN$ and Py, even if they were to form an adduct at C with MesCNO similar to that observed in the reaction of MesCNO with NHCs could not readily undergo valence expansion at the N atom beyond lone pair coordination. Tetrahydrothiophene may be capable of undergoing subsequent OAT chemistry via 1,3-cycloaddition but may not be basic enough to form an adduct with MesCNO. At this

point, we have found only R_3P and, somewhat surprisingly, $(Ar[^tBu]N)_3MoP$ capable of doing this.

5.4   Conclusions

Mesityl nitrile oxide is a versatile OAT reagent. Reactivity with coordinatively unsaturated metal complexes occurs rapidly through initial coordination of the terminal O atom. Oxidation of R_3P and $(Ar[^tBu]N)_3MoP$ on the other hand occurs in minutes at room temperature but follows a different mechanism in which nucleophilic attack at the electrophilic C atom of MesCNO is followed by a cyclic transition state leading to OAT and elimination of MesCN. Reaction of MesCNO with $(Ar[^tBu]N)_3MoP$ provides ready entry to $(Ar[^tBu]N)_3MoPO$ which is a unique terminal phosphorous monoxide complex. However, the P–O BDE in this complex is some 30 kcal•mol^{-1} lower than in R_3PO and corresponds more closely to computed values for PPO or NPO. In spite of the fact that the Mo–P bond in $(Ar[^tBu]N)_3MoPO$ is shorter than in $(Ar[^tBu]N)_3MoP$, the Mo–P BDE in $(Ar[^tBu]N)_3MoPO$ (60.2 kcal•mol^{-1}) is lower than in $(Ar[^tBu]N)_3MoP$ (92.2 kcal•mol^{-1}). This may be attributed to the fact that dissociation of PO results in an increase in the P–O bond strength for the free molecule compared to its adduct. Neither $(Ar[^tBu]N)_3MoN$, THT, nor Py are oxidized under the same conditions in which R_3P oxidation is facile. It appears that two criteria exist for the OAT via this mechanism: i. the reagent must be nucleophilic enough for adduct formation at the C atom, ii. It must be capable of expanded valence for a cyclic OAT transition state. Coordination of R_3P appears to satisfy both these requirements. The novel remote site attack displayed here may be of utility in design of other reagents to achieve difficult OAT reactions to other

non-metal substrates. Additional synthetic, mechanistic, and thermochemical studies are in progress to expand understanding and utilization of OAT reactivity of nitrile oxides.

5.5 Experimental

A. Synthesis

Unless stated otherwise, all operations were performed in a Vacuum Atmospheres or MBraun drybox under an atmosphere of purified nitrogen or argon. Diethyl ether and toluene were dried and deoxygenated by the method of Grubbs.[157] C_6D_6 was purchased from Cambridge Isotopes. The deuterated solvents were degassed and dried over 4 Å molecular sieves. The 4 Å sieves and Celite were dried in vacuo overnight at a temperature just above 200 °C. Mesityl nitrile oxide was prepared and recrystallized according to the literature.[158] All other compounds were used as received. ^{1}H NMR spectra were recorded on a Bruker Avance-400 spectrometer at room temperature. ^{1}H NMR chemical shifts are reported in parts per million (ppm) with respect to the protio impurities referenced at 7.16 ppm for C_6D_6 and 2.09 ppm for toluene-d^8. FTIR spectra were obtained using a Perkin Elmer Spectrum 400 FTIR Spectrometer. Calorimetric measurements were made using a Setaram C-80 Calvet microcalorimeter.

Synthesis of (Ar[^{t}Bu]N)$_3$MoPO using MesCNO. In the glove box, 299 mg (0.456 mmol) of bright yellow (Ar[^{t}Bu]N)$_3$MoP[132] was dissolved in 5 ml CH_2Cl_2 and the solution was cooled to −35 °C. A solution of MesCNO, 84 mg (1.1 equiv) in 2 mL CH_2Cl_2 (also cooled to −35 °C) was added rapidly to the yellow solution. An additional 1 mL of chilled CH_2Cl_2 was used to ensure that all MesCNO had been transferred to the reaction mixture. Upon warming to room temperature, the reaction mixture changed from yellow to deep purple in color. The mixture was stirred for one hour after mixing to insure complete

reaction. The mixture was then filtered through a bed of Celite, which was washed with 5 mL of chilled CH_2Cl_2. The filtrate was then reduced in volume to *ca.* 50% of its original volume. The purple reaction mixture was cooled and 30 mL of thawing acetonitrile was added to precipitate the product. The cold mixture was filtered on a medium-porosity glass frit, and the purple solid was washed with 10 mL cold acetonitrile. The solid was dried under reduced pressure and yielded $(Ar[^tBu]N)_3MoPO$ as a deep purple powder (175 mg, 0.261 mmol, 57%). ^1H and ^{31}P NMR data agreed with previously published data.[123]

Synthesis of the SIPR·MesCNO Adduct. In the glove box, 0.400 g SIPr in 10 mL toluene was added 0.1657 g MesCNO and the mixture was shaken to dissolve the MesCNO. The solution turned blue-violet and some solid began to precipitate out. It was left undisturbed in the glove box overnight. Evaporation of toluene and addition of heptane led to isolation of the pure adduct in 95 % yield. Analysis for $C_{37}H_{49}N_3O$: theory (found): C 80.5 (79.2), H 8.9 (8.9), N 7.6 (7.0). The mass spectrum showed a strong peak at 552.39 corresponding to P + 1 for $C_{37}H_{49}N_3O$ = 551.38. ^1H NMR (400M, C_6D_6): δ= 6.89 (t, 2H, *p*-Ph of SIPr), 6.76 (d, 4H, *m*-Ph of SIPr), 6.45 (s, *m*-Ph of MesCNO), 3.64 (t, 4H, CH_2 of SIPr), 3.32 (septet, 4H, CH of ^iPr), 2.04 (s, 3H, *p*-CH_3 of MesCNO), 1.84 (s, 6H, *o*-CH_3 of MesCNO), 1.26 (d, 12H, CH_3 of ^iPr), 0.95 (d, 12H, CH_3 of ^iPr) ppm.

Reaction of the SIPr·MesCNO adduct with $(Ar[^tBu]N)_3V$ and $(Ar[^tBu]N)_3Mo$. In the glove box, 0.010 g $(Ar[^tBu]N)_3V$ was dissolved into 1 mL C_6D_6 and this solution was syringed onto 0.0095 g of the blue SIPr·MesCNO adduct in a vial. The mixture was shaken and there was an immediate change in color to red-orange. The sample was transferred to an NMR tube. Analysis of the NMR spectrum showed complete conversion

to MesCN, $(Ar[^tBu]N)_3VO$, and free SIPr. Similar results were obtained using $(Ar[^tBu]N)_3Mo$.

Attempted Reaction of SIPr·MesCNO and $(Ar[^tBu]N)_3MoP$ and Cy_3P. In the glove box, 0.0295 g $(Ar[^tBu]N)_3MoP$ was dissolved into 2 mL C_6D_6 and this solution was syringed onto 0.025 g of the blue SIPr·MesCNO adduct in a vial. The mixture was shaken yielding a green solution. The sample was transferred to an NMR tube. Analysis of the NMR spectrum showed no reaction had occurred after a three hour period. Similar results were obtained in the attempted reaction of SIPr·MesCNO and Cy_3P. In this case the solution remained blue in color, and no reaction could be detected by NMR spectroscopy.

Attempted Reaction of MesCNO and Pyridine, Tetrahydrothiophene and $(Ar[^tBu]N)_3MoN$. Several reagents were checked qualitatively at room temperature for reactivity with MesCNO. A total of 27.9 mg MesCNO was dissolved in 1 mL toluene. To this was added 1 mL pyridine and the solution was monitored by FTIR spectroscopy. No decrease in the band due to MesCNO was observed over approximately four hours. In similar experiments, tetrahydrothiophene and also $(Ar[^tBu]N)_3MoN$ were found to not react at room temperature as followed by NMR and FTIR spectroscopy.

B. Crystallographic Data

Crystallographic Analyses. Violet single crystals of SIPr·MesCNO suitable for X-ray diffraction analyses obtained by evaporation of solutions of toluene at 25 °C, crystallized in the monoclinic crystal system. The data crystal was glued onto the end of a thin glass fiber. X-ray intensity data were measured by using a Bruker SMART APEX2 CCD-based diffractometer using Mo Kα radiation (λ = 0.71073 Å). The raw data frames were

integrated with the SAINT+ program by using a narrow-frame integration algorithm.[159] Corrections for Lorentz and polarization effects were also applied with SAINT+. An empirical absorption correction based on the multiple measurement of equivalent reflections was applied using the program SADABS. All structures were solved by a combination of direct methods and difference Fourier syntheses, and refined by full-matrix least-squares on F^2, by using the SHELXTL software package.[160] Crystal data, data collection parameters, and results of the analyses are listed in supporting information.

The systematic absences in the intensity data were consistent with the unique space group $P2_1/c$. Half a molecule of toluene from the solvent of crystallization cocrystallized with the complex and is present in the asymmetric crystal unit. The toluene molecule is disordered about an inversion center, and was modeled in part using geometric restraints and refined with isotropic thermal parameters. However, this disorder could not be completely resolved, which resulted in the relatively high R value (7.46 %). There is not much disorder present in the non-solvent part of the structure. An ORTEP drawing of the structure is shown in the results section.

Crystallographic Data

	SIPr·MesCNO
Empirical formula	$C_{37}H_{47}N_3O \cdot \frac{1}{2}C_7H_8$
Formula weight	597.86
Crystal system	Monoclinic
Lattice parameters	
a (Å)	17.3510(17)
b (Å)	12.9808(13)
c (Å)	16.5439(16)
β (deg)	96.425(2)
V (Å^3)	3702.8(6)
Space group	$P2_1/c$ (# 14)
Z value	4
ρ_{calc} (g / cm^3)	1.072
μ (Mo Kα) (mm^{-1})	0.064
Temperature (K)	296
$2\Theta_{max}$ (°)	50.00
No. Obs. ($I > 2\sigma(I)$)	3207
No. Parameters	399
Goodness of fit	1.020
Max. shift in cycle	0.001
Residuals*:R1; wR2	0.0746; 0.2089
Absorption Correction, Max/min	Multi-scan 0.7457/0.6706
Largest peak in Final Diff. Map (e$^-$ / Å^3)	0.658

$*R = \Sigma_{hkl}(||F_{obs}|-|F_{calc}||)/\Sigma_{hkl}|F_{obs}|$; $R_w = [\Sigma_{hkl}w(|F_{obs}|-|F_{calc}|)^2/\Sigma_{hkl}wF_{obs}^2]^{1/2}$,
$w = 1/\sigma^2(F_{obs})$; GOF $= [\Sigma_{hkl}w(|F_{obs}|-|F_{calc}|)^2/(n_{data}-n_{vari})]^{1/2}$.

C. Calorimetric Measurements

Calorimetric Measurement of Reaction of (Ar[^{t}Bu]N)$_3$MoP and R$_3$P with MesCNO.

In the glove box a solution of 0.5093 g (Ar[^{t}Bu]N)$_3$MoP (0.776 mmol) was dissolved in 6

mL C$_6$D$_6$ and 1 mL of this stock solution was loaded into an NMR tube. The remaining 5

mL of solution were loaded into the Calvet calorimeter cell with MesCNO (0.0100 g, 0.062 mmol) as limiting reagent. The calorimeter cell was sealed, taken from the glove box, and loaded into the Setaram C-80 calorimeter. Following temperature equilibration, the reaction was initiated and the calorimeter rotated to achieve mixing. Following return to baseline the calorimeter cell was taken into the glove box, opened and 1 mL of the solution loaded into an NMR tube. NMR spectra of both the stock solution and calorimetry solution were then acquired and the reaction was confirmed as quantitative. The enthalpy of three measurements done in this way led to $\Delta H = -52.3 \pm 0.7$ kcal mol^{-1} based on the reaction: $(Ar[^{t}Bu]N)_3MoP$ (tol. sol.) + MesCNO (solid) $\rightarrow$ $(Ar[^{t}Bu]N)_3MoPO$ (tol. sol.) + MesCN (tol sol.). To these data the enthalpy of solution of MesCNO in toluene ($+4.3 \pm 0.1$ kcal mol^{-1}) was subtracted to give $\Delta H_{rxn} = -56.6 \pm 0.8$ kcal mol^{-1} with all species in toluene solution. Reactions of R_3P were performed in a similar fashion, but typically with five independent measurements on each phosphine.

D. Kinetic Measurements

UV-vis Kinetic Study of Reaction of $(Ar[^{t}Bu]N)_3MoP$ and MesCNO. Solid $(Ar[^{t}Bu]N)_3MoP$ and MesCNO were dissolved in dry dichloromethane or dry toluene under Ar in an MBraun glovebox. The solutions of $(Ar[^{t}Bu]N)_3MoP$ were loaded into 1 cm path length air tight quartz cuvettes, and solutions of MesCNO were loaded into Hamilton gas tight syringes. Initial spectra of $(Ar[^{t}Bu]N)_3MoP$ (0.6 mM) were collected on a JASCO V-570 UV-vis/NIR spectrophotometer, the MesCNO solution was added to the cuvette via syringe, and the reaction was monitored in 1-10 minute intervals over a total time of 20-60 minutes. Variable temperature (15-45 °C) measurements were achieved using the JASCO PSC-498T temperature controller. The kinetic experiments

were run under pseudo first order conditions with excess MesCNO (25 mM-100 mM) by monitoring the absorbance increase at λ = 550 nm. Data analysis was performed with IGOR pro 5.0 by WaveMetrics.

FTIR Kinetic Study of the Reaction of MesCNO with R$_3$P, and (Ar[^{t}Bu]N)$_3$MoP. In the glove box, a stock solution of MesCNO was prepared (0.125 g in 20 mL freshly distilled toluene). In a separate vial, 0.100 g of (Ar[^{t}Bu]N)$_3$MoP was dissolved in 2 mL of toluene. A 5 mL syringe was loaded with 4 mL of the MesCNO stock solution and a 2.5 mL syringe was used to load the 2.0 mL of (Ar[^{t}Bu]N)$_3$MoP in toluene. The 4.0 mL solution was loaded into a thermostatted reaction vessel and allowed to equilibrate with respect to temperature. The 2.0 mL (Ar[^{t}Bu]N)$_3$MoP solution was then injected into the reactor and the timer started. The thermostatted reaction vessel was fitted via thick wall Teflon tubing lines to a thermostatted FTIR cell kept in a temperature and environment controlled chamber. A total of 4.0 mL of solution was flushed under Ar pressure through the tubing and cell through a valve with tubing leading to a vent. The valve was closed so that under Ar pressure, the thermostatted cell was filled with a solution 0.0258 M in MesCNO and 0.0254 M in (Ar[^{t}Bu]N)$_3$MoP. A series of FTIR spectra were collected of the reaction mixture approximately every 20 seconds through the first two half lives, and at a slightly slower rate as the reaction progressed. Data for the nearly equimolar reaction were analyzed by standard techniques and found to obey second order kinetics. Averaged rate data are collected in Table 5.3 for reactions studied by FTIR spectroscopy.

E. Computational Details

Electronic structure calculations were carried out using the B3LYP[161, 162] and M05-2X[163] density functionals with the 6-311G(d,p) and 6-311G(3df,2p) basis sets as

implemented in the Gaussian 09 suite of programs.[164] Minimum energy and transition state structures were optimized by computing analytical energy gradients. The obtained stationary points were characterized by performing energy second derivatives, confirming them as minima or first order saddle points by the number of negative eigenvalues of the hessian matrix of the energy (zero and one negative eigenvalues respectively). Computed electronic energies were corrected for zero-point energy, thermal energy, and entropic effects to obtain the corresponding thermodynamic properties H^0 and G^0. To derive binding energies, the basis set superposition error (BSSE) was computed using counterpoise calculations.[165] For the metal-containing species $(Ar[^tBu]N)_3MoP$ and $(Ar[^tBu]N)_3MoPO$, optimizations were performed using the Stuttgart-Dresden MWB28[166] quasi-relativistic effective core potential and basis including a set of additional f functions for Mo and the triple-zeta quality basis set (6-311G(d,p)) for all other elements.

Intrinsic reaction coordinate (IRC) calculations[167] were done in order to describe the reaction mechanism for PhCNO and Me_3P, providing the connection between the minimum energy points through the different transitions states. Further optimization of the final points of the IRCs with steepest descent algorithm was done in order to obtain the real minimum energy structures.

Moreover, the energy of the compounds studied was calculated using Gaussian-n theory at the G3 level when applicable.[168] G3 corresponds effectively to calculations at the QCISD(T)/G3large level, G3large being a modification of the 6-311+G(3df,2p) basis set, including more polarization functions for the second row (3d2f), less on the first row (2df), and other changes to improve uniformity. In addition, some core polarization

functions are added. Single-point energy calculations are carried out on MP2(full)/6-31G(d) optimized geometries, incorporating scaled HF/6-31G(d) zero-point vibrational energies, a so-called higher-level correction to accommodate remaining deficiencies, and spin-orbit correction for atomic species only.

Overview and Future Outlook

The work in this thesis has visited a number of small areas (villages) and two major ones (cities). The major conclusions compare the energetics and mechanism of binding of dioxygen to two quite different complexes--Pd(IPr)$_2$ and V(N^{t}BuAr)$_3$. The enthalpies of binding are quite different--binding of O$_2$ to Pd(IPr)$_2$ is exothermic by 24.0 kcal/mol whereas V(N^{t}BuAr)$_3$ is exothermic by 75 kcal/mol. Compared to Pd(IPr)$_2$, a simpler picture emerges for the mechanism of binding of O$_2$ to V(N^{t}BuAr)$_3$--namely initial binding to form an η^1-O$_2$ complex is rapid (k_1(-62 °C) = 26,100 M^{-1}s^{-1}, $\Delta H^{\ddagger}$ = 3.3 kcal/mol; $\Delta S^{\ddagger}$ = -22 cal/mol•K). For Pd(IPr)$_2$, the binding is even faster: (k_1(-62 °C) = 128,100 M^{-1}s^{-1} (extrapolated from Eyring plot), $\Delta H^{\ddagger}$ = 6.0 kcal/mol; $\Delta S^{\ddagger}$ = -6 cal/mol•K).

However, an important difference is that in binding to Pd(IPr)$_2$, we are referring to binding all the way to the η^2 complex--passing through the η^1 and going to the η^2 binding mode faster than V(N^{t}BuAr)$_3$ is able to bind η^1. For V(N^{t}BuAr)$_3$, conversion of η^1 to η^2, while rapid, occurs as a clearly identifiable second step with $\Delta H^{\ddagger}$ = 10.3 kcal/mol; $\Delta S^{\ddagger}$ = -6 cal/mol K. There must be a significantly lower barrier to formation of the η^2 complex for Pd(IPr)$_2$.

Kinetic studies showed that for V(N^{t}BuAr)$_3$, it was conversion of the η^2 complex to its more reactive η^1 form that was rate determining in reaction with a second mole of V(N^{t}BuAr)$_3$ to form two moles of oxo. Likewise, the thermal instability leading to unknown products is believed to also procced by conversion of the η^2 complex to the

more reactive η^1 which in the absence of an available O acceptor undergoes self-oxidation and decomposition.

The more complex nature of binding of O_2 to $Pd(IPr)_2$ incorporates some of the features discussed above for $V(N^tBuAr)_3$, but a richer chemistry exists in that the η^2 complex complex formed initially at low T, is capable of adding a second mole of O_2 at higher T to form the bis η^1 complex. This is believed to occur via reversion of the η^2 complex back to its η^1 form which is then trapped by a second mole of O_2. In a similar way, reactivity with H_2O was believed to be enhanced when an η^1-O_2 complex was kinetically accessible. Both of these areas lead to the conclusion that the factors of what controls η^1-O_2 binding are central to understanding its reactivity. While it is conceivable that in some imagined complex the η^2-O_2 binding motif would be more reactive, that goes against the chemical intuition which dictates that in order to react, one end of the bound O_2 must detach itself from the metal as a first step in the process. This work has added insight to the nature of the η^1-O_2 to η^2-O_2 conversion in oxygen binding.

A number of avenues of research have been opened but their development remains to be completed. Additional facts about the mechanism of binding, particularly addition of the second mole of O_2 needs to be completed. Additional knowledge about the reactivity of the η^1-O_2 complexes needs to be investigated. The basic question addressed here-how O_2 binds to a vacant coordination site, is not fully answered at this time.

The question of how O_2 binds and is activated, even when fully answered, will still represent only a first step in catalyst design. Detailed knowledge of substrate binding, and how the other steps play out will be needed. For example, none of the complexes we

studied proved to be capable of catalysis and were even sluggish at stoichiometric oxidations. A dominant reason for that is probably due to the steric crowding present in the system. This presents a paradox--in order to form the highly reactive η^1 complexes we have observed--either as a stable complex $(Pd(IPr)_2(\eta^1\text{-}O_2)_2)$ or a fleeting intermediate the complex must prohibit rapid rearrangement to the more stable η^2 form. The steric bulkiness required to achieve this limits the possible utility of the complex itself as a catalyst. One possible way to avoid this, as illustrated in Figure 3.6 would be design of a binuclear catalyst with a separate binding site in close proximity to the "furnace" where the activated form of oxygen is bound. There are no doubt other, possibly better, design motifs available. In terms of understanding the binding step, it is hoped that this work has made some contributions to that area. If so, they are small compared to the wealth of knowledge that will be needed to design real catalysts for future selective oxidation chemistry. In spite of that, the author believes, that such a goal is both important and attainable, and that it will be achieved in the future.

Appendix
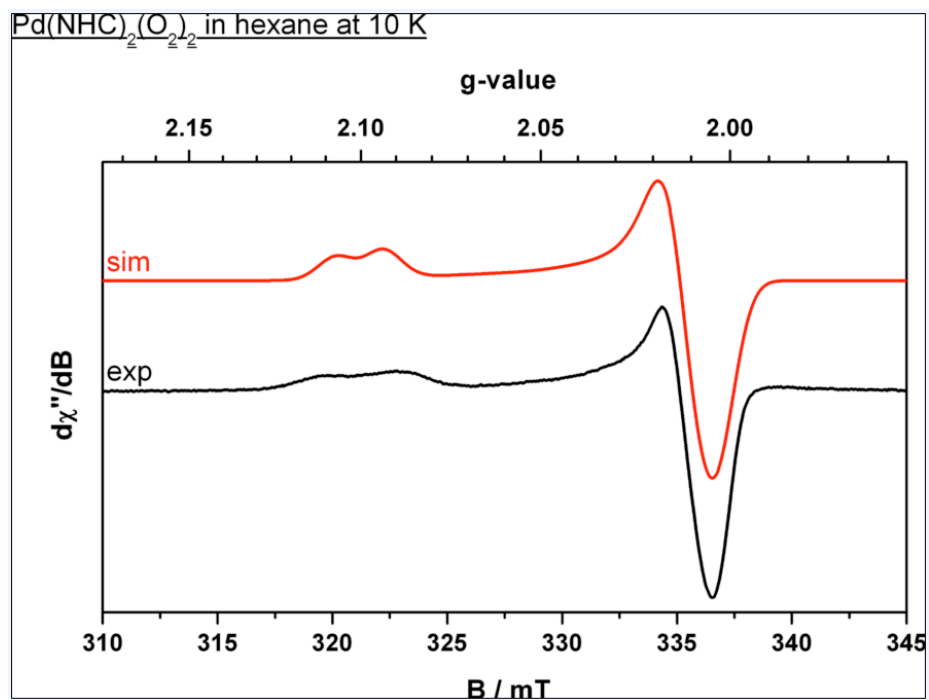
Figure A.1 Simulated and experimental EPR spectrum of *trans*-Pd(IPr)$_2$(η^1-O$_2$)$_2$ in hexane at 10K.
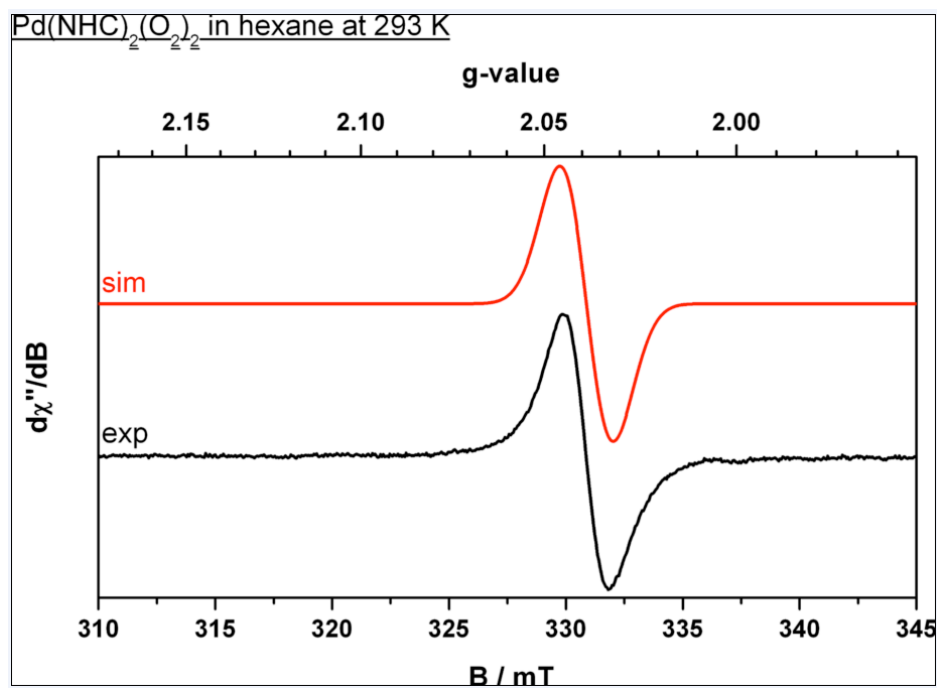
Figure A.2 Simulated and experimental EPR spectrum of *trans*-Pd(IPr)$_2$(η^1-O$_2$)$_2$ in hexane at 293K.
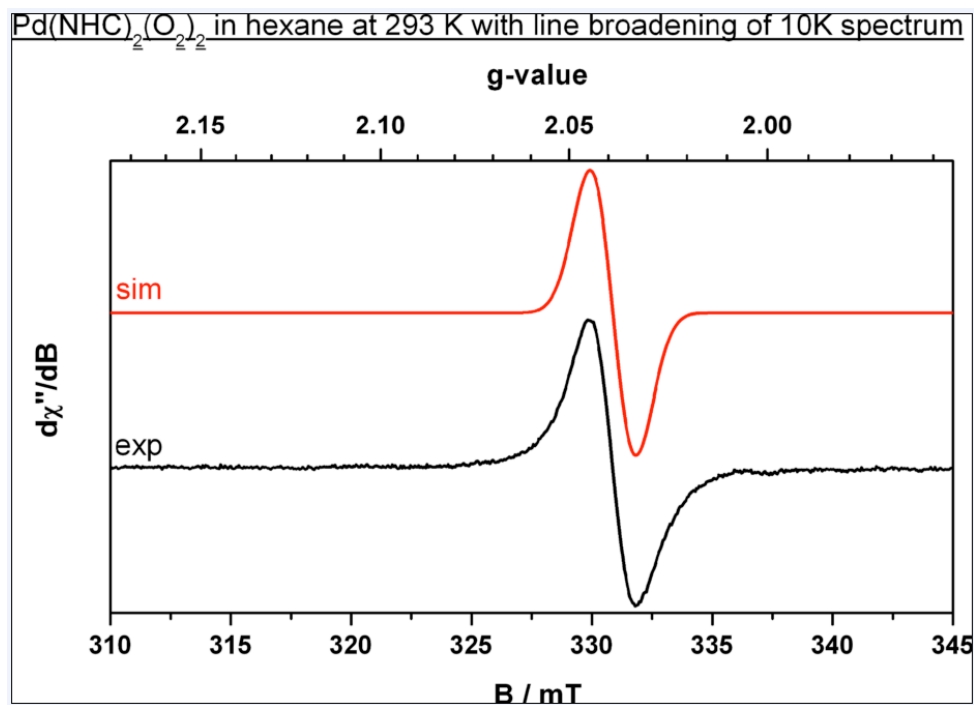
Figure A.3 Simulated and experimental EPR spectrum of *trans*-Pd(IPr)$_2$(η^1-O$_2$)$_2$ in hexane at 293K with line broadening of 10K spectrum.
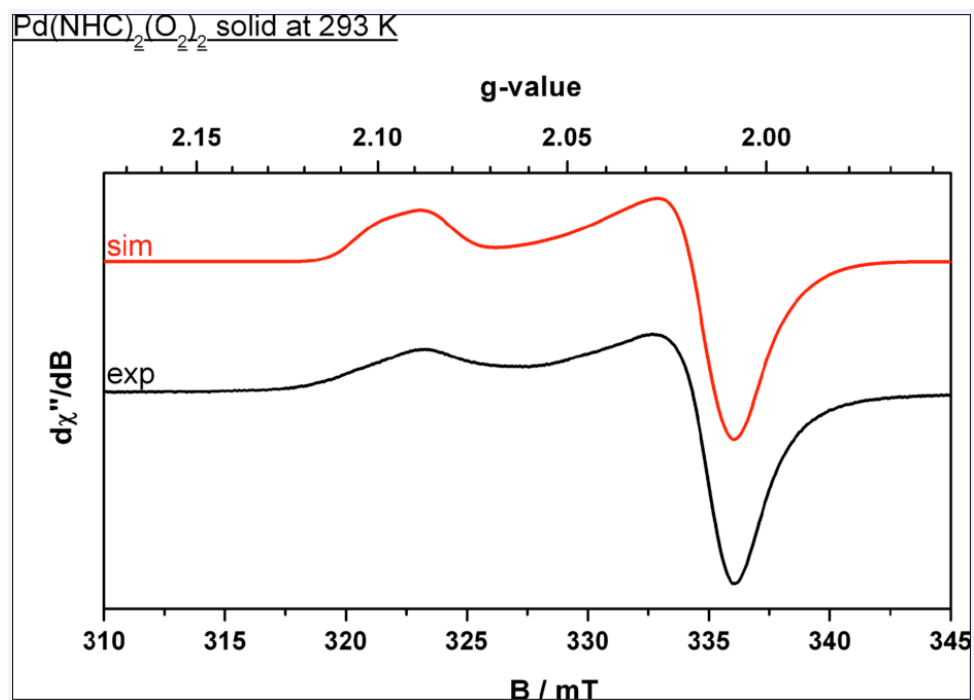
Figure A.4 Simulated and experimental EPR spectrum of solid *trans*-Pd(IPr)$_2$(η^1-O$_2$)$_2$ at 293K.
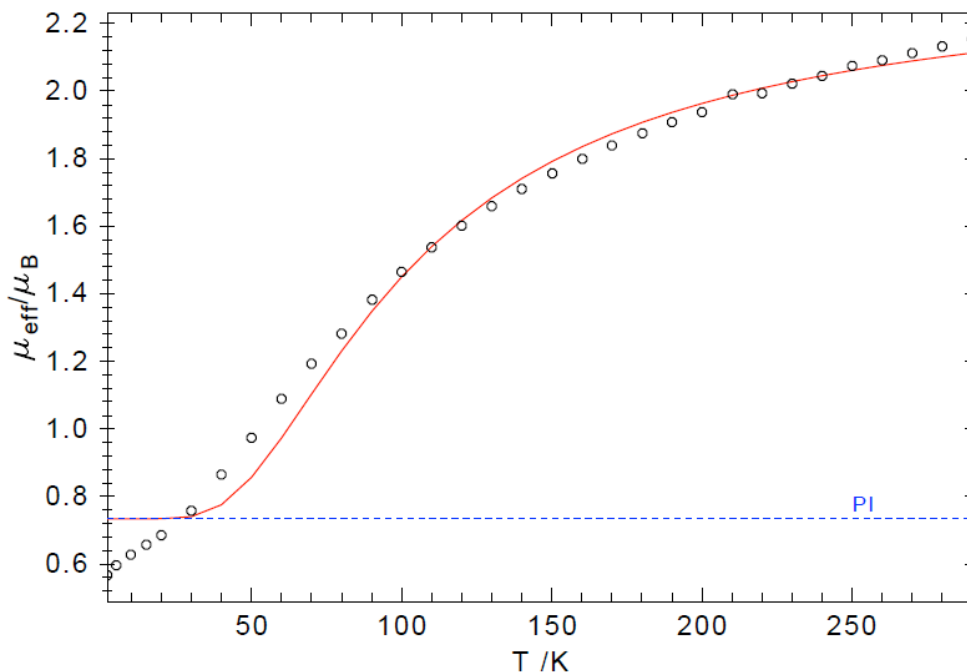
Figure A.5 SQUID magnetometry data of *trans*-Pd(IPr)$_2$(η^1-O$_2$)$_2$ (open circles) along with simulated data (red line).

The data are consistent with a singlet diradical ground state for *trans*-Pd(IPr)$_2$(η^1-O$_2$)$_2$. The coupling constant (J), determined by SQUID magnetometry is -82(2) cm^{-1}, in very good agreement with the DFT-calculated J value of -113 cm^{-1}. The EPR data are also in agreement. Either in the solid state at room temperature or in a frozen hexane solution we find a pseudo-axial EPR spectrum with two features on the low-field signal (ca. 320 mT). This splitting results from the small zero-field splitting for this complex (D = 0.001 cm^{-1}) and can thus not be fit with an S = 1/2 model. The small D is exactly what one would expect for a triplet spin system centered on 2p-element nuclei. We have also collected the room temperature solution-state spectrum, which can be fit well by simply applying the same parameters as those used to fit the frozen solution spectrum, changing only the anisotropic g-values to a single value that is the average of the three. Increasing

the line broadening slightly then gives an excellent fit between the experiment and the model.

CASSCF and MRCI calculations are performed on a truncated form of this complex. These calculations indicate that the ground state is a nearly equal mixture of the closed-shell singlet and the doubly-excited configurations. These results get to the same general picture as the broken symmetry DFT methods, but they do so more rigorously and also allow us to quantify certain aspects of interest. One of these is the diradical index, which for this system is very high (>99%), and the calculations do consistently predict the singlet as the ground state.

References

1. Weissermel, K.; Arpe, H.-J., Industrial Organic Chemistry, 3rd ed., VCH, New York, **1997**.

2. Meier, G.; Braun, T., Hydrogenation of a Rhodium Peroxido Complex by Formate Derivatives: Mechanistic Studies and the Catalytic Formation of H_2O_2 from O_2. *Angewandte Chemie International Edition* **2012,** *51* (50), 12564-12569.

3. Oyama, S. T.; Desikan, A. N.; Hightower Joe, W., Research Challenges in Selective Oxidation. In Catalytic Selective Oxidation, *American Chemical Society*: **1993**; Vol. 523, pp 1-14.

4. Boisvert, L.; Goldberg, K. I., Reactions of Late Transition Metal Complexes with Molecular Oxygen. *Accounts of Chemical Research* **2012,** *45* (6), 899-910.

5. Selected publications for heterogeneous catalysts:
a) Gong, J.; Mullins, C. B., Selective Oxidation of Ethanol to Acetaldehyde on Gold. *Journal of the American Chemical Society* **2008**, 130 (49), 16458-16459. b) Yoon, S.-M.; Kim, S. J.; Shin, H.-J.; Benayad, A.; Choi, S. J.; Kim, K. K.; Kim, S. M.; Park, Y. J.; Kim, G.; Choi, J.-Y.; Lee, Y. H., Selective Oxidation on Metallic Carbon Nanotubes by Halogen Oxoanions. *Journal of the American Chemical Society* **2008,** *130* (8), 2610-2616. c) Yurdakal, S.; Palmisano, G.; Loddo, V.; Augugliaro, V.; Palmisano, L., Nanostructured Rutile TiO_2 for Selective Photocatalytic Oxidation of Aromatic Alcohols to Aldehydes in Water. *Journal of the American Chemical Society* **2008,** *130* (5), 1568-1569. d) Tada, M.; Muratsugu, S.; Kinoshita, M.; Sasaki, T.; Iwasawa, Y., Alternative Selective Oxidation Pathways for Aldehyde Oxidation and Alkene Epoxidation on a SiO_2-Supported Ru−Monomer Complex Catalyst. *Journal of the American Chemical Society* **2009,** *132* (2), 713-724. e) Li, X.-H.; Chen, J.-S.; Wang, X.; Sun, J.; Antonietti, M., Metal-Free Activation of Dioxygen by Graphene/g-C_3N_4 Nanocomposites: Functional Dyads for Selective Oxidation of Saturated Hydrocarbons. *Journal of the American Chemical Society* **2011,** *133* (21), 8074-8077. f) Tanaka, A.; Hashimoto, K.; Kominami, H., Preparation of Au/CeO_2 Exhibiting Strong Surface Plasmon Resonance Effective for Selective or Chemoselective Oxidation of Alcohols to Aldehydes or Ketones in Aqueous Suspensions under Irradiation by Green Light. *Journal of the American Chemical Society* **2012,** *134* (35), 14526-14533. g) Yang, X.-L.; Xie, M.-H.; Zou, C.; He, Y.; Chen, B.; O'Keeffe, M.; Wu, C.-D., Porous Metalloporphyrinic Frameworks Constructed from Metal 5,10,15,20-Tetrakis(3,5-biscarboxylphenyl)porphyrin for Highly Efficient and Selective Catalytic Oxidation of Alkylbenzenes. *Journal of the American Chemical Society* **2012,** *134* (25), 10638-10645.

6. Selected publications for homogeneous catalysts:
a) Smidt, J.; Hafner, W.; Jira, R.; Sedlmeier, J.; Sieber, R.; Rüttinger, R.; Kojer, H., Katalytische Umsetzungen von Olefinen an Platinmetall-Verbindungen Das Consortium-Verfahren zur Herstellung von Acetaldehyd. *Angewandte Chemie* **1959,** *71* (5), 176-182.

b) Hosokawa, T.; Murahashi, S., New Aspects of Oxypalladation of Alkenes. *Accounts of Chemical Research* **1990,** *23* (2), 49-54. c) Peterson, K. P.; Larock, R. C., Palladium-Catalyzed Oxidation of Primary and Secondary Allylic and Benzylic Alcohols. *The Journal of Organic Chemistry* **1998,** *63* (10), 3185-3189. d) Steinhoff, B. A.; Fix, S. R.; Stahl, S. S., Mechanistic Study of Alcohol Oxidation by the Pd(OAc)$_2$/O$_2$/DMSO Catalyst System and Implications for the Development of Improved Aerobic Oxidation Catalysts. *Journal of the American Chemical Society* **2002,** *124* (5), 766-767. e) Mandal, S. K.; Sigman, M. S., Palladium-Catalyzed Aerobic Oxidative Kinetic Resolution of Alcohols with an Achiral Exogenous Base. *The Journal of Organic Chemistry* **2003,** *68* (19), 7535-7537.

7. Döbler, C.; Mehltretter, G. M.; Sundermeier, U.; Beller, M., Osmium-Catalyzed Dihydroxylation of Olefins Using Dioxygen or Air as the Terminal Oxidant. *Journal of the American Chemical Society* **2000,** *122* (42), 10289-10297.

8. Stahl, S. S., Palladium Oxidase Catalysis: Selective Oxidation of Organic Chemicals by Direct Dioxygen-Coupled Turnover. *Angewandte Chemie International Edition* **2004,** *43* (26), 3400-3420.

9. Keith, J. A.; Nielsen, R. J.; Oxgaard, J.; Goddard, W. A., Unraveling the Wacker Oxidation Mechanisms. *Journal of the American Chemical Society* **2007,** *129* (41), 12342-12343.

10. Groves, J. T.; Quinn, R., Aerobic Epoxidation of Olefins with Ruthenium Porphyrin Catalysts. *Journal of the American Chemical Society* **1985,** *107* (20), 5790-5792.

11. Neumann, R.; Dahan, M., A Ruthenium-substituted Polyoxometalate as an Inorganic Dioxygenase for Activation of molecular oxygen. *Nature* **1997,** *388*, 353-355.

12. Vaska, L., Oxygen-Carrying Properties of a Simple Synthetic System. *Science* **1963,** *140* (3568), 809-810.

13. Rybak-Akimova, E. V., Mechanisms of Oxygen Binding and Activation at Transition Metal Centers. In *Physical Inorganic Chemistry*, John Wiley & Sons, Inc.: **2010**; pp 109-188.

14. Carreón-Macedo, J.-L.; Harvey, J. N., Do Spin State Changes Matter in Organometallic Chemistry? A Computational Study. *Journal of the American Chemical Society* **2004,** *126* (18), 5789-5797.

15. Unno, M.; Chen, H.; Kusama, S.; Shaik, S.; Ikeda-Saito, M., Structural Characterization of the Fleeting Ferric Peroxo Species in Myoglobin: Experiment and Theory. *Journal of the American Chemical Society* **2007,** *129* (44), 13394-13395.

16. Popp, B. V.; Stahl, S. S., Insertion of Molecular Oxygen into a Palladium−Hydride Bond: Computational Evidence for Two Nearly Isoenergetic Pathways. *Journal of the American Chemical Society* **2007,** *129* (14), 4410-4422.

17. Kryatov, S. V.; Rybak-Akimova, E. V.; Schindler, S., Kinetics and Mechanisms of Formation and Reactivity of Non-heme Iron Oxygen Intermediates. *Chemical Reviews* **2005,** *105* (6), 2175-2226.

18. Konnick, M. M.; Guzei, I. A.; Stahl, S. S., Characterization of Peroxo and Hydroperoxo Intermediates in the Aerobic Oxidation of *N*-Heterocyclic-Carbene-Coordinated Palladium(0). *Journal of the American Chemical Society* **2004,** *126* (33), 10212-10213.

19. Valentine, J. S., Dioxygen Ligand in Mononuclear Group VIII Transition Metal Complexes. *Chemical Reviews* **1973,** *73* (3), 235-245.

20. Würtele, C.; Gaoutchenova, E.; Harms, K.; Holthausen, M. C.; Sundermeyer, J.; Schindler, S., Crystallographic Characterization of a Synthetic 1:1 End-On Copper Dioxygen Adduct Complex. *Angewandte Chemie International Edition* **2006,** *45* (23), 3867-3869.

21. Ashley, D. C.; Brinkley, D. W.; Roth, J. P., Oxygen Isotope Effects as Structural and Mechanistic Probes in Inorganic Oxidation Chemistry. *Inorganic Chemistry* **2010,** *49* (8), 3661-3675.

22. Popp, B. V.; Wendlandt, J. E.; Landis, C. R.; Stahl, S. S., Reaction of Molecular Oxygen with an NHC-Coordinated Pd^0 Complex: Computational Insights and Experimental Implications. *Angewandte Chemie International Edition* **2007,** *46* (4), 601-604.

23. Germain, M. E.; Temprado, M.; Castonguay, A.; Kryatova, O. P.; Rybak-Akimova, E. V.; Curley, J. J.; Mendiratta, A.; Tsai, Y.-C.; Cummins, C. C.; Prabhakar, R.; McDonough, J. E.; Hoff, C. D., Coordination-Mode Control of Bound Nitrile Radical Complex Reactivity: Intercepting End-on Nitrile−Mo(III) Radicals at Low Temperature. *Journal of the American Chemical Society* **2009,** *131* (42), 15412-15423.

24. a) Bilgrien, C.; Davis, S.; Drago, R. S., The Selective Oxidation of Primary Alcohols to Aldehydes by Oxygen Employing a Trinuclear Ruthenium Carboxylate Catalyst. *Journal of the American Chemical Society* **1987,** *109* (12), 3786-3787. b) Tang, R.; Diamond, S. E.; Neary, N.; Mares, F., Homogeneous Catalytic Oxidation of Amines and Secondary Alcohols by Molecular Oxygen. *Journal of the Chemical Society, Chemical Communications* **1978,** 562-562. c) Matsushita, T.; Ebitani, K.; Kaneda, K., Highly Efficient Oxidation of Alcohols and Aromatic Compounds Catalysed by the Ru-Co-Al Hydrotalcite in the Presence of Molecular Oxygen. *Chemical Communications* **1999,** 265-266.

25. Iwahama, T.; Sakaguchi, S.; Nishiyama, Y.; Ishii, Y., Aerobic Oxidation of Alcohols to Carbonyl Compounds Catalyzed by n-hydroxyphthalimide (NHPI) Combined with Co(acac)$_3$. *Tetrahedron Letters* **1995,** *36* (38), 6923-6926.

26. a) Munakata, M.; Nishibayashi, S.; Sakamoto, H., Copper(I) Complex-catalysed Reduction of Dioxygen to Water and Oxidation of Alcohols: a Model of Copper(I)-containing Oxidase. *Journal of the Chemical Society, Chemical Communications* **1980,** 219-220. b) Wang, Y.; DuBois, J. L.; Hedman, B.; Hodgson, K. O.; Stack, T. D. P., Catalytic Galactose Oxidase Models: Biomimetic Cu(II)-Phenoxyl-Radical Reactivity. *Science* **1998,** *279* (5350), 537-540.

27. Bäeckvall, J. E., Palladium in Some Selective Oxidation Reactions. *Accounts of Chemical Research* **1983,** *16* (9), 335-342.

28. Osborn, J. A.; Jardine, F. H.; Young, J. F.; Wilkinson, G., The Preparation and Properties of Tris(triphenylphosphine)halogenorhodium(I) and Some Reactions Thereof Including Catalytic Homogeneous Hydrogenation of Olefins and Acetylenes and Their Derivatives. *Journal of the Chemical Society A: Inorganic, Physical, Theoretical* **1966,** 1711-1732.

29. Wanzlick, H. W.; Schönherr, H. J., Direct Synthesis of a Mercury Salt-Carbene Complex. *Angewandte Chemie International Edition in English* **1968,** *7* (2), 141-142.

30. a) Arduengo, A. J.; Harlow, R. L.; Kline, M., A Stable Crystalline Carbene. *Journal of the American Chemical Society* **1991,** *113* (1), 361-363. b) Arduengo, A. J.; Gamper, S. F.; Calabrese, J. C.; Davidson, F., Low-Coordinate Carbene Complexes of Nickel(0) and Platinum(0). *Journal of the American Chemical Society* **1994,** *116* (10), 4391-4394.

31. a) Kantchev, E. A. B.; O'Brien, C. J.; Organ, M. G., Palladium Complexes of N-Heterocyclic Carbenes as Catalysts for Cross-Coupling Reactions—A Synthetic Chemist's Perspective. *Angewandte Chemie International Edition* **2007,** *46* (16), 2768-2813. b) Peris, E.; Crabtree, R. H., Recent Homogeneous Catalytic Applications of Chelate and Pincer *N*-heterocyclic Carbenes. *Coordination Chemistry Reviews* **2004,** *248* (21–24), 2239-2246. c) Herrmann, W. A., N-Heterocyclic Carbenes: A New Concept in Organometallic Catalysis. *Angewandte Chemie International Edition* **2002,** *41* (8), 1290-1309.

32. Herrmann, W. A.; Köcher, C., *N*-Heterocyclic Carbenes. *Angewandte Chemie International Edition in English* **1997,** *36* (20), 2162-2187.

33. a) Hu, X.; Castro-Rodriguez, I.; Olsen, K.; Meyer, K., Group 11 Metal Complexes of N-Heterocyclic Carbene Ligands: Nature of the MetalCarbene Bond. *Organometallics* **2004,** *23* (4), 755-764. b) Nemcsok, D.; Wichmann, K.; Frenking, G., The Significance of π Interactions in Group 11 Complexes with *N*-Heterocyclic Carbenes. *Organometallics* **2004,** *23* (15), 3640-3646.

34. Khramov, D. M.; Rosen, E. L.; Er, J. A. V.; Vu, P. D.; Lynch, V. M.; Bielawski, C. W., *N*-Heterocyclic Carbenes: Deducing σ- and π-contributions in Rh-catalyzed Hydroboration and Pd-catalyzed Coupling Reactions. *Tetrahedron* **2008,** *64* (29), 6853-6862.

35. Fortman, G. C.; Scott, N. M.; Linden, A.; Stevens, E. D.; Dorta, R.; Nolan, S. P., Unusual Reactivities of *N*-heterocyclic Carbenes upon Coordination to the Platinum(II)-dimethyl Moiety. *Chemical Communications* **2010,** *46* (7), 1050-1052.

36. For reviews, see: a) reference 8. b) Nishimura, T.; Uemura, S. Synlett **2004**, 201–216. c) Sigman, M. S.; Jensen, D. R. *Accounts of Chemical Research* **2006**, 39, 221–229. d) Gligorich, K. M.; Sigman, M. S. *Chemical Communications* **2009**, 3854–3867. e) Chen, X.; Engle, K. M.; Wang, D.-H.; Yu, J.-Q. *Angewandte Chemie International Edition* **2009**, 48, 5094–5115. f) Konnick, M. M.; Decharin, N.; Popp, B. V.; Stahl, S. S., O_2 Insertion into a Palladium(II)-hydride Bond: Observation of Mechanistic Crossover between HX-reductive-elimination and Hydrogen-atom-abstraction Pathways. *Chemical Science* **2011,** *2* (2), 326-330. g) For a review on the role of NHC in late transition metal catalysis, see: Díez-Gonzalez, S.; Marion, N.; Nolan, S. P. *Chemical Reviews* **2009**, 109, 3612–3676.

37. a) Sheldon, R. A.; Arends, I.; Hanfeld, U. Green Chemistry and Catalysis; Wiley-VCH:Weinheim, Germany, **2007**; Chapter 4, pp18-23. b) van Leeuwen, P. V. N. M. Homogeneous Catalysis: Understanding the Art; Kluwer: Dordrecht, The Netherlands, **2004**; Chapter 15. c) Stahl, S. S. *Science* **2005**, 309, 1824–1826.

38. Yoshida, T.; Otsuka, S., Reactions of Two-coordinate Phosphine Platinum(0) and Palladium(0) Compounds. Ligand Exchange and Reactivities Toward Small Molecules. *Journal of the American Chemical Society* **1977,** *99* (7), 2134-2140.

39. Stahl, S. S.; Thorman, J. L.; Nelson, R. C.; Kozee, M. A., Oxygenation of Nitrogen-Coordinated Palladium(0): Synthetic, Structural, and Mechanistic Studies and Implications for Aerobic Oxidation Catalysis. *Journal of the American Chemical Society* **2001,** *123* (29), 7188-7189.

40. a) ref 39. b) Clegg, W.; Eastham, G. R.; Elsegood, M. R. J.; Heaton, B. T.; Iggo, J. A.; Tooze, R. P.; Whyman, R.; Zacchini, S., Synthesis and Reactivity of Palladium Hydrido-solvento Complexes, Including a Key Intermediate in the Catalytic Methoxycarbonylation of Ethene to Methyl Propanoate. *Journal of the Chemical Society, Dalton Transactions* **2002,** 3300-3308. c) Yamashita, M.; Goto, K.; Kawashima, T., Fixation of Both O_2 and CO_2 from Air by a Crystalline Palladium Complex Bearing N-Heterocyclic Carbene Ligands. *Journal of the American Chemical Society* **2005,** *127* (20), 7294-7295. d) Fantasia, S.; Nolan, S. P., A General Synthetic Route to Mixed NHC–Phosphane Palladium(0) Complexes (NHC=N-Heterocyclic Carbene). *Chemistry – A European Journal* **2008,** *14* (23), 6987-6993. e) Fantasia, S.; Egbert, J. D.; Jurčík, V.; Cazin, C. S. J.; Jacobsen, H.; Cavallo, L.; Heinekey, D. M.; Nolan, S. P., Activation of Hydrogen by Palladium(0): Formation of the Mononuclear Dihydride Complex trans-

[Pd(H)$_2$(IPr)(PCy$_3$)]. *Angewandte Chemie International Edition* **2009,** *48* (28), 5182-5186. f) Labios, L. A.; Millard, M. D.; Rheingold, A. L.; Figueroa, J. S., Bond Activation, Substrate Addition and Catalysis by an Isolable Two-Coordinate Pd(0) Bis-Isocyanide Monomer. *Journal of the American Chemical Society* **2009,** *131* (32), 11318-11319. g) Sergeev, A. G.; Neumann, H.; Spannenberg, A.; Beller, M., Synthesis and Catalytic Applications of Stable Palladium Dioxygen Complexes. *Organometallics* **2010,** *29* (15), 3368-3373.

41. Vaska, L., Reversible Activation of Covalent Molecules by Transition-metal Complexes. The Role of the Covalent Molecule. *Accounts of Chemical Research* **1968,** *1* (11), 335-344.

42. CCDC-800882 and CCDC-800883 contain the supplementary crystallographic data for this contribution. These data can be obtained free of charge from The Cambridge Crystallographic Data Centre via www.ccdc.cam.ac.uk/data_request/cif.

43. Crystal data: PdO$_4$N$_4$ C$_{54}$H$_{72}$•1/2C$_6$H$_{14}$, M$_r$ = 990.64, monoclinic, space group P21/c, a = 13.766(4) Å, b = 15.624(4) Å, c = 25.915(8) Å, β = 103.647(7)^o, V = 5416(3) Å^3, Z = 4, T = 93 K, Mo Kα = 0.71073 Å. GOF = 1.138, no. parameters = 595, 2 Θ max = 50°. The final R1(F^2) was 0.1261 for 6664 reflections, I > 2 σ (I).

44. a) Talsi, E. P.; Babenko, V. P.; Likholobov, V. A.; Nekipelov, V. M.; Chinakov, V. D., A New Superoxo-complex of Palladium that Oxidizes Alkenes to Epoxides. *Journal of the Chemical Society, Chemical Communications* **1985,** 1768-1769. b) Talsi, E. P.; Babenko, V. P.; Shubin, A. A.; Chinakov, V. D.; Nekipelov, V. M.; Zamaraev, K. I., Formation, Structure, and Reactivity of Palladium Superoxo Complexes. *Inorganic Chemistry* **1987,** *26* (23), 3871-3878. c) Fiallo, M. M. L.; Garnier-Suillerot, A., Interaction of the Antitumor Drug Streptonigrin with Palladium(II) Ions. Evidence of the Formation of a Superoxo-palladium(II)-streptonigrin Complex. *Inorganic Chemistry* **1990,** *29* (5), 893-897.

45. Huacuja, R.; Graham, D. J.; Fafard, C. M.; Chen, C.-H.; Foxman, B. M.; Herbert, D. E.; Alliger, G.; Thomas, C. M.; Ozerov, O. V., Reactivity of a Pd(I)−Pd(I) Dimer with O2: Monohapto Pd Superoxide and Dipalladium Peroxide in Equilibrium. *Journal of the American Chemical Society* **2011,** *133* (11), 3820-3823.

46. Cai, X.; Majumdar, S.; Fortman, G. C.; Cazin, C. S. J.; Slawin, A. M. Z.; Lhermitte, C.; Prabhakar, R.; Germain, M. E.; Palluccio, T.; Nolan, S. P.; Rybak-Akimova, E. V.; Temprado, M.; Captain, B.; Hoff, C. D., Oxygen Binding to [Pd(L)(L′)] (L= NHC, L′ = NHC or PR$_3$, NHC = *N*-Heterocyclic Carbene). Synthesis and Structure of a Paramagnetic *trans*-[Pd(NHC)$_2$(η^1-O$_2$)$_2$] Complex. *Journal of the American Chemical Society* **2011,** *133* (5), 1290-1293.

47. Data for H-O$_2$H BDE in the gas phase were computed from data available at http://webbook.nist.gov. Data for H-Mo(CO)$_3$Cp were taken from Landrum, J. T.; Hoff, C. D., The Heats of Hydrogenation of the Metal—metal Bonded Complexes [M(CO)$_3$C$_5$H$_5$]$_2$ (M = Cr, Mo, W). *Journal of Organometallic Chemistry* **1985,** *282* (2), 215-224.

48. Crystal data: PdO$_4$N$_4$C$_{54}$H$_{78}$, M$_r$ = 953.60, triclinic, space group P$\bar{1}$, a = 12.2884(5) Å, b = 12.3340(5) Å, c = 17.2479(7) Å, α = 82.982(1)°, β = 87.966(1) °, γ = 89.015(1)°, V = 2592.74(18) Å^3, Z = 2, T = 296 K, Mo KR = 0.71073 Å. GOF = 1.021, no. parameters = 586, 2Θmax = 57°. The final R1(F^2) was 0.0375 for 10468 reflections, I >2σ(I).

49. For a selection of monohydroperoxide structurally characterized complexes, see the following. a) For Pd-NHC: Konnick, M. M.; Gandhi, B. A.; Guzei, I. A.; Stahl, S. S., Reaction of Molecular Oxygen with a PdII– Hydride To Produce a PdII–Hydroperoxide: Acid Catalysis and Implications for Pd-Catalyzed Aerobic Oxidation Reactions. *Angewandte Chemie International Edition* **2006,** *45* (18), 2904-2907. b) For Pd: Denney, M. C.; Smythe, N. A.; Cetto, K. L.; Kemp, R. A.; Goldberg, K. I., Insertion of Molecular Oxygen into a Palladium(II) Hydride Bond. *Journal of the American Chemical Society* **2006,** *128* (8), 2508-2509. For Pt: c) Look, J. L.; Wick, D. D.; Mayer, J. M.; Goldberg, K. I., Autoxidation of Platinum(IV) Hydrocarbyl Hydride Complexes To Form Platinum(IV) Hydrocarbyl Hydroperoxide Complexes. *Inorganic Chemistry* **2009,** *48* (4), 1356-1369. d) Rostovtsev, V. V.; Henling, L. M.; Labinger, J. A.; Bercaw, J. E., Structural and Mechanistic Investigations of the Oxidation of Dimethylplatinum(II) Complexes by Dioxygen. *Inorganic Chemistry* **2002,** *41* (14), 3608-3619.

50. Fortman, G. C.; Isrow, D.; McDonough, J. E.; Schleyer, P. v. R.; Schaefer, H. F.; Scott, B.; Kubas, G. J.; Kégl, T. s.; Ungváry, F.; Hoff, C. D., Kinetic and Thermodynamic Studies of the Reactivity of (Trimethylsilyl)diazomethane with HMo(CO)$_3$(C$_5$R$_5$) (R = H, Me). Estimation of the Mo−N$_2$CH$_2$SiMe$_3$ Bond Strength and Experimental Determination of the Enthalpy of Formation of (Trimethylsilyl)diazomethane. *Organometallics* **2008,** *27* (19), 4873-4884.

51. Bain, G. A.; Berry, J. F., Diamagnetic Corrections and Pascal's Constants. *Journal of Chemical Education* **2008,** *85* (4), 532.

52. Gaussian 03, Revision C.02, Frisch, M. J.; Trucks, G. W.; Schlegel, H. B.; Scuseria, G. E.; Robb, M. A.; Cheeseman, J. R.; Montgomery, Jr., J. A.; Vreven, T.; Kudin, K. N.; Burant, J. C.; Millam, J. M.; Iyengar, S. S.; Tomasi, J.; Barone, V.; Mennucci, B.; Cossi, M.; Scalmani, G.; Rega, N.; Petersson, G. A.; Nakatsuji, H.; Hada, M.; Ehara, M.; Toyota, K.; Fukuda, R.; Hasegawa, J.; Ishida, M.; Nakajima, T.; Honda, Y.; Kitao, O.; Nakai, H.; Klene, M.; Li, X.; Knox, J. E.; Hratchian, H. P.; Cross, J. B.; Bakken, V.; Adamo, C.; Jaramillo, J.; Gomperts, R.; Stratmann, R. E.; Yazyev, O.; Austin, A. J.; Cammi, R.; Pomelli, C.; Ochterski, J. W.; Ayala, P. Y.; Morokuma, K.; Voth, G. A.; Salvador, P.; Dannenberg, J. J.; Zakrzewski, V. G.; Dapprich, S.; Daniels, A. D.; Strain, M. C.; Farkas, O.; Malick, D. K.; Rabuck, A. D.; Raghavachari, K.; Foresman, J. B.; Ortiz, J. V.; Cui, Q.; Baboul, A. G.; Clifford, S.; Cioslowski, J.; Stefanov, B. B.; Liu, G.; Liashenko, A.;

Piskorz, P.; Komaromi, I.; Martin, R. L.; Fox, D. J.; Keith, T.; Al-Laham, M. A.; Peng, C. Y.; Nanayakkara, A.; Challacombe, M.; Gill, P. M. W.; Johnson, B.; Chen, W.; Wong, M. W.; Gonzalez, C.; and Pople, J. A.; Gaussian, Inc., Wallingford CT, 2004.

53. a) Becke, A. D., Density-functional Exchange-energy Approximation with Correct Asymptotic Behavior. *Phys. Rev. A.* **1988,** *38*, 3098-3100; b) Hay, P. J., and Wadt, W. R., Ab Initio Effective Core Potentials for Molecular Calculations. Potentials for the Transition Metal Atoms Sc to Hg. *J. Chem. Phys.* **1985,** *82*, 270-283; c) Becke, A. D. J., Density-functional Thermochemistry. III. The Role of Exact Exchange. *Chemical Physics.* **1993,** *98*, 5648-5652.

54. CrystalClear Version 2.0. Rigaku Corporation, Akishima, Tokyo, Japan, 2009.

55. Sheldrick, G. M. *Acta Crystallographica*. **2008,** A64, 112–122.

56. Apex2 Version 2.2-0 and SAINT+ Version 7.46A; Bruker Analytical X-ray System, Inc., Madison, Wisconsin, USA, **2007**.

57. Sheldrick, G. M. SHELXTL Version 6.1; Bruker Analytical X-ray Systems, Inc., Madison, Wisconsin, USA, **2000**.

58. Maiti, D.; Lee, D.-H.; Gaoutchenova, K.; Würtele, C.; Holthausen, M. C.; Narducci Sarjeant, A. A.; Sundermeyer, J.; Schindler, S.; Karlin, K. D., Reactions of a Copper(II) Superoxo Complex Lead to C-H and O-H Substrate Oxygenation: Modeling Copper-Monooxygenase C-H Hydroxylation. *Angewandte Chemie International Edition* **2008,** *47* (1), 82-85.

59. Cramer, C. J.; Tolman, W. B., Mononuclear Cu–O_2 Complexes: Geometries, Spectroscopic Properties, Electronic Structures, and Reactivity. *Accounts of Chemical Research* **2007,** *40* (7), 601-608.

60. Unno, M.; Chen, H.; Kusama, S.; Shaik, S.; Ikeda-Saito, M., Structural Characterization of the Fleeting Ferric Peroxo Species in Myoglobin: Experiment and Theory. *Journal of the American Chemical Society* **2007,** *129* (44), 13394-13395.

61. De Waal, D. J. A.; Gerber, T. I. A.; Louw, W. J.; Van Eldik, R., Kinetics and Mechanism of the Dioxygen Uptake of the Four-coordinate (X = Cl) and Five-coordinate (X = I, SCN, PPh_3) Complexes Ir(cod) (phen)X. *Inorganic Chemistry* **1982,** *21* (5), 2002-2006.

62. Aboelella, N. W.; Kryatov, S. V.; Gherman, B. F.; Brennessel, W. W.; Young, V. G.; Sarangi, R.; Rybak-Akimova, E. V.; Hodgson, K. O.; Hedman, B.; Solomon, E. I.; Cramer, C. J.; Tolman, W. B., Dioxygen Activation at a Single Copper Site: Structure, Bonding, and Mechanism of Formation of 1:1 Cu−O_2 Adducts. *Journal of the American Chemical Society* **2004,** *126* (51), 16896-16911.

63. Wever, R. In Vanadium: Biochemical and Molecular Biological Approaches; Michibata, H., Ed.; Springer: New York, **2012**; pp 95– 125.

64. Conte, V.; Coletti, A.; Floris, B.; Licini, G.; Zonta, C., Mechanistic Aspects of Vanadium Catalysed Oxidations with Peroxides. *Coordination Chemistry Reviews* **2011,** *255* (19–20), 2165-2177.

65. Butler, A.; Clague, M. J.; Meister, G. E., Vanadium Peroxide Complexes. *Chemical Reviews* **1994,** *94* (3), 625-638.

66. (a) Kirk Egdal, R.; Bond, A. D.; McKenzie, C. J., Air Oxidation of Divanadium(IV) Complexes. *Dalton Transactions* **2009,** 3833-3839. (b) Waidmann, C. R.; DiPasquale, A. G.; Mayer, J. M., Synthesis and Reactivity of Oxo-Peroxo-Vanadium(V) Bipyridine Compounds. *Inorganic Chemistry* **2010,** *49* (5), 2383-2391.

67. (a) Arzoumanian, H.; Petrignani, J. F.; Pierrot, M.; Ridouane, F.; Sanchez, J., Preparation of an Oxoperoxocyanomolybdate(VI) Complex by Dioxygen Oxidation of an Oxocyanomolybdate(IV) Anion. Structure and Reactivity toward Phosphines and Olefins. *Inorganic Chemistry* **1988,** *27* (19), 3377-3381. (b) Hagadorn, J. R.; Arnold, J., Preparation of Complexes Containing TiE, $Ti_2(\mu\text{-}E)_2$, and $Ti(\eta^2\text{-}E_2)$ (E = O, S) Functionalities from a Reactive Titanium Dinitrogen Complex. *Inorganic Chemistry* **1997,** *36* (14), 2928-2929. (c) Hanna, T. E.; Lobkovsky, E.; Chirik, P. J., Dihydrogen and Silane Addition to Base-Free, Monomeric Bis(cyclopentadienyl)titanium Oxides. *Inorganic Chemistry* **2007,** *46* (7), 2359-2361. (d) Jeske, P.; Haselhorst, G.; Weyhermueller, T.; Wieghardt, K.; Nuber, B., Synthesis and Characterization of Mononuclear Octahedral Titanium(IV) Complexes Containing Ti:O, $Ti(O_2)$, and $Ti(OCH_3)x$ (x = 1-3) Structural Units. *Inorganic Chemistry* **1994,** *33* (11), 2462-2471. (e) Lyashenko, G.; Saischek, G.; Pal, A.; Herbst-Irmer, R.; Mosch-Zanetti, N. C., Molecular Oxygen Activation by a Molybdenum(iv) Monooxo Bis(β-ketiminato) Complex. *Chemical Communications* **2007,** 701-703. (f) Matoga, D.; Szklarzewicz, J.; Mikuriya, M., $[PPh_4]_3[W(CN)_7(O_2)]\cdot 4H_2O$ as the Representative of the $[M(L)_7(LL)]$ Class for Nine-Coordinate Complexes. *Inorganic Chemistry* **2006,** *45* (18), 7100-7104. (g) Matoga, D.; Szklarzewicz, J.; Samotus, A.; Burgess, J.; Fawcett, J.; Russell, D. R., Preparation and Characterisation of $[M(CN)_4O(pz)]_2-$ complexes (M=Mo or W) and Their Reactivity towards Molecular Oxygen. *Polyhedron* **2000,** *19* (12), 1503-1509. (h) Qin, K.; Incarvito, C. D.; Rheingold, A. L.; Theopold, K. H., A Structurally Characterized Chromium(III) Superoxide Complex Features "Side-on" Bonding. *Angewandte Chemie International Edition* **2002,** *41* (13), 2333-2335. (i) Sofetis, A.; Fotopoulou, F.; Raptopoulou, C. P.; Zafiropoulos, T. F.; Perlepes, S. P.; Klouras, N., Reactions of Titanocene Dihalides with N,N′,N″-chelates: Preparation, X-ray Structure and Characterization of bis(chloro){2,6-bis[(3,5-dimethyl)pyrazol-1-yl]pyridine}$(\eta^2\text{-}$peroxo)titanium(IV). *Polyhedron* **2009,** *28* (15), 3356-3360. (j) Stanciu, C.; Jones, M. E.; Fanwick, P. E.; Abu-Omar, M. M., Multi-electron Activation of Dioxygen on Zirconium(IV) to Give an Unprecedented Bisperoxo Complex. *Journal of the American Chemical Society* **2007,** *129* (41), 12400-12401. (k) Van Asselt, A.; Trimmer, M. S.; Henling, L. M.; Bercaw, J. E., Dioxygen-derived Peroxo-alkyl Complexes of

Permethyltantalocene. Structural Characterization of (η ^{5}-C$_5$Me$_5$)$_2$Ta(η ^{2}-O$_2$)(CH$_2$C$_6$H$_5$) and Acid-catalyzed Rearrangement to Oxo-alkoxide Derivatives. *Journal of the American Chemical Society* **1988,** *110* (24), 8254-8255. (l) Yokoyama, A.; Han, J. E.; Cho, J.; Kubo, M.; Ogura, T.; Siegler, M. A.; Karlin, K. D.; Nam, W., Chromium(IV)–Peroxo Complex Formation and Its Nitric Oxide Dioxygenase Reactivity. *Journal of the American Chemical Society* **2012,** *134* (37), 15269-15272.

68. (a) Groysman, S.; Goldberg, I.; Goldschmidt, Z.; Kol, M., Vanadium(III) and Vanadium(V) Amine Tris(Phenolate) Complexes. *Inorganic Chemistry* **2005,** *44* (14), 5073-5080. (b) Liu, Z.; Anson, F. C., Schiff Base Complexes of Vanadium(III, IV, V) as Catalysts for the Electroreduction of O$_2$ to H$_2$O in Acetonitrile. *Inorganic Chemistry* **2001,** *40* (6), 1329-1333. (c) Tsuchida, E.; Oyaizu, K., Oxovanadium(III–V) mononuclear complexes and their linear assemblies bearing tetradentate Schiff base ligands: structure and reactivity as multielectron redox catalysts. *Coordination Chemistry Reviews* **2003,** *237* (1–2), 213-228.

69. Palluccio, T.; Rybak-Akimova, E. V.; Cai, X.; Majumdar, S.; Temprado, M.; Silvia, J. S.;Cozzolino, A. F.; Tofan, D.; Cummins, C. C.; Captain, B.; Hoff, C. D., Oxygen Atom Transfer from N-oxides to a Vanadium(III) Complex: Enhanced Reaction Rates for Organic Adducts of Nitrous Oxide and Mesityl Nitrile Oxide. *J. Am. Chem. Soc* **2012**, submitted ja-2012-04597w.

70. Tatiersky, J.; Pacigová, S.; Sivák, M.; Schwendt, P. J., Monoperoxidovanadium(V) Complexes: Synthesis, Structure and Solution Properties. *Journal of the Argentine Chemical Society* **2009**, 97, 181– 198.

71. Sergienko, V. S., Structural Characteristics of Peroxo Complexes of Group IV and V Transition Metals. Review. *Crystallogr. Rep.* **2004,** *49* (6), 907-929.

72. (a) Grzywa, M.; Łasocha, W., Crystal structure of potassium and ammonium tetraperoxovanadates (V). *Zeitschrift für Kristallographie - Crystalline Materials* **2007,** *222* (2), 95-98. (b) Won, T.-J.; Barnes, C. L.; Schlemper, E. O.; Thompson, R. C., Two Crystal Structures Featuring the Tetraperoxovanadate(V) Anion and a Brief Reinvestigation of Peroxovanadate Equilibria in Neutral and Basic Solutions. *Inorganic Chemistry* **1995,** *34* (17), 4499-4503.

73. (a) Cambridge Structural Database, version 5. 3, Nov **2011**, with 586977 entries. (b) Allen, F. H., The Cambridge Structural Database: a Quarter of a Million Crystal Structures and Rising. *Acta Crystallographica Section B* **2002**, B58, 380– 388.

74. (a) Desiraju, G.; Steiner, T. The Weak Hydrogen Bond; Oxford University Press: Oxford, U.K., **1999**. (b) Weinhold, F.; Klein, R. A., What is a Hydrogen Bond? Mutually Consistent Theoretical and Experimental Criteria for Characterizing H-bonding Interactions. *Molecular Physics* **2012,** *110* (9-10), 565-579.

75. (a) Rybak-Akimova, E. V.; Marek, K.; Masarwa, M.; Busch, D. H., The Dynamics of Formation of the O_2-Co^{II} bond in the Cobalt(II) Cyclidene Complexes. *Inorganica Chimica Acta* **1998,** *270* (1–2), 151-161. (b) Fry, H. C.; Scaltrito, D. V.; Karlin, K. D.; Meyer, G. J., The Rate of O_2 and CO Binding to a Copper Complex, Determined by a "Flash-and-Trap" Technique, Exceeds that for Hemes. *Journal of the American Chemical Society* **2003,** *125* (39), 11866-11871.

76. Mayer, I., Bond order and valence: Relations to Mulliken's population analysis. *International Journal of Quantum Chemistry* **1984,** *26* (1), 151-154.

77. Glendening, E. D.; Badenhoop, J. K.; Weinhold, F., Natural resonance theory: III. Chemical applications. *Journal of Computational Chemistry* **1998,** *19* (6), 628-646.

78. Odom, A. L.; Cummins, C. C.; Protasiewicz, J. D., Nitric Oxide Cleavage: Synthesis of Terminal Chromium(VI) Nitrido Complexes via Nitrosyl Deoxygenation. *Journal of the American Chemical Society* **1995,** *117* (24), 6613-6614.

79. Yang, W.; Parr, R. G.; Pucci, R., Electron Density, Kohn–Sham Frontier Orbitals, and Fukui Functions. *Journal of Chemical Physics*. **1984**, 81, 2862.

80. (a) Leung, W.-H.; Chim, J. L. C.; Williams, I. D.; Wong, W.-T., Reactions of Nitridorhenium(V) and Osmium(VI) Complexes with Acylating Agents. *Inorganic Chemistry* **1999,** *38* (12), 3000-3005. (b) Clough, C. R.; Greco, J. B.; Figueroa, J. S.; Diaconescu, P. L.; Davis, W. M.; Cummins, C. C., Organic Nitriles from Acid Chlorides: An Isovalent N for (O)Cl Exchange Reaction Mediated by a Tungsten Nitride Complex. *Journal of the American Chemical Society* **2004,** *126* (25), 7742-7743. (c) Figueroa, J. S.; Piro, N. A.; Clough, C. R.; Cummins, C. C., A Nitridoniobium(V) Reagent That Effects Acid Chloride to Organic Nitrile Conversion: Synthesis via Heterodinuclear (Nb/Mo) Dinitrogen Cleavage, Mechanistic Insights, and Recycling. *Journal of the American Chemical Society* **2005,** *128* (3), 940-950.

81. (a) Thomas, S.; Lim, P. J.; Gable, R. W.; Young, C. G., Acylimido Complexes of Tungsten(IV) Formed by Oxygen Atom Transfer to Nitrile-$\kappa^2 N,C$ Complexes. *Inorganic Chemistry* **1998,** *37* (3), 590-593. (b) J. Nielson, A.; A. Hunt, P.; E. F. Rickard, C.; Schwerdtfeger, P., d^2 Complexes of Tungsten Containing *p*-toluonitrile as a Four- or Two-electron Donor and Oxidative Addition Giving the Two-electron Donor Acylimido Ligand $NCOC_6H_4Me$-4. *Journal of the Chemical Society, Dalton Transactions* **1997,** 3311-3318.

82. Brask, J. K.; Fickes, M. G.; Sangtrirutnugul, P.; Dura-Vila, V.; Odom, A. L.; Cummins, C. C., Niobium and Vanadium Iminophosphinimide Complexes. *Chemical Communications* **2001,** 1676-1677.

83. Fickes, M. G. Synthesis and Reactivity of Vanadium and Niobium Complexes Containing Sterically Demanding Amido Ligands, Massachusetts Institute of Technology, **1998**, p. 284.

84. Brask, J. K.; Fickes, M. G.; Sangtrirutnugul, P.; Dura-Vila, V.; Odom, A. L.; Cummins, C. C., Niobium and Vanadium Iminophosphinimide Complexes. *Chemical Communications* **2001,** 1676-1677.

85. In CRC Handbook of Chemistry and Physics (Internet Version); Haynes, W. M., Ed.; CRC Press/Taylor and Francis: Boca Raton, FL, **2012**.

86. Battino, R.; Rettich, T. R.; Tominaga, T. J., The Solubility of Oxygen and Ozone in Liquids. *Journal of Physical and Chemical Reference Data* **1983**, 12, 163.

87. Becke, A. D. J., Density-functional Thermochemistry. III. The Role of Exact Exchange. *Journal of Chemical Physics* **1993**, 98, 5648–5652.

88. Perdew, J. P., Density-functional Approximation for the Correlation Energy of the Inhomogeneous Electron Gas. *Physical Review B* **1986**, 33, 8822.

89. Frisch, M. J. et al. Gaussian 09, revision B.01 **2010**.

90. Wadt, W. R.; Hay, P. J., Ab *Initio* Effective Core Potentials for Molecular Calculations. Potentials for Main Group Elements Na to Bi. *Journal of Chemical Physics* **1985**, 82, 284.

91. Hay, P. J.; Wadt, W. R., *Ab Initio* Effective Core Potentials for Molecular Calculations. Potentials for the Transition Metal Atoms Sc to Hg. *Journal of Chemical Physics* **1985**, 82, 270.

92. Hay, P. J.; Wadt, W. R., *Ab initio* Effective Core Potentials for Molecular Calculations. Potentials for K to Au Including the Outermost Core Orbitals. *Journal of Chemical Physics* **1985**, 82, 299.

93. Dunning Jr., T. H.; Hay, P. J. Modern Theoretical Chemistry, Vol. 3; Schaefer III, H. F., Ed.; Plenum: New York, **1976**; pp. 1–28.

94. Martin, J. M. L.; Sundermann, A., Correlation Consistent Valence Basis Sets for Use with the Stuttgart–Dresden–Bonn Relativistic Effective Core Potentials: The Atoms Ga–Kr and In–Xe. *Journal of Chemical Physics* **2001**, 114.

95. Dolg, M.; Wedig, U.; Stoll, H.; Preuss, H., Energy Adjusted *Ab Initio* Pseudopotentials for the First Row Transition Elements. *Journal of Chemical Physics* **1987**, 86, 866.

96. Boys, S. F.; Bernardi, F., The Calculation of Small Molecular Interactions by the Differences of Separate Total Energies. Some Procedures with Reduced Errors. *Molecular Physics* **1970**, 19, 553.

97. Simon, S.; Duran, M.; Dannenberg, J. J. How does Basis Set Superposition Error Change the Potential Surfaces for Hydrogen-bonded Dimers? *Journal of Chemical Physics* **1996**, 105, 11024.

98. Neese, F. ORCA, Version 2.8 **2010**.

99. Perdew, J. P.; Wang, Y., Accurate and Simple Analytic Representation of the Electron-gas Correlation Energy. *Physical Review B* **1992**, 45, 13244.

100. van Lenthe, E.; Baerends Evert, J.; Snijders, J. G., Relativistic Regular Two-component Hamiltonians. *Journal of Chemical Physics* **1993**, 99, 4597–4610.

5.4101. Heully, J. L.; Lindgren, I.; Lindroth, E.; Lundqvist, S.; Maartensson-Pendrill, A. M., Diagonalisation of the Dirac Hamiltonian as a Basis for a Relativistic Many-body Procedure. *Journal of Physics B: Atomic, Molecular and Optical Physics* **1986**, 19, 2799–2815.

102. Pantazis, D. A.; Chen, X.-Y.; Landis, C. R.; Neese, F., All-Electron Scalar Relativistic Basis Sets for Third-Row Transition Metal Atoms. *Journal of Chemical Theory and Computation* **2008,** *4* (6), 908-919.

103. Schaefer, A.; Horn, H.; Ahlrichs, R., Fully optimized contracted Gaussian basis sets for atoms Li to Kr. *Journal of Chemical Physics* **1992**, 97, 2571–2577.

104. Glendening, E. D.; Badenhoop, J. K.; Reed, A. E.; Carpenter, J. E.; Bohmann, J. A.; Morales, C. M.; Weinhold, F. NBO 5.0 **2001**.

105. Glendening, E. D.; Badenhoop, J. K.; Weinhold, F. *Journal of Computational Chemistry* **1998**, 19, 628-646.

106. Glendening, E. D.; Weinhold, F. *Journal of Computational Chemistry* **1998**, 19, 593–609.

107. Glendening, E. D.; Weinhold, F. *Journal of Computational Chemistry* **1998**, 19, 610–627.

108. Sheldrick, G. M. CELL_NOW **2003**.

109. Sheldrick, G. M. SHELX97 [Includes SHELXS97, SHELXL97, CIFTAB] - Programs for Crystal Structure Analysis, release 97-2 **1998**.

110. Sheldrick, G. M. SADABS: Programm for Empirical Absorption Correction of Area Detectors **1996**.

111. Sheldrick, G. M. TWINABS: Program for Performing Absorption Corrections to X-ray Diffraction Patterns Collected from Non-Merohedrally Twinned and Multiple Crystals **2002.**

112. Nam, W., Dioxygen Activation by Metalloenzymes and Models. *Accounts of Chemical Research* **2007,** *40* (7), 465-465.

113. Horváth, H. T; Anastas, P. T., Introduction: Green Chemistry. *Chemical Reviews* **2007,** *107* (6), 2167-2168

114. a) Parmon, V. N.; Panov, G. I.; Uriarte, A.; Noskov, A. S., Nitrous Oxide in Oxidation Chemistry and Catalysis: Application and Production. *Catalysis Today* **2005**, *100* (1–2), 115-131. b) Hintz, P. A.; Sowa, M. B.; Ruatta, S. A.; Anderson, S. L., Reactions of Boron Cluster Ions (B^+_n, *n*=2–24) with N_2O: NO Versus NN Bond Activation as a Function of Size. *Journal of Chemical Physics*. **1991**, 94, 6446.

115. a) Vaughan, G. A.; Rupert, P. B.; Hillhouse, G. L., Selective O-atom Transfer from Nitrous Oxide to Hydride and Aryl Ligands of Bis(pentamethylcyclopentadienyl)hafnium Derivatives. *Journal of the American Chemical Society* **1987,** *109* (18), 5538-5539. b) Vaughan, G. A.; Hillhouse, G. L.; Lum, R. T.; Buchwald, S. L.; Rheingold, A. L., Oxygen-atom Transfer from Nitrous Oxide. Synthesis and Structure of a Zirconocene oxametallacyclobutene Complex. *Journal of the American Chemical Society* **1988,** *110* (21), 7215-7217. c) Matsunaga, P. T.; Hillhouse, G. L.; Rheingold, A. L., Oxygen-atom Transfer from Nitrous Oxide to a Nickel Metallacycle. Synthesis, Structure, and Reactions of [cyclic] (2,2'-bipyridine)Ni(OCH₂CH₂CH₂CH₂). *Journal of the American Chemical Society* **1993,** *115* (5), 2075-2077. d) Koo, K.; Hillhouse, G. L.; Rheingold, A. L., Oxygen-Atom Transfer from Nitrous Oxide to an Organonickel(II) Phosphine Complex. Syntheses and Reactions of New Nickel(II) Aryloxides and the Crystal Structure of [cyclic] (Me₂PCH₂CH₂PMe₂)Ni(O-*o*-C₆H₄CMe₂CH₂). *Organometallics* **1995,** *14* (1), 456-460. e) Harrold, N. D.; Waterman, R.; Hillhouse, G. L.; Cundari, T. R., Group-Transfer Reactions of Nickel−Carbene and −Nitrene Complexes with Organoazides and Nitrous Oxide that Form New C=N, C=O, and N=N Bonds. *Journal of the American Chemical Society* **2009,** *131* (36), 12872-12873.

116. a) Tuan, D. F. T.; Hoffmann, R., Nitrogen Atom vs. Oxygen Atom Linkage and σ vs. π Bonding in Transition-metal Complexes of Dinitrogen Oxide and Cyanate. *Inorganic Chemistry* **1985,** *24* (6), 871-876. b) Armor, J. N.; Taube, H., Formation and Reactions of [(NH₃)₅RuN₂O₂⁺]. *Journal of the American Chemical Society* **1969,** *91* (24), 6874-6876. c) Diamantis, A. A.; Sparrow, G. J., Nitrous Oxide Complexes: the Isolation of Pentammine(dinitrogen oxide)ruthenium(II) Tetrafluoroborate. *Journal of the Chemical Society D: Chemical Communications* **1970**, 819-820. d) Armor, J. N.; Taube, H., Evidence of a Binuclear Nitrous Oxide Complex of Ruthenium. *Journal of the Chemical Society D: Chemical Communications* **1971,** 287-288. e) Bottomley, F.; Brooks, W. V. F., Mode of Bonding of Dinitrogen Oxide (Nitrous Oxide) in (Dinitrogen oxide)pentaammineruthenium. *Inorganic Chemistry* **1977,** *16* (2), 501-502.

117. Piro, N. A.; Lichterman, M. F.; Harman, W. H.; Chang, C. J., A Structurally Characterized Nitrous Oxide Complex of Vanadium. *Journal of the American Chemical Society* **2011,** *133* (7), 2108-2111.

118. a) Otten, E.; Neu, R. C.; Stephan, D. W., Complexation of Nitrous Oxide by Frustrated Lewis Pairs. *Journal of the American Chemical Society* **2009,** *131* (29), 9918-9919. b) Neu, R. C.; Otten, E.; Stephan, D. W., Bridging Binding Modes of Phosphine-Stabilized Nitrous Oxide to $Zn(C_6F_5)_2$. *Angewandte Chemie International Edition* **2009,** *48* (51), 9709-9712.

119. Veige, A. S.; Slaughter, L. M.; Wolczanski, P. T.; Matsunaga, N.; Decker, S. A.; Cundari, T. R., Deoxygenations of $(silox)_3$WNO and R_3PO by $(silox)_3$M (M = V, Ta) and $(silox)_3$NbL (silox = $^tBu_3$SiO): Consequences of Electronic Effects. *Journal of the American Chemical Society* **2001,** *123* (26), 6419-6420.

120. Abu-Omar, M. M., Oxygen Atom Transfer. In *Physical Inorganic Chemistry*, John Wiley & Sons, Inc.: 2010; pp 75-108.

121. Cai, Y.; Ellern, A.; Espenson, J. H., New Oxorhenium(V) Compound for Catalyzed Oxygen Atom Transfer from Picoline *N*-Oxide to Triarylphosphines. *Inorganic Chemistry* **2005,** *44* (7), 2560-2565.

122. Keith, J. M.; Tomić, Z. D.; Zarić, S. D.; Hall, M. B., Oxygen atom transfer catalysis: Ligand effects on the key reaction barrier in molybdenum (VI) dioxo systems. *Journal of Molecular Catalysis A: Chemical* **2010,** *324* (1–2), 15-23.

123. Park, J.; Morimoto, Y.; Lee, Y.-M.; Nam, W.; Fukuzumi, S., Metal Ion Effect on the Switch of Mechanism from Direct Oxygen Transfer to Metal Ion-Coupled Electron Transfer in the Sulfoxidation of Thioanisoles by a Non-Heme Iron(IV)−Oxo Complex. *Journal of the American Chemical Society* **2011,** *133* (14), 5236-5239.

124. Holm, R. H., Metal-centered Oxygen Atom Transfer Reactions. *Chemical Reviews* **1987,** *87* (6), 1401-1449.

125. Grundmann, C.; Grünanger, P. The Nitrile Oxides: Versatile Tools of Theoretical and Preparative Chemistry; Springer-Verlag: Berlin, Germany, **1971**.

126. Haaland, A., Covalent versus Dative Bonds to Main Group Metals, a Useful Distinction. *Angewandte Chemie International Edition in English* **1989,** *28* (8), 992-1007.

127. Shiro, M.; Yamakawa, M.; Kubota, T., The structures of 4-methoxy-2,6-dimethylbenzonitrile N-oxide (I), 4-bromo-2,6-dimethylbenzonitrile N-oxide (II) and 2,4,6-trimethylbenzonitrile N-oxide (III). *Structural Crystallography and Crystal Chemistry* **1979**, 35, 712– 716.

128. Herzberg, G. Electronic Spectra and Electronic Structure of Polyatomic Molecules; Van Nostrand: New York, **1966**; p 1.

129. Luo, Y. R. Handbook of Bond Dissociation Energies in Organic Compounds; CRC Press: Boca Raton, FL, **2003**.

130. The authors are not aware of this thermodynamically favored loss of O_2 occurring in either catalyzed or uncatalyzed reactions.

131. a) Grundmann, C.; Frommeld, H.-D., Nitrile Oxides. III. Reduction of Nitrile Oxides to Nitriles1. *The Journal of Organic Chemistry* **1965,** *30* (6), 2077-2078. b) Sicard, G.; Baceiredo, A.; Crocco, G.; Bertrand, G., A New Route to Nitrile Oxides via α-Nitrosodiazo Derivatives. *Angewandte Chemie International Edition in English* **1988,** *27* (2), 301-302.

132. a) J. A. Johnson, M.; L. Odom, A.; C. Cummins, C., Phosphorus Monoxide as a Terminal Ligand. *Chemical Communications* **1997,** 1523-1524. b) Piro, N. A.; Cummins, C. C., An Unusual P−P Double Bond Formed via Phospha-Wittig Transformation of a Terminal PO Complex. *Journal of the American Chemical Society* **2009,** *131* (25), 8764-8765.

133. Beck, W.; Keubler, M.; Leidl, E.; Nagel, U.; Schaal, M.; Cenini, S.; Del Buttero, P.; Licandro, E.; Maiorana, S.; Villa, A. C., Facile P-C bond Cleavage in the Reactions of Nitrile Oxides with Zerovalent Triphenylphosphine Platinum Complexes. *Journal of the Chemical Society, Chemical Communications* **1981,** 446-448.

134. Genco, N. A.; Partis, R. A.; Alper, H., Iron Pentacarbonyl and the Hydridoundecacarbonyltriferrate Anion as Reagents for Converting Benzohydroxamoyl Chlorides to Nitriles. Deoxygenation of Nitrile Oxides. *The Journal of Organic Chemistry* **1973,** *38* (26), 4365-4367.

135. Feuer, H., Ed.; Nitrile Oxides, Nitrones, and Nitronates in Organic Synthesis; John Wiley & Sons: Hoboken, NJ, **2008**.

136. a) Bokach, N. A.; Khripoun, A. V.; Kukushkin, V. Y.; Haukka, M.; Pombeiro, A. J. L., A Route to 1,2,4-Oxadiazoles and Their Complexes via Platinum-Mediated 1,3-Dipolar Cycloaddition of Nitrile Oxides to Organonitriles. *Inorganic Chemistry* **2003,** *42* (3), 896-903. b) Kuznetsov, M. L.; Kukushkin, V. Y.; Dement'ev, A. I.; Pombeiro, A. J. L., 1,3-Dipolar Cycloaddition of Nitrones to Free and Pt-Bound Nitriles. A Theoretical Study of the Activation Effect, Reactivity, and Mechanism. *The Journal of Physical Chemistry A* **2003,** *107* (31), 6108-6120.

137. a) McDonough, J. E.; Mendiratta, A.; Curley, J. J.; Fortman, G. C.; Fantasia, S.; Cummins, C. C.; Rybak-Akimova, E. V.; Nolan, S. P.; Hoff, C. D., Thermodynamic, Kinetic, and Computational Study of Heavier Chalcogen (S, Se, and Te) Terminal Multiple Bonds to Molybdenum, Carbon, and Phosphorus. *Inorganic Chemistry* **2008,** *47* (6), 2133-2141. b) Huang, J.; Schanz, H.-J.; Stevens, E. D.; Nolan, S. P.; Capps, K. B.; Bauer, A.; Hoff, C. D., Structural and Solution Calorimetric Studies of Sulfur Binding to Nucleophilic Carbenes. *Inorganic Chemistry* **2000,** *39* (5), 1042-1045. c) Capps, K. B.;

Wixmerten, B.; Bauer, A.; Hoff, C. D., Thermochemistry of Sulfur Atom Transfer. Enthalpies of Reaction of Phosphines with Sulfur, Selenium, and Tellurium, and of Desulfurization of Triphenylarsenic Sulfide, Triphenylantimony Sulfide, and Benzyl Trisulfide. *Inorganic Chemistry* **1998,** *37* (12), 2861-2864.

138. a) Delaude, L.; Demonceau, A.; Wouters, J., Assessing the Potential of Zwitterionic NHC·CS$_2$ Adducts for Probing the Stereoelectronic Parameters of N-Heterocyclic Carbenes. *European Journal of Inorganic Chemistry* **2009,** 2009 (13), 1882-1891. b) Duong, H. A.; Tekavec, T. N.; Arif, A. M.; Louie, J., Reversible carboxylation of *N*-heterocyclic carbenes. *Chemical Communications* **2004,** 112-113.

139. work in progress.

140. Lee, S. C.; Holm, R. H., Toward an Expanded Oxygen Atom Transfer Reactivity Scale: Computational Investigation of the Energetics of Oxo Transfer Reaction Couples. *Inorganica Chimica Acta* **2008,** *361* (4), 1166-1176.

141. Cox, J. D.; Wagman, D. D.; Medvedev, V. A. CODATA Key Values for Thermodynamics; Hemisphere: New York, **1989**.

142. Dinescu, A.; Whiteley, C.; Combs, R. R.; Cundari, T. R., Oxygen Atom Transfer Energetics: Assessment of the Effect of Method and Solvent. *The Journal of Physical Chemistry A* **2006,** *110* (11), 4053-4056.

143. Temprado, M.; Cai, X.; Majumdar, S.; Captain, B.; Hoff, C. D.; work in progress.

144. Williams, D. S.; Meyer, T. J.; White, P. S., Preparation of Osmium(II) Nitrosyls by Direct Oxidation of Osmium(VI) Nitrides. *Journal of the American Chemical Society* **1995,** *117* (2), 823-824.

145. Díez-González, S.; Marion, N.; Nolan, S. P., *N*-Heterocyclic Carbenes in Late Transition Metal Catalysis. *Chemical Reviews* **2009,** *109* (8), 3612-3676.

146. Kirklin, D. R.; Domalski, E. S., Enthalpies of Combustion of Triphenylphosphine and Triphenylphosphine Oxide. *The Journal of Chemical Thermodynamics* **1988,** *20* (6), 743-754.

147. Bedford, A. F.; Mortimer, C. T., 327. Heats of Formation and Bond Energies. Part II. Triethyl Phosphate, Triphenylphosphine, and Triphenylphosphine Oxide. *Journal of the Chemical Society (Resumed)* **1960,** 1622-1625.

148. Chernick, C. L.; Skinner, H. A., 285. Thermochemistry of Organophosphorus Compounds. Part II. Triethyl Phosphate, Tripropylphosphine Oxide, and Tributylphosphine Oxide. *Journal of the Chemical Society (Resumed)* **1956,** 1401-1405.

149. The P–O BDEs for Me$_3$PO from ref 120 of 139 kcal mol^{-1} and for Bu$_3$PO from ref 121 of 137.2 kcal mol^{-1} are in agreement with the values of 138.5 and 137.6 kcal mol^{-1} respectively for Me$_3$PO and Cy$_3$PO in this work.

150. Data taken from the NIST Webbook. http://webbook.nist.gov/chemistry

151. Stephens, F. H.; Johnson, M. J. A.; Cummins, C. C.; Kryatova, O. P.; Kryatov, S. V.; Rybak-Akimova, E. V.; McDonough, J. E.; Hoff, C. D., Mechanism of White Phosphorus Activation by Three-Coordinate Molybdenum(III) Complexes: A Thermochemical, Kinetic, and Quantum Chemical Investigation. *Journal of the American Chemical Society* **2005,** *127* (43), 15191-15200.

152. Cherry, J.-P. F.; Johnson, A. R.; Baraldo, L. M.; Tsai, Y.-C.; Cummins, C. C.; Kryatov, S. V.; Rybak-Akimova, E. V.; Capps, K. B.; Hoff, C. D.; Haar, C. M.; Nolan, S. P., On the Origin of Selective Nitrous Oxide N−N Bond Cleavage by Three-Coordinate Molybdenum(III) Complexes. *Journal of the American Chemical Society* **2001,** *123* (30), 7271-7286.

153. Caramori, G.; Frenking, G., Analysis of the metal–ligand bonds in [Mo(X)(NH2)3] (X = P, N, PO, and NO), [Mo(CO)$_5$(NO)]$^+$, and [Mo(CO)$_5$(PO)]$^+$. *Theor Chem Account* **2008,** *120*(4-6), 351-361.

154. a) Frenking, G.; Wichmann, K.; Fröhlich, N.; Grobe, J.; Golla, W.; Van, D. L.; Krebs, B.; Läge, M., Nature of the Metal−Ligand Bond in M(CO)$_5$PX$_3$ Complexes (M = Cr, Mo, W; X = H, Me, F, Cl):   Synthesis, Molecular Structure, and Quantum-Chemical Calculations. *Organometallics* **2002,** *21* (14), 2921-2930. b) Fischer, R. A.; Schulte, M. M.; Weiss, J.; Zsolnai, L.; Jacobi, A.; Huttner, G.; Frenking, G.; Boehme, C.; Vyboishchikov, S. F., Transition Metal Coordinated Al(X)L$_2$ and Ga(X)L$_2$ Fragments. *Journal of the American Chemical Society* **1998,** *120* (6), 1237-1248.

155. Martin, D.; Soleilhavoup, M.; Bertrand, G., Stable Singlet Carbenes as Mimics for Transition Metal Centers. *Chemical Science* **2011,** *2* (3), 389-399.

156. Quadrelli, P.; Mella, M.; Gamba Invernizzi, A.; Caramella, P., The Mild Oxidation of Nitrile Oxides Affords a Convenient Entry to Nitrosocarbonyl Intermediates, Versatile Tools in Organic Syntheses. *Tetrahedron* **1999,** *55* (34), 10497-10510.

157. Pangborn, A. B.; Giardello, M. A.; Grubbs, R. H.; Rosen, R. K.; Timmers, F. J., Safe and Convenient Procedure for Solvent Purification. *Organometallics* **1996,** *15* (5), 1518-1520.

158. a) Barybin, M. V.; Diaconescu, P. L.; Cummins, C. C., Coordination Chemistry of a Chelating Amidoximato Ligand. *Inorganic Chemistry* **2001,** *40* (12), 2892-2897. b) Grundmann, C.; Dean, J. M., Nitrile Oxides. V. Stable Aromatic Nitrile Oxides1,2. *The Journal of Organic Chemistry* **1965,** *30* (8), 2809-2812.

159. Apex2 Version 2.2–0 and SAINT+ Version 7.46A; Bruker Analytical X-ray System, Inc.: Madison, WI, **2007**.

160. a) Sheldrick, G. M. SHELXTL, Version 6.1; Bruker Analytical X-ray Systems, Inc.: Madison, WI, **2000**. b) Sheldrick, G. M. Acta Crystallogr. **2008**, A64, 112– 122.

161. Becke, A. D., Density-functional Thermochemistry. III. The role of exact exchange. *Journal of Chemical Physics* **1993**, 98, 5648.

162. Kameo, H.; Ishii, S.; Nakazawa, H., Synthesis of Iridium Complexes Bearing {o-($Ph_2P)C_6H_4$}$_3$E Type (E = Si, Ge, and Sn) Ligand and Evaluation of Electron Donating Ability of Group 14 Elements E. *Dalton Transactions* **2012,** *41* (27), 8290-8296.

163. Zhao, Y.; Schultz, N. E.; Truhlar, D. G., Design of Density Functionals by Combining the Method of Constraint Satisfaction with Parametrization for Thermochemistry, Thermochemical Kinetics, and Noncovalent Interactions. *Journal of Chemical Theory and Computation* **2006,** *2* (2), 364-382.

164. Frisch, M. J.; Gaussian 09, revision B.01; Gaussian, Inc.: Wallingford, CT, **2010**.

165. a) Simon, S.; Duran, M.; Dannenberg, J. J., How does Basis Set Superposition Error Change the Potential Surfaces for Hydrogen-bonded Dimers? *Journal of Chemical Physics* **1996**, 105, 11024. b) Boys, S. F.; Bernardi, F., The Calculation of Small Molecular Interactions by the Differences of Separate Total Energies. Some Procedures with Reduced Errors. *Molecular Physics* **1970**, 19, 553.

166. Andrae, D.; Häußermann, U.; Dolg, M.; Stoll, H.; Preuß, H., Energy-adjustedab Initio Pseudopotentials for the Second and Third Row Transition Elements. *Theoretica chimica acta* 1990, *77* (2), 123-141.

167. Fukui, K., The Path of Chemical Reactions - the IRC Approach. *Accounts of Chemical Research* **1981,** *14* (12), 363-368.

168. Curtiss, L. A.; Raghavachari, K.; Redfern, P. C.; Rassolov, V.; Pople, J. A., Gaussian-3 (G3) Theory for Molecules Containing First and Second-row Atoms. *Journal of Chemical Physics* **1998**, 109, 7764.

169. a) Chapter 2 is adapted with permission from (Cai, X.; Majumdar, S.; Fortman, G. C.; Cazin, C. S. J.; Slawin, A. M. Z.; Lhermitte, C.; Prabhakar, R.; Germain, M. E.; Palluccio, T.; Nolan, S. P.; Rybak-Akimova, E. V.; Temprado, M.; Captain, B.; Hoff, C. D., Oxygen Binding to [Pd(L)(L′)] (L= NHC, L′ = NHC or PR_3, NHC = *N*-Heterocyclic Carbene). Synthesis and Structure of a Paramagnetic *trans*-[Pd(NHC)$_2$(η^1-O_2)$_2$] Complex. *Journal of the American Chemical Society* 2011, *133* (5), 1290-1293.). Copyright (2010) American Chemical Society. b) Chapter 4 is adapted with permission from (Cozzolino, A. F.; Tofan, D.; Cummins, C. C.; Temprado, M.; Palluccio, T. D.; Rybak-Akimova, E. V.; Majumdar, S.; Cai, X.; Captain, B.; Hoff, C. D., Two-Step Binding of O_2 to a